Manipulation in microfluidic systems using surface acoustic waves (SAW)

by

David J. Collins, BE(Hons)

Submitted by David J. Collins

for fulfillment of the Requirements for the Degree of

Doctor of Philosophy

Supervisor: A/Prof. Adrian Neild

Associate Supervisor: Dr. Tuncay Alan

Department of Mechanical and Aerospace Engineering

Monash University

May, 2014

Copyright Notices

Notice 1

Notice 2

Do something you enjoy

Contents

List of Tables . . . . . **vii**

List of Figures . . . . . **ix**

Abstract . . . . . **xiii**

Acknowledgments . . . . . **xvii**

1 Introduction **1**
1.1 Microfluidics 1
1.2 Thesis outline 3
1.2.1 Chapter 2 4
1.2.2 Chapter 3 4
1.2.3 Chapter 4 4
1.2.4 Chapter 5 5
1.2.5 Chapter 6 5
1.2.6 Chapter 7 5
1.2.7 Chapter 8 6

2 Background **7**
2.1 The lab-on-a-chip paradigm 7
2.2 Microfluidic concepts 9
2.2.1 Droplet based microfluidics 11
2.2.2 Actuation methods 14
2.3 Surface acoustic waves (SAW) 17
2.3.1 Principles 18
2.3.2 Acoustic pressure 21
2.3.3 Acoustic streaming 24
2.4 Relevant applications of SAW 28
2.4.1 Atomization 28
2.4.2 Concentration 31
2.4.3 Sorting 33

3 Microfabrication **37**
3.1 Overview 37
3.2 SAW device fabrication 38
3.3 Chamber fabrication 39
3.4 Device assembly 41
3.5 Experimental setup 42

4 SAW atomization droplet size . . . 47
4.1 Introduction . . . 47
4.2 Publication . . . 48

5 On demand droplet production and encapsulation . . . 61
5.1 Introduction . . . 61
5.2 Publication . . . 62

6 Particle trapping, concentration and release . . . 75
6.1 Introduction . . . 75
6.2 Publication . . . 76

7 Virtual deterministic lateral displacement . . . 83
7.1 Introduction . . . 83
7.2 Publication . . . 84

8 Conclusions . . . 97
8.1 Contributions . . . 97
8.2 Continuing and future work . . . 99

Appendix A Conference paper . . . 103

Appendix B Flow around a PDMS membrane . . . 107

List of Tables

2.1 Microfluidic actuation methods 15

3.1 Microfabrication processes 40

List of Figures

1.1 The number of publications on acoustic microfluidics is less than that for other microfluidic actuation methods. The number of publications was estimated by the number of search results in Google Scholar (www.scholar.google.com), using the search term 'optical microfluidics', 'magnetic microfluidics', etc. Here, surface acoustic wave (SAW) publications are a subset of acoustic microfluidic ones. . . 3

2.1 An example of the LOC concept, here showing a device capable of performing multiple steps required in genetic analysis. Here, several different components, including heaters, sensors, electrophoretic arrays and addressable valves can be integrated into a single, compact system to reduce the cost and time of genetic analysis. Reproduced with permission from [38]. Copyright 2005, Royal Society of Chemistry. 8

2.2 Microfluidic techniques, such as the passive one shown here, are required in order to analyze micron-scale species such as cells. Here, cells are trapped in an array of polydimethylsiloxane (PDMS) mcirco-structured features, designed so that each trap contains a maximum of one cell. Reproduced with permission from [39]. Copyright 2006, ACS publications. 9

2.3 (A,B) Passive micromixers use fluid-folding techniques to reduce the thickness of adjoining reagent layers so that diffusion acts over smaller distances. (C) Active mechanical methods perform mixing by raising local Reynolds numbers over small lengths. (A) Reproduced with permission from [40, 41]. Copyright 2001, 2011, Royal Society of Chemistry. (B) Reproduced with permission from [42]. Copyright 2006, National Academy of Sciences. (C) Reproduced with permission from [43]. Copyright 2004 Royal Society of Chemistry. 10

2.4 The relative dominance of interfacial forces such as surface tension allow for fluid handling and manipulation methods that are not feasible on a macro-scale. (A) Individual droplets, whose shape is maintained by surface tension, can be manipulated in an electrowetting array, including transport and mixing. (B) Similarly, interfacial forces allow the self-filling/pumping properties of micro-structured channels, with capillary wicking driving fluid flow. (A) Reproduced with permission from [56]. Copyright 2008, Royal Society of Chemistry. (B) Reproduced with permission from [57]. Copyright 2008, John Wiley and Sons 12

2.5 A microfluidic water-in-oil droplet is produced primarily using a microfabricated (a) T-junction or (b) flow-focussing geometry. (c) Individual droplets for discrete number of cells is an ideal system for a miniature bioreactor, simplifying analysis and cell handling. (d) The droplet breakup mechanism, which in part determines final droplet dimensions, can be described as the (1) squeezing, (2) dripping or (3) jetting regime, a function of the value of Ca_c. (e) Discretized fluid units form the basis for digital microfluidics, with hydrodynamic logic possible, here demonstrating (A) three AND gates in a ring oscillator and (C) a fluidic ladder for droplet timing synchronization. (a-c) Reproduced with permission from [59]. Copyright 2010, IOP Publishing. (d) Reproduced with permission from [62]. Copyright 2007, Cambridge University Press. (e) Reproduced with permission from [65]. Copyright 2007, The American Association for the Advancement of Science. . . 13

2.6 A variety of actuation methods and forces are used in lab-on-a-chip systems for manipulating microfluidic species. Different actuation methods can be used to perform a range of activities, including (a) magnetically controlled mixing, (b) optical separation, (c) acoustic sorting, (d) electrical cell membrane fusion and hydrodynamic sorting using either (e) deterministic rolling or (f) inertial separation. (a) Reproduced from [120]. Copyright 2007, IEEE. (b) Reproduced with permission from [87]. Copyright 2003, Nature Publishing Group. (c) Reproduced with permission from [121]. Copyright 2014, Elsevier. (d) Reproduced with permission from [48]. Copyright 2012, The Royal Society of Chemistry. (e) Reproduced with permission from [86], Copyright 2012, The Royal Society of Chemistry. (f) Reproduced with permission from [122], Copyright 2009, The Royal Society of Chemistry. 16

2.7 Acoustic fields generated by SAW have found use for a diverse range of microfluidic applications, including (A) concentration, (B) pumping, (C) sessile droplet transport, and (D) oil-water droplet sorting. (A) Reproduced with permission from [111], Copyright 2008, The Royal Society of Chemistry. (B) Reproduced with permission from [141]. Copyright 2008, AIP Publishing LLC. (C) Reproduced with permission from [142]. Copyright 2006, SAGE Publications. (D) Reproduced with permission from [78], Copyright 2009, The Royal Society of Chemistry. . . 18

2.8 A SAW device is comprised of a piezoelectric substrate on which a series of interdigital transducers (IDTs) are arrayed. When excited at its resonant frequency, these IDTs produce a wave that will travel directionally along the substrate surface. 18

2.9 An advantage of SAW is that there are several different IDT configurations and patterns that can be used to achieve the desired frequency or field shape characteristics. (a) Normal IDTs, (b) split-finger IDTs and (c) single-phase unidirectional IDTS are some of the more common IDT configurations, which can be further modified into (d) slanted finger, (e) chirped and (f) focussed IDTs patterns. 20

2.10 SAW microfluidic systems make use of both (a) traveling and (b) standing wave setups, the latter showing a part of the region where a standing SAW exists. Either traveling or standing waves can then be applied to either (c) open, or droplet-based systems, or (d) closed channel-based systems whose boundaries are defined by channels bonded onto the substrate, both of which are shown here in a standing wave setup. The use of either traveling waves or standing waves in an open or closed microfluidic system depends on the intended application. 21

2.11 Configurations of for the production of (a) Langevin and (b) Rayleigh radiation pressures. In both cases a transducer (T) produces waves (W) which are incident on the absorber (A). 22

2.12 A SAW incident on a fluid body will undergo amplitude attenuation, transferring acoustic energy to the fluid with the resulting wavefronts propagating at the Rayleigh angle θ_R. Attenuation of the acoustic beam in the fluid itself gives rise to a momentum flux, with this momentum transfer resulting in a bulk fluid motion known as acoustic streaming. Reproduced with permission from [25]. Copyright 2009, AIP Publishing LLC. 25

2.13 Atomization is the process through which capillary instabilities resulting from acoustic actuation result in droplet break-off from a larger liquid bulk. Shown here for a (a) a fluid atop a (b) bulk-mode vibrating transducer and a (b-f) SAW device. (b,c) In a SAW atomization system (e,f) droplets of different characteristic dimensions are produced. (a) Reproduced with permission from [177]. Copyright 2002, Springer. (b-f) Reproduced with permission from [35]. Copyright 2009, The Royal Society of Chemistry. 28

2.14 Images of droplet breakup. (a) Subthreshold capillary wave amplitude results in a vibrating surface, with no or few droplets produced. (b) Atomization occurs when the capillary stabilization forces are overcome in the presence of sufficient external forcing in the process of liquid thread formation and subsequent droplet pinch-off. Image reproduced with permission from [178]. Copyright 2007, AIP Publishing LLC. 29

2.15 SAW particle concentration can be accomplished via several independent mechanisms. (A) Viscosity-induced shear stress results in particle migration to the center of a droplet actuated by asymmetrical acoustic streaming. (B) A standing wave acoustic force created by a set of opposing IDTs results in patterning of particles at the acoustic nodes in both a (a,c) 1D and (b,d) 2D field. (C) In a novel method, a small (mm-scale) disc is placed on a SAW device via a viscous coupling layer, and is induced to spin by asymmetric application of SAW. Concentration in this case is mediated by centrifugal forces. (A) Reproduced with permission from [94]. Copyright 2008, AIP Publishing LLC. (B) Reproduced with permission from [101]. Copyright 2009, The Royal Society of Chemistry. (C) Reproduced with permission from [194]. Copyright 2012, Wiley Online Library. 32

2.16 Particle separation and sorting using SAW is based on the differential force that is applied to different microfluidic species as determined by their different size or acoustic contrast. Separation of different particle sizes, for example, has been demonstrated using (A) standing wave SAW, with the acoustic force $F \sim R^3$ or (B) traveling waves, with $F \sim R^6$. (C) These forces can also be used for more generalized sorting, with particles, cells or fluid streams directed towards a desired outlet when a SAW is applied. (A) Reproduced with permission from [202]. Copyright 2009, The Royal Society of Chemistry. (B) Reproduced with permission from [203]. Copyright 2013, The Royal Society of Chemistry. (C) Reproduced with permission from [79]. Copyright 2010, The Royal Society of Chemistry. 34

3.1 A properly implemented and practical SAW device is composed not only of the IDTs that are used to generate a SAW, but also the electrode pads that are used to apply the AC signal, markers for the purpose of aligning PDMS chambers and channels on the device and readable text that describes the device type and/or SAW wavelength (labeled in inset). An example device, comprised of six separate devices, is shown here. 38

3.2 Fabrication procedures in the lift-off process to produce patterned metals on a piezoelectric substrate: the SAW device. (1-2) A $LiNbO_3$ wafer spin-coated in photoresist is (3) selectively exposed to UV light @ 387 nm, which after (4) development results in patterned features. Subsequent (5) metal deposition and (6) lift-off results in patterned metals on $LiNbO_3$. Dicing the wafer results in finished devices ready for bonding. 41
3.3 Fabrication options to produce a PDMS chamber. (1-2) A silicon wafer spin-coated in photoresist is (3) selectively exposed to UV light @ 387 nm, which after (4a,4b) development results in patterned features. These features, if at the right height, can (5b) be directly used to produce a finished PDMS chamber. Alternatively, the photoresist (or a metal on silicon patterned by lift-off) can (5a) be used as a mask for deep reactive ion etching (DRIE), resulting in a silicon mould for PDMS. 42
3.4 A PDMS chamber and SAW device can be bonded together to create fully enclosed fluid chambers in which SAW can be used to manipulate particles and cells. Here, (1) patterned PDMS and a SAW device are (2) exposed to an oxygen plasma. These surface-activated components are then (3) aligned and brought into contact with one another, resulting in (4) a finished device. 43
3.5 A thermally conducting heat pump such as a thermoelectric cooler can be used to choose the steady state device temperature and limit long-term temperature changes. Here, the device is measured at the site of the microfluidic channel subject to SAW (black box in inset) mounted on either a either a thermally non-conductive glass slide or a peltier cooler [PC] (at 0 V, 1 V or 2 V). SAW power is 0.4 W. 44
3.6 (a) The device platform (shown here with representative SAW device) integrates a thermoelectric heat pump that moves heat generated by the SAW device to (b) a combined heat-sink/fan on the underside of the platform. (c) This platform allows for flexible removal of different-sized probe mounts. (d) The thermoelectric device itself is a 40 mm square unit bonded with thermally conductive paste to the heat sink. By applying different electric polarizations the active side can be heated as well as cooled, if this is required. 45

8.1 With multiple independent vDLD channels it is possible to sort multiple particle or cell populations simultaneously by making use of arbitrarily small differences in parameters, including size, electrical permittivity and stiffness. 99
8.2 Using a 2D acoustic field it is is possible to create an array of particles, with only one particle per acoustic node (a,b). Using a partial traveling wave in one direction, excess particles are swept in the direction of the traveling wave. Bulk manipulation of particles is made possible through periodic frequency sweeps, with (c) decreasing and (d) increasing frequencies leading to dispersal and concentration, respectively. 100

B.1 Particles subject to an acoustic field oriented principally vertically in the system demonstrated in Chapter 6 will are trapped behind a 3D structured PDMS feature. Here, particles collection is aided by the lower characteristic fluid velocity in the region immediately behind this membrane. Discontinuities at the entrance to the channel are a result of the constant 0.5 mm/s flow condition, which quickly relaxes into a normal parabolic flow profile. 108

Manipulation in microfluidic systems using surface acoustic waves (SAW)

David J. Collins, BE(Hons)
[redacted]
Monash University, 2014

Supervisor: A/Prof. Adrian Neild
[redacted]
Associate Supervisor: Dr. Tuncay Alan
[redacted]

Abstract

Lab-on-a-chip microfluidic systems hold substantial promise for a wide range of diagnostic and therapeutic applications. By shrinking down conventional laboratory processes and replicating their functions on-chip, the size, cost, required time, and amount of reagent and sample needed can be drastically reduced. However, because these devices operate at length scales orders of magnitude smaller than conventional fluid processes different physical phenomena become dominant, meaning new forces and techniques must be developed to perform them. Acoustic forces have the potential to be useful at small length scales, though, their use has for the most part been limited by the relatively small force magnitudes and low frequencies at which they have been generated, thereby limiting the promise of rapid acoustic manipulation on microfluidic scales. However, a developing technology relying on the application of surface acoustic waves (SAW) has shown the potential to overcome these limitations, especially due to the high frequencies (10–2000 MHz) and correspondingly small length scales (2–300 μm), on the order of the bacteria and eukaryotic cells, that are characteristic of this method. In this thesis, SAW is used in a range of applications that emphasize these advantages, specifically with respect to the large and localized forces that can be generated on interfaces, both between two immiscible phases and on particles within a single fluid phase. In the studies presented here, SAW is used to (1) actuate a fluid-air interface for the production of water-in-air droplets with tunable diameters in the range of $\sim$0.5–50 μm for the purpose of targeted nebulization therapy, (2) actuate a water-oil interface for the tunable production of picoliter-sized water-in-oil droplets with simultaneous particle pre-concentration and encapsulation for application in digital microfluidic systems, (3) perform controlled concentration and release of particles using a novel microfabricated channel structure and (4) deterministically

sort particles over a large size range, demonstrated between 0.3–7 μm with potential application in cell sorting systems where high sorting efficiency or sorting based on only small size differences is required. Finally the case is made that acoustic fields, especially those produced by SAW, are optimal for many, if not most, applications where manipulation of microfluidic species is required.

Manipulation in microfluidic systems using surface acoustic waves (SAW)

In accordance with Monash University Doctorate Regulation 17.2 Doctor of Philosophy and Research Master's regulations the following declarations are made:

I hereby declare that this thesis contains no material which has been accepted for the award of any other degree or diploma at any university or equivalent institution and that, to the best of my knowledge and belief, this thesis contains no material previously published or written by another person, except where due reference is made in the text of the thesis.

This thesis includes three original papers published in peer reviewed journals and publication in review. The core theme of the thesis is the application of surface acoustic waves (SAW) in microfluidic systems, with specific attention to the force exerted on interfaces. The ideas, development and writing up of all the papers in the thesis were the principal responsibility of myself, the candidate, working within the department of mechanical engineering under the supervision of Assoc. Prof. Adrian Neild and Dr. Tuncay Alan.

The inclusion of co-authors reflects the fact that the work came from active collaboration between researchers and acknowledges input into team-based research.

In the case of the publications reproduced in this this (listed on the next page), my contributions to this work was as the chief investigator, responsible for fabrication, experimental design and experimentation, analytical and numerical simulations, interpretation of results and writing of the publications, in part or in full. Specific detail of these contributions are given in the declarations for each chapter containing a publication.

David J. Collins
October 30, 2014

Full list of publications

Publications

Thesis Chapter	Publication
4	D.J. Collins, O. Manor, A.Winkler, H. Schmidt, J.R. Friend, and L.Y. Yeo. Atomization off thin water films generated by high-frequency substrate wave vibrations. *Physical Review E*, 86(5):056312, 2012.
5	David J Collins, Tuncay Alan, Kristian Helmerson, and Adrian Neild. Surface acoustic waves for on-demand production of picoliter droplets and particle encapsulation. *Lab on a Chip*, 13(16):32253231, 2013.
6	David J Collins, Tuncay Alan, and Adrian Neild. The particle valve: on-demand particle trapping, filtering and release from a microfabricated PDMS membrane using surface acoustic waves (SAW). *in review*, 2014.
7	David J Collins, Tuncay Alan, and Adrian Neild. Particle separation using virtual deterministic lateral displacement (vDLD). *Lab on a Chip*, 14(9):15951603, 2014.

Conference proceedings

Appendix	proceeding
A	David J Collins, Tuncay Alan, Kristian Helmerson, and Adrian Neild. On-demand picoliter-scale droplet generation using surface acoustic waves. *17th International Conference on Miniaturized systems for Chemistry and life Sciences October, 2013.*

Acknowledgments

There are many people who deserve credit and thanks for supporting me through my candidature. First and foremost I would like to thank my supervisors, A/Prof. Adrian Neild and Dr. Tuncay Alan for working with me over the last few years. The genuine care you have for the well being and success of all of the students under your care is obvious. This thesis would not have been possible without your guidance, and I am very thankful for the time you've given me to listen to my crazy ideas. I think our work together has been very fruitful, and I hope we get the chance to work together in the future.

My previous supervisors, Prof. Leslie Yeo, Prof. James Friend and Dr. Ofer Manor also deserve thanks for their help in getting me involved in research in the first place. I can only hope that I've inherited even a portion of their professionalism, research skills and work ethic. Our collaborators in and out of the university, Andreas Winkler, Hagen Schmidt and Kristian Helmerson were also instrumental in making our research a success.

I thank my numerous current and former group members including Anushi, Mike, Jeremy, Ricky, Nick, Aisha, Christina, Priscilla, Debadi, Sam, Robin, Jue Nee, Amarin, Saab, Jason, Muhsincan, Bulut, Nin, Emin, Ian, and Ganaka for keeping me sane throughout my PhD and being a massive help in the lab. Device fabrication couldn't have happened without the help of Melbourne Centre for Nanofabrication (MCN) staff past and present, including Sasi, Doug, Zoran, Ricky, Varsha, Sean and Yang. I also appreciate the support and help from the department and its staff.

I also would like to thank all of my family and friends, especially my long suffering house mates Lorne, Amit and Cameron. I consider myself very lucky to know and be able to spend time with you, and I thank you for all of your support throughout my PhD. Lastly, my amazing girlfriend Pamela deserves more gratitude than I can give her. Thank you for keeping me sane through the tough times, and helping me enjoy the good ones. I don't know where I'd be without your love and support.

David J. Collins

Monash University
May 2014

Chapter 1

Introduction

Microfluidics is the scientific field devoted to the study and application of physics at the micro-scale. In this chapter both microfluidic concepts and surface acoustic waves (SAW), a relatively new method for the microfluidic manipulation of cells and particles, are briefly introduced. This is followed by an outline, where the layout for the remainder of this thesis is presented.

1.1 Microfluidics

Broadly considered, microfluidics is the study of fluid physics on the scale of micrometers to millimeters or in fluid volumes of femtoliters to microliters [1, 2]. One reason for working with fluids at this scale is to take advantage of the scaling laws that open up new opportunities for fluid handling. Fluid mixing, for example, can be more easily controlled due to the inherently laminar flow qualities at small length scales and fluid velocities. Commercial and practical advantages also stem from the small size of microfluidic systems, which therefore require less material, smaller amounts of reagent and shorter times required to use these devices than for conventional laboratory processes. Since the field's inception approximately two and half decades ago [3], a wide variety of microfluidic techniques and processes have been developed that expand the range of applications that are possible on these platforms; microfluidic pumps, valves and sensors have all been developed for uses as diverse as flow cytometry, fuel cells and DNA sequencing and analysis, supporting a growing industry of hundreds comprising companies [4]. Though there are a wide variety of applications that employ microfluidic principles, including chemical threat detection [5], inkjet printing technology [6, 7] and display technology [8], it is possible that microfluidics has the potential to make the largest impact in clinical diagnostics and treatment, reducing the

time and expense required for an increasing array of clinical tests in an otherwise burgeoning healthcare system. The range of fluid logic and sensing functions that have been developed on the micro scale has made possible what has been termed the lab-on-a-chip (LOC), a concept that, incorporating the ability to integrate a wide variety of processes and functions on a small scale, has the goal of producing small, portable and complete systems for biomedical diagnosis, detection and therapy. The potential advantages this platform affords are profound; by shifting these functions from a purely clinical setting to the point of care while drastically reducing their cost, detection and treatment of illnesses can happen over smaller time scales, especially in resource and infrastructure poor locations [9]. The manipulation of microfluidic species, including cells, particles, and biomolecules is an integral function in microfluidic systems [10]. Filtering, sorting and concentration of these species are necessary steps for sample pre-treatment and detection. However, many of the methods used to perform these processes in the laboratory setting do not necessarily transfer to the micro-scale; conventional centrifugation, for example (with the force produced $F \sim r\omega^2$, where r is the rotational radius and ω is the angular velocity) becomes less useful as its size and rotational speed become smaller. In order to perform these processes on the micro-scale, methods for on-chip manipulation have been developed that exploit physics at the micro scale, making using of electrical [11], optical [12], magnetic [13], hydrodynamic [14] and acoustic forces [15, 16]. In fact, in many cases functions are made possible by use of these forces that would not be possible on the macro-scale, especially where individual manipulation of biomolecules or cells is desired [17, 18, 19].

Perhaps the least explored method for microfluidic manipulation and actuation are acoustic forces; the number of extant publications on acoustic microfluidics is less than that for any other applicable method (see Fig. 1.1), a loss to the wider field due to the variety of abilities and force scalings that are made possible using acoustic fields, where practical forces on all but the smallest biomolecules can be realized an with bulk fluid motion also made possible through acoustic streaming [10]. This relative dearth of publications may be in part due to the short period in which research in acoustic methods has been ongoing, with some of the first research in the field published only at the turn of the century [20, 21]. Perhaps more limiting for the initial growth of the field, however, was the lack of suitable acoustic actuation technologies that could easily be integrated with microfluidic systems. Many initial methodologies relied on essentially affixing a bulk piezoelectric to a separate microfluidic device [22, 23], making it often difficult, if not impossible,

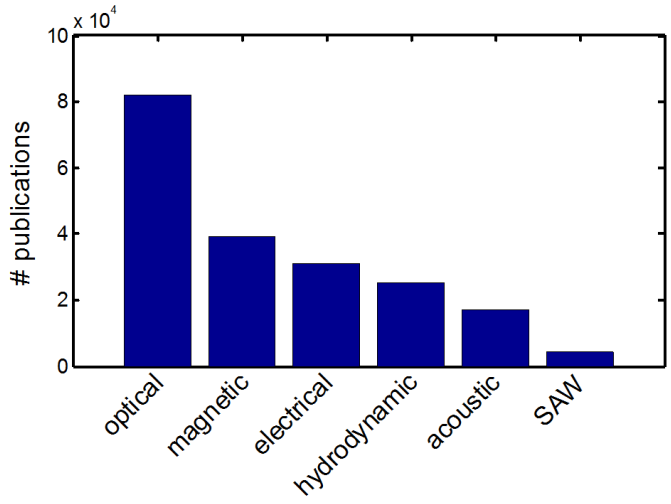

Figure 1.1: The number of publications on acoustic microfluidics is less than that for other microfluidic actuation methods. The number of publications was estimated by the number of search results in Google Scholar (www.scholar.google.com), using the search term 'optical microfluidics', 'magnetic microfluidics', etc. Here, surface acoustic wave (SAW) publications are a subset of acoustic microfluidic ones.

to localize acoustic fields in the section of a microfluidic chip where they are desired, limiting these methods mostly to instances where integration with other components is not required. However, with the introduction of surface acoustic waves (SAW) as a method for microfluidic manipulation on-chip less than a decade ago [24], it is now possible to selectively pattern and localize acoustic forces, and due to it's simple planar construction is broadly compatible with microfluidic devices in general [25]. In the next chapter the background and applications of SAW in the context of microfluidic systems are discussed.

1.2 Thesis outline

The purpose of the research in this thesis is to develop manipulation methods in microfluidic systems using SAW and to develop understanding of the physical principles that underlie these methods. The thesis is laid out as follows: a thorough literature review of SAW in microfluidic systems in Chapter 2, an overview of the fabrication methods used in Chapter 3, whereafter the research is then presented in four separate publications, comprising Chapters 4-7. Finally concluding remarks are made in Chapter 8. These Chapters are described in more detail in the following subheadings.

1.2.1 Chapter 2

In Chapter 2 a thorough literature review is performed, where the basic principles and scaling laws that are inherent to microfluidic systems are discussed in the context of a lab-on-a-chip, a developing concept wherein a small disposable and cost-efficient chip is used to perform any number of diagnostic, analysis or therapeutic functions. This is followed by a discussion of the different technologies used to manipulate fluids and cells and particles within them. SAW is then presented as a developing technology that is capable of improving the performance of on-chip manipulation. The principles that make acoustic actuation possible – acoustic streaming and acoustic pressure – are also discussed. Further, an introduction to atomization, concentration and sorting using SAW, the subjects of research in later chapters, is made.

1.2.2 Chapter 3

Microfabrication procedures are integral to the production of both microfluidic channels and the SAW devices that are used to manipulate particles and cells within these channels. In this chapter the steps required are described for the reliable production of micro-scale features on both lithium niobate, the piezoelectric material on which as SAW is produced and propagates, and in PDMS, the material used to construct the enclosed channels, chambers and other features through which fluid flows.

1.2.3 Chapter 4

In Chapter 4 a systematic exploration of the physics the determine droplet size during SAW atomization is performed. SAW atomization is a developing technique for the production of atomized droplets for the purpose of pulmonary therapy, where different droplet sizes can be used to target different lung regions. Previously there was little understanding of either the droplet size distributions that are produced during high frequency excitation or the principles and scaling laws that determine what these droplet sizes are. Here, we formulate a theory of the distribution of droplet diameters and test it successfully against experimental results.

1.2.4 Chapter 5

Chapter 5 builds off the principles from Chapter 4, here producing droplets in a water-oil system as opposed to water-air. A water-in-oil droplet is a powerful microfluidic tool that allows for the compartmentalization of reactions; in doing so microfluidics becomes digital, potentially performing many different reactions simultaneously, though this would require methods for production and handling of individual droplets. Here we use SAW for the on-demand production of microfluidic droplets, and further demonstrate the capability to simultaneously pre-concentrate and encapsulate particles, here serving as an analogue for cells, within these droplets.

1.2.5 Chapter 6

As the sophistication of lab-on-a-chip systems increases gating functions such as controlled concentration and release becomes increasingly important. In Chapter 6 we expand on the ability to pre-concentrate and release particles on-demand, doing so here in a continuous flow, single phase system. This is done at extremely low powers – on the order of milliwatts – and is made possible by the use of an easily fabricated, quasi-3D membrane structure against which particles are pushed and trapped. Because the force used to trap these particles scales with their dimensions, this system is also demonstrated as a particle sorter, with larger particles trapped and smaller ones continuing in the direction of the flow.

1.2.6 Chapter 7

Chapter 7 presents a method for the sorting of particles with arbitrarily small differences in properties, including size. Particle and cell sorting is a required function in a wide range of pre-treatment and on-chip analysis applications. The sensitivity and practicality of existing methods, however, falls short of requirements for many purposes. Here we demonstrate particle sorting with diameter differences of only 6%, which is a far smaller size difference than that realized previously using SAW. The acoustic field is modeled and the experimental results confirmed against this model. Additionally, it is shown to be possible to perform sorting using electrical forces on particles as well by altering some device parameters, with an electric field in the vicinity of the transducers also being produced.

1.2.7 Chapter 8

In the final chapter a summary of the contributions to the field of SAW microfluidics by the research presented in this thesis is made. Finally, conclusions with regard to the future of the this field and microfluidics and possible future work will be made.

Chapter 2

Background

In this chapter the background and concepts relevant to surface acoustic wave (SAW) actuated microfluidic systems are explored. Here, we find that though the concept of a lab-on-a-chip (LOC) is potentially profoundly useful, there still remain issues regarding its abilities to replicate lab processes with similar fidelity and efficiency. To date, these issues have prevented its widespread implementation and use, especially in portable applications. Here the microfluidic concepts that underpin the LOC concept are explored and SAW is discussed in its potential to address some of these issues.

2.1 The lab-on-a-chip paradigm

The concept of a lab-on-a-chip (LOC) is a powerful one. The essential goal for a LOC device is to replicate, in full, the abilities and power of a complete diagnostic laboratory with integrated components far smaller than their full-scale counterparts. Many advantages are conferred by reducing the scale of a diagnostic system. By shrinking the components, the value of many important parameters are similarly reduced, meaning less time to perform chemical reactions, less time on the part of an operator, less reagents, fewer materials and components, and as a result of this, reduced cost. Properly implemented, this concept has the potential to change clinical diagnostics; by making a simple device that can perform rapid screening or diagnosis cheaply, frequency of doctor visits, and especially cost and delays between testing and diagnostics as with a conventional lab, could be significantly reduced. These advantages have been recognized especially for their application in resource-poor developing countries, where the funds and training needed for diagnostic

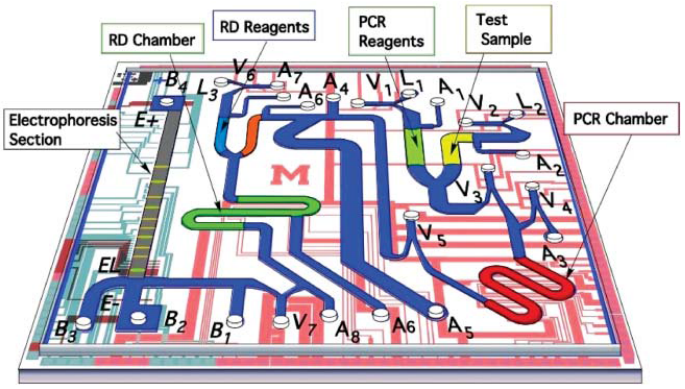

Figure 2.1: An example of the LOC concept, here showing a device capable of performing multiple steps required in genetic analysis. Here, several different components, including heaters, sensors, electrophoretic arrays and addressable valves can be integrated into a single, compact system to reduce the cost and time of genetic analysis. Reproduced with permission from [38]. Copyright 2005, Royal Society of Chemistry.

.

laboratories may be non-existent [26]. While LOC development has focussed mostly on diagnostic applications, it is important to note that the concept can also be extended to other applications as well, such as high throughput screening for drug discovery [27, 28, 29, 30], environmental monitoring [31, 32, 33], and therapeutic roles [34, 35, 36, 37], where the advantages of low-cost, speed or portability are also desired. A picture of a representative LOC integrating many different functions is shown in Fig. 2.1.

Despite the advantages conferred by the LOC, these devices have for the most part yet to achieve widespread use or impact. The reason for this may lie in the relatively short time since LOC concept development in the 1990s, with many applications of LOC systems still in the research stage. However, there are also still challenges that have only partially been addressed to date, especially with regard to the portability, flexibility and production of these platforms. While the chip itself may be quite small, external pumps and analysis equipment are often still required, with typical LOCs only able to perform specific, limited processes that may be restricted to specific reactions or particular input species, requiring bespoke devices for specific applications. For the LOC to become a truly successful platform, these issues related to portability and integration of components should be addressed, though there is fundamentally no barrier to this occurring, requiring further development in the methods used to perform on-chip manipulation to more fully replicate the abilities and flexibility afforded by conventional lab processes. In this chapter, the microfluidic concepts that underpin the LOC paradigm are discussed, with attention later given to

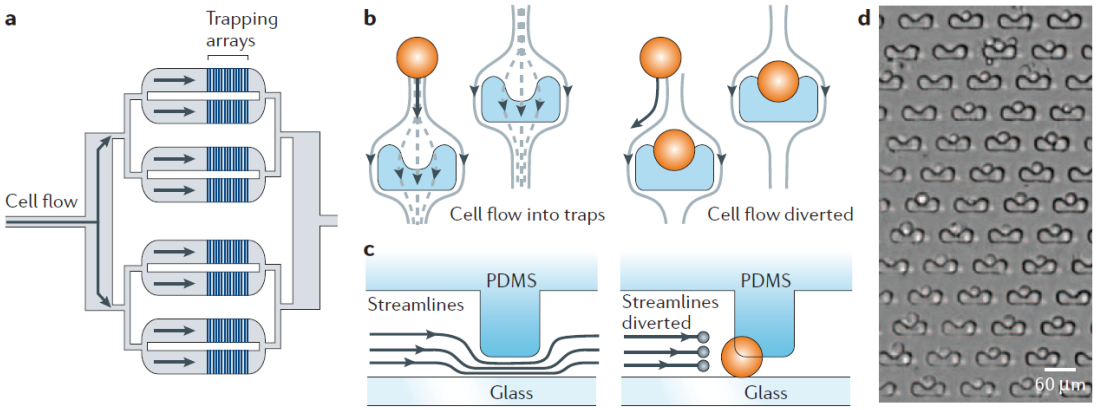

Figure 2.2: Microfluidic techniques, such as the passive one shown here, are required in order to analyze micron-scale species such as cells. Here, cells are trapped in an array of polydimethylsiloxane (PDMS) mcirco-structured features, designed so that each trap contains a maximum of one cell. Reproduced with permission from [39]. Copyright 2006, ACS publications.

.

an on-chip actuation method that has the potential to address many issues preventing widespread implementation of the LOC.

2.2 Microfluidic concepts

Because of its dimensions, LOC platforms rely primarily on techniques and concepts developed in the field of microfluidics, a broad topic of study whose central tenant is the manipulation or processing of small amounts of fluid, with characteristic dimensions on the order of millimeters to nanometers and volumes on the order of microliters to femtoliters [44]. Because of the advantages conferred by using small fluid volumes and from operating on length scales on the order of cells and large biomolecules, this is an increasingly active field [45, 46]. Because of this reduced scale, far from merely replicating abilities on a macroscopic scale, it is possible to utilize effects and forces that may be impractical to use otherwise [47]. Near-field targeted electrical [48] and optical [49, 17] methods, for example, have the ability to manipulate and analyze individual cells and biomolecules on-demand, as shown in Fig. 2.2, in contrast to more indiscriminate conventional bulk cell-culturing and processing. The different physics between the micro and macro scales must be taken into account when designing a microfluidic system. A significant portion of early effort in the microfluidic field has been to replicate conventional laboratory processes, such as centrifugation [50] or DNA sequencing [51], though often methods applicable on the macro-scale are not as effective or are overly complex to implement when scaled down; a replication of results

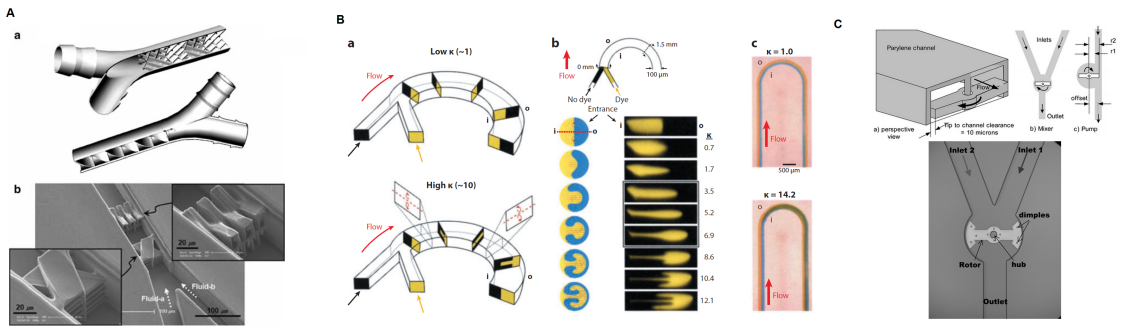

Figure 2.3: (A,B) Passive micromixers use fluid-folding techniques to reduce the thickness of adjoining reagent layers so that diffusion acts over smaller distances. (C) Active mechanical methods perform mixing by raising local Reynolds numbers over small lengths. (A) Reproduced with permission from [40, 41]. Copyright 2001, 2011, Royal Society of Chemistry. (B) Reproduced with permission from [42]. Copyright 2006, National Academy of Sciences. (C) Reproduced with permission from [43]. Copyright 2004 Royal Society of Chemistry.

but not necessarily methods is thus desired. In the case of centrifugation for the purpose of cell sorting, for example, with the force generated proportional to the square of the velocity, $F \sim v^2$, it becomes difficult to generate the required fluid speed in a small space, which would necessitate unrealistic velocity gradients and require time spans that are incompatible with rapid diagnostic devices. To circumvent this, a variety of passive and active techniques (to be discussed in later sections) have been developed that make use of other forces [52]. The need to develop new methods is driven by the different length scales L of microfluidic devices, where different forces are dominant for different L. Dimensionless numbers that determine the dominance of different forces that are influenced by L, include:

- the Reynolds number $Re = \rho UL/\mu$ relating inertial to viscous forces, where ρ, U and μ are the fluid density, characteristic velocity and viscosity,
- the Weber number $We = \rho U^2 L/\gamma$ relating inertial in interfacial forces, where γ is the fluid surface tension,
- the Péclet number UL/D relating the impact of convection and diffusion where D is the diffusion constant, and
- the Capillary number $\mu U/\gamma$ relating viscous and interfacial forces, which is not strictly a function of L, though microfluidic systems by virtue of their size often have a characteristically small U value.

In microfluidics the result of a characteristically small L is that, compared to macroscopic length scales, viscosity, interfacial forces and diffusion tend to dominate fluid flow characteristics in microfluidic systems [10]. One of the most significant impacts of low Reynolds and Péclet numbers is the minimal fluidic mixing that naturally occurs, with Reynolds numbers typically on the order of $\mathcal{O}(1)$ or less preventing chaotic advection through turbulence. However, while this may be an advantage for many applications, passively keeping different species and reagents on-chip spatially separated with only diffusion gradients determining reagent dispersal, it is often desirable to have control over the mixing location and time. For this to be accomplished hydrodynamically on small length scales, methods have developed that fold, twist or warp the flow to increase the surface area between layers of different fluid species, as shown in Fig. 2.3, allowing diffusion to completely mix the fluid.

Similarly, the dominance of interfacial forces, especially surface tension, results in low capillary and Weber numbers that present both challenges and opportunities for manipulation in microfluidic devices. Liquid dispensing and handling become more problematic at the micro-scale; for example, it is essentially impossible to discretely 'pour' nanoliter volumes, with water and most other fluids spontaneously forming discrete droplets in air that are orders of magnitude larger. On the microfluidic scale, this difficulty has been overcome using a variety of methods, using a locally applied field to reliably dispense picoliter and femtoliter droplets [53, 54, 27, 55]. However, the dominance of surface tension also permits other activities such as the discrete handling of small fluid volumes or self-filling of microfluidic chambers through capillary action, shown in Fig. 2.4. By encasing finite fluid volumes within a segmented flow several advantages are realized when utilized in a microfluidic system, many of which are elaborated in the following section.

2.2.1 Droplet based microfluidics

Because of the relative dominance of surface tension, it is possible to segment fluid into a number of droplets of a defined volume. In the case of fluid flow in a closed channel, droplet based microfluidics is a subset of microfluidics whereby flow is segmented by the mixture of two immiscible fluids so that individual droplets of one fluid phase is entirely surrounded by another, for example water in oil. There are several advantages are conferred in the use of these droplets. By reducing the reagent volume yet further, smaller amounts of highly valuable reagents such as concentrated DNA or protein samples are required, while undesired concentration gradients that may

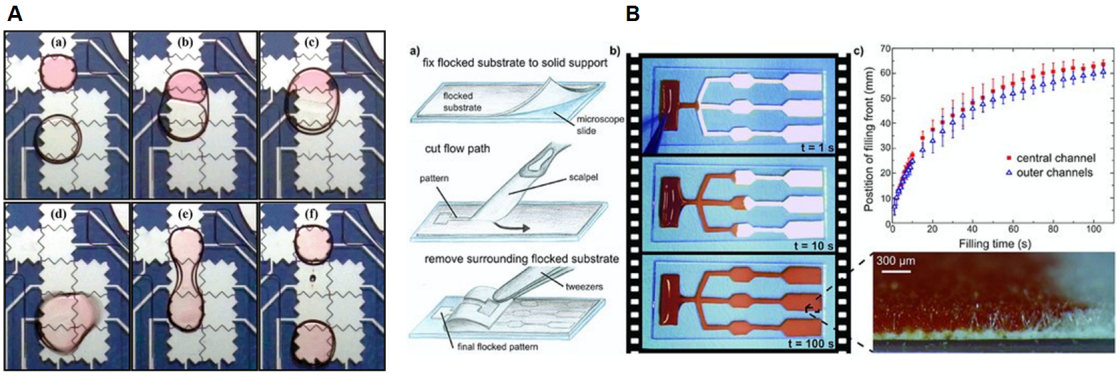

Figure 2.4: The relative dominance of interfacial forces such as surface tension allow for fluid handling and manipulation methods that are not feasible on a macro-scale. (A) Individual droplets, whose shape is maintained by surface tension, can be manipulated in an electrowetting array, including transport and mixing. (B) Similarly, interfacial forces allow the self-filling/pumping properties of micro-structured channels, with capillary wicking driving fluid flow. (A) Reproduced with permission from [56]. Copyright 2008, Royal Society of Chemistry. (B) Reproduced with permission from [57]. Copyright 2008, John Wiley and Sons

.

be present in a continuous-flow microfluidic system are avoided due to to an oil-water diffusion barrier. Additionally, again because of the dominance of surface tension at small length scales, the mixing between picoliter volumes is almost instantaneous with spontaneous merging of droplets in contact with one another occurring rapidly. But perhaps the most significant advantage, and one that is only relatively recently been explored, is the potential to make use of the compartmentalized and discretized flow on a microfluidic chip much as electrical signals are used in microelectronics, making possible what has been termed 'digital microfluidics' [56, 58]. In doing so, processes that might normally require large amounts of reagent and machinery, such as those involved in high-throughput screening (HTS) where the reaction between thousands of different compounds are analyzed, could be replicated on a microfluidic lab-on-a-chip, resulting in order of magnitude time and cost savings that are inherent to this platform. In the following paragraphs the techniques and principles fundamental to droplet-based microfluidics are discussed.

Fig. 2.5(A,B) demonstrates the fundamental principle for droplet creation in a microfluidic system, here showing (A) a T-junction and (B) flow focussing structure. In both, a continuous (oil) phase is mixed with a disperse (water) phase, resulting in spontaneous and controllable droplet formation, with the higher surface tension liquid (water) forming droplets in the lower surface tension (oil) one [59, 60, 61]. The droplet formation mechanism in these systems is determined by the capillary number of the continuous phase $Ca = \mu u_c / L$, where u_c is the flow rate of the continuous phase.

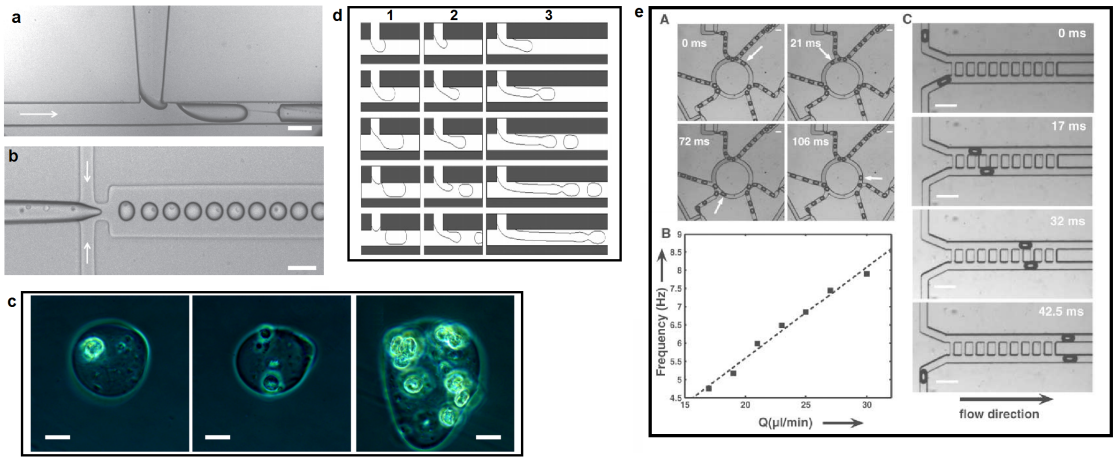

Figure 2.5: A microfluidic water-in-oil droplet is produced primarily using a microfabricated (a) T-junction or (b) flow-focussing geometry. (c) Individual droplets for discrete number of cells is an ideal system for a miniature bioreactor, simplifying analysis and cell handling. (d) The droplet breakup mechanism, which in part determines final droplet dimensions, can be described as the (1) squeezing, (2) dripping or (3) jetting regime, a function of the value of Ca_c. (e) Discretized fluid units form the basis for digital microfluidics, with hydrodynamic logic possible, here demonstrating (A) three AND gates in a ring oscillator and (C) a fluidic ladder for droplet timing synchronization. (a-c) Reproduced with permission from [59]. Copyright 2010, IOP Publishing. (d) Reproduced with permission from [62]. Copyright 2007, Cambridge University Press. (e) Reproduced with permission from [65]. Copyright 2007, The American Association for the Advancement of Science.

These mechanisms can be broadly defined as fitting into one of three regimes: squeezing dripping, or jetting, depending on the value of Ca. For low Ca values, droplet formation falls into the squeezing regime, where surface tension is dominant [62]. In the context of a T-juction, in this regime a incoming disperse phase enters and fills the entire width of the channel, with the pressure drop on either side of the nascent droplet resulting in the breakup of the thinning neck region at the orifice boundary, as shown in Fig. 2.5d(1). For $0.015 \lesssim Ca_c \lesssim 0.035$ droplet size drops off sharply in the dripping regime, with the disperse phase failing to fill the width of the channel prior to breakup (Fig. 2.5d(2)). For yet higher values of Ca_c, droplet breakup occurs with the formation of an unstable viscous thread which undergoes capillary breakup [63, 64], though droplet production in microfluidic lab-on-a-chip devices most often occurs in the squeezing, or sometimes dripping regime, where the droplet dimensions can be more rigorously controlled.

For the implementation of a device that confers the same relative abilities as a digital electronic device, the ability to address and control the path of individual droplets is required. Digital logic, with microfluidic AND, NAND OR and XOR gates (basic logic operators) has been demonstrated

in microfluidic devices through the use of clever geometries [66, 65, 67, 68, 69], though are limited in either their compatible fluids, range of allowable throughput, and actual addressability of individual droplets. Without active control, the range of functions allowable on such a platform are limited, with suitable applications restricted to those in which the same activity is required to be repeatedly performed. With this in mind, several methods have been developed to individually control droplet trajectories and pathways based on feedback-control mechanisms, including pneumatic valves [69, 70, 71, 72], optical methods [73, 74], electrokinetic forces [75, 76, 77] and acoustic forces [78, 79, 80, 81]. For full versatility in controlling the timing and location of droplet kinetics, pressure gradients used to drive droplet formation should also be actively controlled. To this end, active methods have been used for on-demand microfluidic droplet generation [80, 82, 83, 84, 85], though most require external, rather than on-chip generation of pressure gradients, with limited ability to combine these gradients with other useful on-chip abilities, a shortcoming that is addressed in Chapter 5, where SAW is used to generate microfluidic water-in-oil droplets on-chip. These and other microfluidic actuation methods are discussed and compared in the following section.

2.2.2 Actuation methods

The on-demand, tunable manipulation of fluid flow, droplets, cells and particles requires active control on-chip, with several techniques developed that make use of different forces that are relevant on the micro-scale, including magnetic, optical, electrical and high frequency acoustic forces. These forces are applicable to microfluidic systems because they are near-field, with force magnitude dropping off over larger length scales due to attenuation or inherent field properties. Because they are non-contact, these forces can also potentially be generated external to the actual microfluidic channels. Active control on microfluidic platforms has been demonstrated for a wide variety of processes that are applicable to microfluidic species, including sorting and size discrimination [86, 87, 88, 75, 79, 89, 36], single-cell and biomolecule manipulation [16, 90, 47, 91, 17], concentration [92, 93, 94, 95], mixing [94, 96, 43, 72] and cell treatment including transfection [37, 97], lysis [98, 99] and cell patterning and culturing [100, 101, 102, 103, 104]. While there are a wide variety of techniques used to perform these procedures, and an equally wide range of applications that they could conceivably be applied to, there are applications for which each technique is well

suited. It is important to choose the technique employed for the required device qualities, including throughput, magnitude of force, ability to localize this force, flexibility and tunability, ability to integrate with other microfluidic components in addition to economic considerations such as cost of materials, manufacturing time and assembly ease. Some common microfluidic techniques and their comparative advantages and disadvantages are given in Table 2.1, with examples of each shown in Fig. 2.6. Active methods are contrasted with hydrodynamic ones in that hydrodynamic manipulation techniques, while potentially performing sophisticated individual processes, are limited in their flexibility and tunability, unless of course active control in terms of flow rate modulation or on-chip gating is applied.

Table 2.1: Microfluidic actuation methods

Technique	**Force**	**Scaling**	**Advantages**	**Disadvantages**	**Examples**
magnetic	magnetophoretic force	$F \sim R^3$, $\Delta\chi$	Simple, inexpensive, passive use of magnets possible	weak force, throughput/specifity tradeoff, limited application (magnetic species/fluid required)	[105, 106, 107, 108, 109]
optical	optical tweezers	$F \sim R^{3,6}$, $\Delta\varepsilon$	high spatial resolution, high speed and responsiveness, high specificity,	low throughput, cell damage and photobleaching, complicated and sensitive setup required	[87, 73, 110, 88]
acoustic	acoustic pressure	$F \sim R^{3,6}$, $\phi(\rho,\beta)$	high throughput, large forces	integration difficulties with devices, large wavelengths will mean small effect on cells	[111, 79, 112, 25, 81, 16]
electrical	dielectrophoretic force	$F \sim R^3$, $\Delta\varepsilon$	high throughput	high voltages required, relatively small force, local heating,	[113, 90, 114, 115, 116]
passive	hydrodynamic force	$F \sim R, \rho$	high throughput, simple	low specificity, only simple or single activities possible	[117, 118, 119, 86]

Active techniques differ more fundamentally, however, in the types of force and force scalings that are applied, which can limit what microfluidic species the technique can be reasonably applied to. Electrical and optical manipulation methods, for example, can apply differential force based on size or electrical permittivity differences $\Delta\varepsilon$ [123, 124] or (closely related) differences in magnetic susceptibility $\Delta\chi$ [125]. Also, though most fluids exhibit observable paramagnetism at high enough field strengths, magnetic forces are limited to cases where magnetic particles or

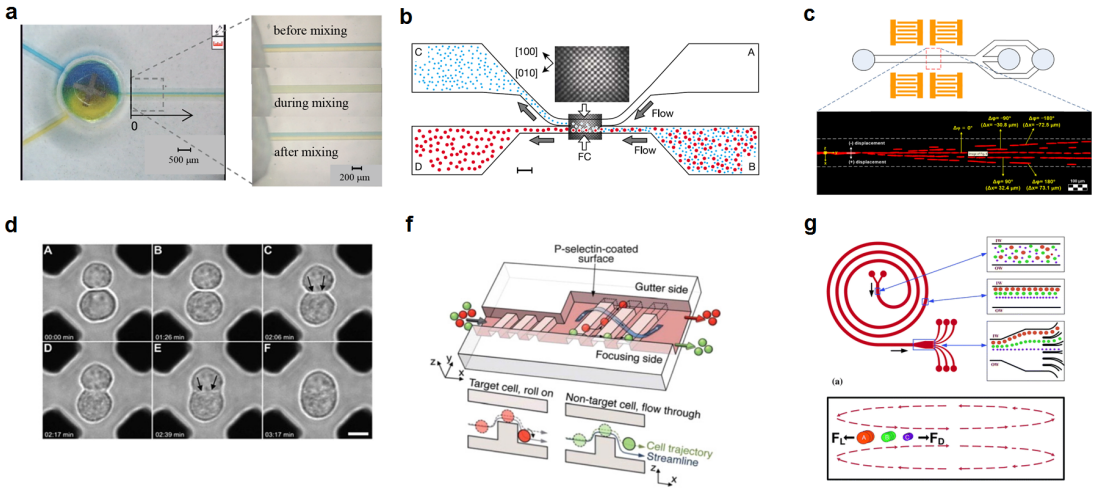

Figure 2.6: A variety of actuation methods and forces are used in lab-on-a-chip systems for manipulating microfluidic species. Different actuation methods can be used to perform a range of activities, including (a) magnetically controlled mixing, (b) optical separation, (c) acoustic sorting, (d) electrical cell membrane fusion and hydrodynamic sorting using either (e) deterministic rolling or (f) inertial separation. (a) Reproduced from [120]. Copyright 2007, IEEE. (b) Reproduced with permission from [87]. Copyright 2003, Nature Publishing Group. (c) Reproduced with permission from [121]. Copyright 2014, Elsevier. (d) Reproduced with permission from [48]. Copyright 2012, The Royal Society of Chemistry. (e) Reproduced with permission from [86], Copyright 2012, The Royal Society of Chemistry. (f) Reproduced with permission from [122], Copyright 2009, The Royal Society of Chemistry.

fluids are involved, so that the requisite field can be generated by a passive magnet or small electromagnet. Where this is not the case, other forces such as electrical ones can be applied, which can be more readily pattered and localized on-chip without as much danger of far-field effects; the dielectrophoretic (DEP) force drops off rapidly outside of the immediate vicinity of an electrode [126].

However, in cases where the permittivity of the medium and the particle or cell are similar, or there is little difference in the electrical properties between two species for which separation is required, yet other techniques are required. Acoustic forces fulfill this role well, being similarly non-contact and offering the same force scaling with particle dimensions as optical methods (where the traveling optical/acoustic wave force scales with R^3 and a standing wave with R^6), while being the only active control method that differentiates on mechanical properties rather than electrical ones. This is relevant for certain applications such as the sorting of infected malarial cells from noninfected ones, where there is only a fractional difference in electrical permittivity [127], but a ten-fold difference in mechanical stiffness [128].

Similar to electrical forces, acoustic forces have also proven to be very versatile when applied on chip, having been used for activities as varied as mixing [94, 25], concentration [15, 129], atomization [35, 34], pumping [130, 131], droplet production [132, 83] and on-chip microcentrifugation [133]. The limiting factor in applying these forces to microfluidic systems has been their (1) ability to arbitrarily localize forces and (2) ease of integration within a microfluidic device. In some of the first iterations of these acoustic microfluidic devices a bulk piezoelectric transducer was affixed to a stiff substrate such as silicon which contains the fluid chambers [134]. However, while functional as an individual unit, unforseen and undesired effects on other processes may occur when integrating this as a module into a complete lab-on-a-chip. To address these and other issues, a relatively new method for on-chip acoustic manipulation has garnered increasing attention, called surface acoustic waves (SAW).

2.3 Surface acoustic waves (SAW)

It is a property of a piezoelectric material that, when an electrical potential is applied, a mechanical expansion or contraction is produced. This principle and its converse, where a mechanical displacement produces a charge separation, has been known since the latter part of the 19th century [135]. While the effect has been known for some time, it was not until it was applied to the generation of acoustic fields, where a piezoelectric is actuated at a given electrical frequency to generate an oscillating acoustic field, that these materials found widespread use. Today the diverse applications of piezoelectrically generated acoustic fields include underwater depth sounding, medical imaging, non-destructive testing and, of course, microfluidic devices. A SAW is a special type of acoustic wave that, rather than resulting from the bulk vibration of a material, travels exclusively in the vicinity of its surface. SAW devices were initially developed for the telecommunication industry, where they continue to serve as bandpass filters for RF devices [136]. SAW has only recently found application in lab-on-a-chip microfluidic devices, where SAW has substantial advantages over other methods for generating acoustic fields. Some of these are listed in the following points: (1) The mechanical displacement is concentrated at the material interface – often the piezoelectric substrate and water – resulting in efficient energy transfer into the fluid. (2) The acoustic wavelength of typical SAW devices for microfluidic applications range from the size of larger microfluidic channels ($\sim$300 μm) [111] to that of the smallest cells ($\sim$1 μm), a result of

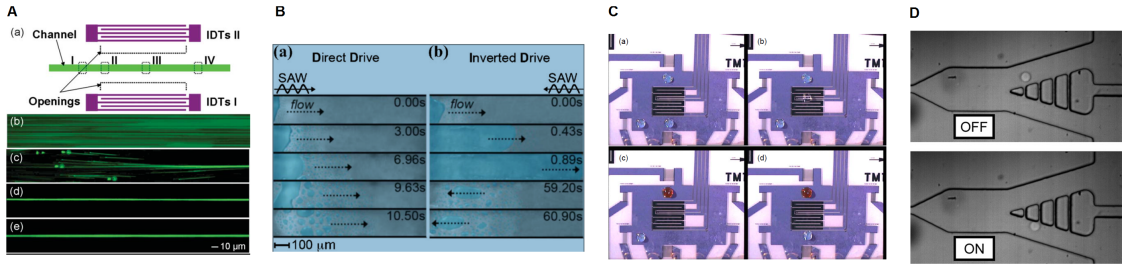

Figure 2.7: Acoustic fields generated by SAW have found use for a diverse range of microfluidic applications, including (A) concentration, (B) pumping, (C) sessile droplet transport, and (D) oil-water droplet sorting. (A) Reproduced with permission from [111], Copyright 2008, The Royal Society of Chemistry. (B) Reproduced with permission from [141]. Copyright 2008, AIP Publishing LLC. (C) Reproduced with permission from [142]. Copyright 2006, SAGE Publications. (D) Reproduced with permission from [78], Copyright 2009, The Royal Society of Chemistry.

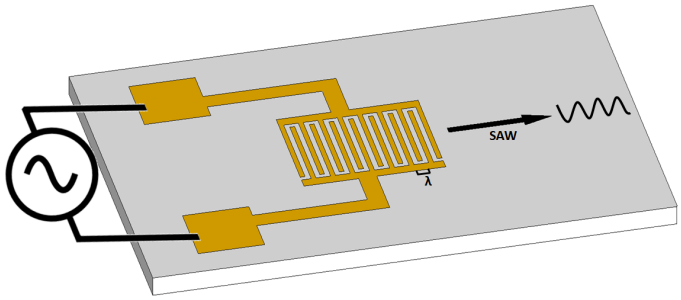

Figure 2.8: A SAW device is comprised of a piezoelectric substrate on which a series of interdigital transducers (IDTs) are arrayed. When excited at its resonant frequency, these IDTs produce a wave that will travel directionally along the substrate surface.

the large frequency (10 MHz–10GHz) at which these devices are actuated [137]. (3) These devices are planar, composed of a series of metal interdigital transducers (IDTs) patterned on a flat piezoelectric substrate, and therefore easily integrated with similarly planar microfluidic platforms through direct channel bonding [138] or channel etching in the substrate itself [139]. Additionally, a superstrate can be used, with a viscous layer coupling energy from the the piezoelectric to a separate microfluidic device on top, obviating the need to integrate channels directly on top of the piezoelectric material [140]. These and other advantages have seen this technology used for a diverse range of applications, some of which are depicted in Fig. 2.7.

2.3.1 Principles

A representative SAW device is depicted in Fig. 2.8. To generate a SAW, a series of interdigital transducers (IDTs) are arrayed on a piezoelectric substrate. When an AC signal is applied across the pair of electrodes at the resonant frequency of the IDTs such that the surface displacement

emanating from each finger-pair is reinforced by the subsequent one, a SAW that will continue to propagate across the substrate orthogonal to long-axis of the IDTs. The frequency, f, of this resonant condition is given by

$$f = \frac{c_s}{\lambda_{SAW}}, \tag{2.1}$$

where c_s is the SAW phase velocity of the piezoelectric material and λ_{SAW} is the resonant wavelength of the IDTs. In the most straightforward IDT configuration, each strip of metal in an IDT is $1/4\lambda_{SAW}$ wide. Other IDT configurations are possible, however; split-finger [143] and single phase unidirectional IDTs [144, 145] have the advantages, respectively, of a more uniform bandpass region (defining the range of resonant frequencies) and unidirectional propagation. Additionally, any IDT configuration can be patterned to shape the resulting field or its frequency range as desired, including focussed patterns [146], which confer a concentrated region of surface displacement, chirped [91] and slanted finger patterns [147], both of which yielld a large range of resonant frequnecies by virtue of their varying IDT finger dimensions. These configurations and patterns are shown in Fig. 2.9. The most common piezoelectric material used for SAW microfluidics is lithium niobate ($LiNbO_3$), optimal for this application because of its high spontaneous polarization and electromechanical coupling coefficient [148, 149] and low inherent acoustic attenuation [150].

When a SAW traveling along a piezoelectric substrate encounters a body of fluid on top of it, energy will radiate from the substrate into the fluid in the form of an acoustic wave at the Rayleigh angle θ_R, defined as the angle of propagation into the fluid from a direction normal to the substrate surface [35], given by

$$\theta_R = sin^-1 \left(\frac{c_f}{c_s} \right), \tag{2.2}$$

where c_l is the sound speed in the fluid. In 128° YX-cut lithium niobate, $c_s \approx 3960$ m/s [151], $c_f \approx 1480$ at room temperature, resulting in $\theta_R \approx 22°$. In the case of a pure standing wave, however, energy radiates vertically into the fluid. The existence of a traveling or standing wave in a system is a function of the system design. As shown in Fig. 2.10, a traveling SAW is the result of a single set of IDTs whereas a standing wave is produced through the superposition of two incident travelling waves. Typical microfluidic systems using SAW can be further broken up into open (Fig. 2.10c) or closed (Fig. 2.10d) formats, with the design chosen depending on

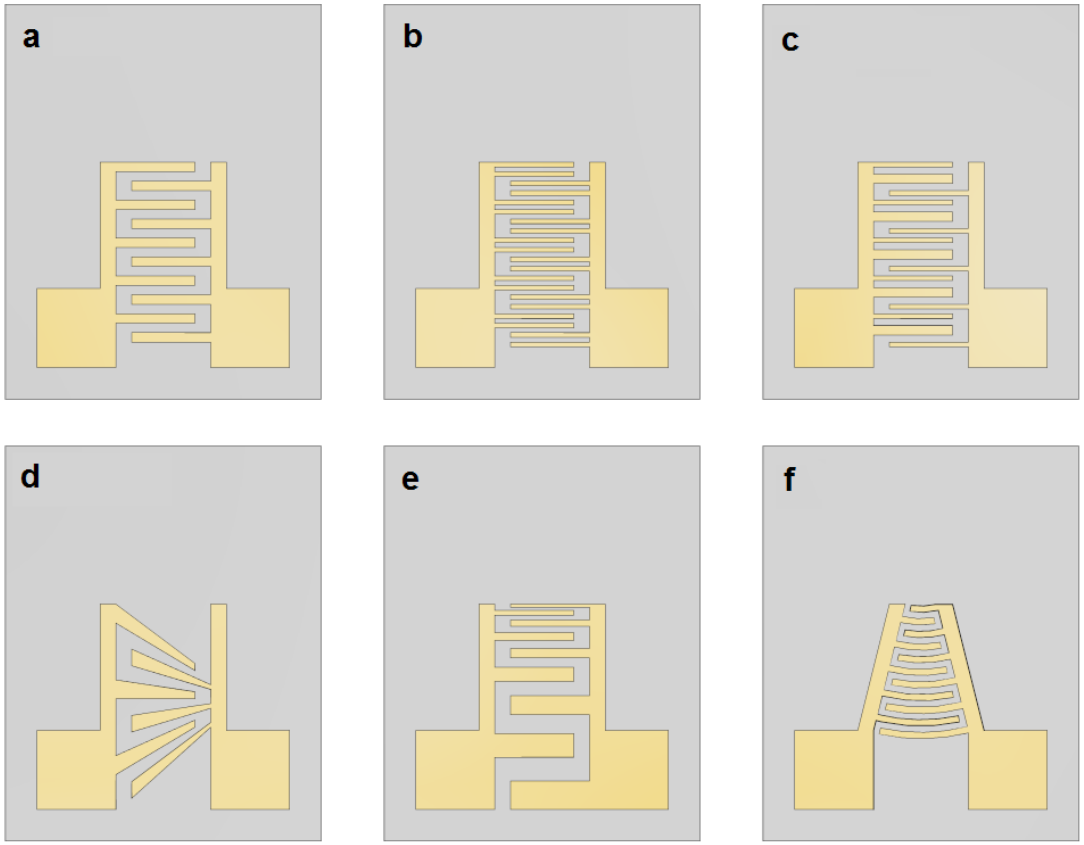

Figure 2.9: An advantage of SAW is that there are several different IDT configurations and patterns that can be used to achieve the desired frequency or field shape characteristics. (a) Normal IDTs, (b) split-finger IDTs and (c) single-phase unidirectional IDTS are some of the more common IDT configurations, which can be further modified into (d) slanted finger, (e) chirped and (f) focussed IDTs patterns.

the intended application. In an open-microfluidic electrowetting array, for example, SAW can be used for droplet translation [152] and applied to closed microfluidic systems for applications that require constant throughput [101] or those that contain two fluid phases for droplet-based microfluidics [79]. Regardless of the configuration, all SAW microfluidic devices make use of an acoustic wave that propagates through a body of fluid. These devices make use of one or both of the following effects: (1) when this fluid interacts with an interface, including those of immersed particles, a time-averaged pressure is produced on that interface or particle and (2) the attenuation of the displacement amplitude as the acoustic wave propagates creates a momentum flux that, in a fluid, results in acoustic streaming [153]. These two effects are discussed more thoroughly in the next two subsections.

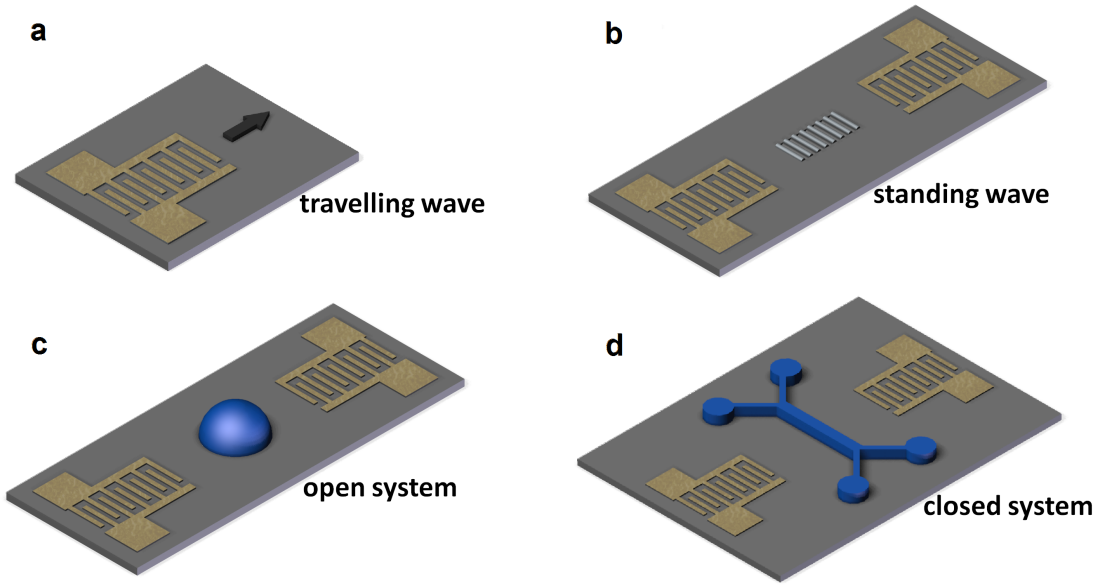

Figure 2.10: SAW microfluidic systems make use of both (a) traveling and (b) standing wave setups, the latter showing a part of the region where a standing SAW exists. Either traveling or standing waves can then be applied to either (c) open, or droplet-based systems, or (d) closed channel-based systems whose boundaries are defined by channels bonded onto the substrate, both of which are shown here in a standing wave setup. The use of either traveling waves or standing waves in an open or closed microfluidic system depends on the intended application.

2.3.2 Acoustic pressure

Acoustic pressue is the mechanism fundamental to the operation of many microfluidic systems using SAW, such as on a water-air interface where fluid drops can be translated on a level surface [94]. Similarly, pressure on a water-oil interface is required for the manipulation of droplets in closed systems [79]. In this section the theory of acoustic radiation pressure is presented. There are two central definitions of acoustic radiation pressure, which are applied depending on the nature of the system concerned. Rayleigh radiation pressure refers to the time-averaged pressure induced by acoustic waves which are incident on an interface in a confined chamber, while Langevin radiation pressure is the time-averaged pressure on a wall in an unconfined chamber [154], depicted in Fig. 2.11. The effect of the confined chamber in the case of Rayleigh radiation pressure is to introduce an additional hydrostatic pressure term proportional to the square of the displacement amplitude [155]. The difference in pressures recorded at each absorber in Fig. 2.11 is due to the different reference pressures; in an unconfined chamber this is the pressure of the fluid directly behind the absorber, while in a confined chamber this is the pressure of the unperturbed fluid at

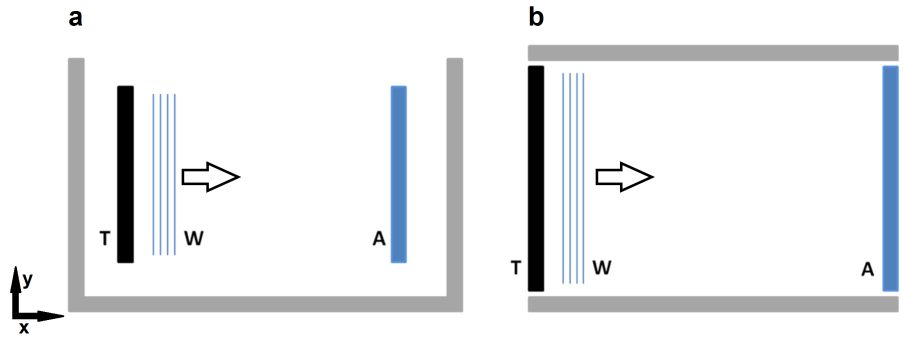

Figure 2.11: Configurations of for the production of (a) Langevin and (b) Rayleigh radiation pressures. In both cases a transducer (T) produces waves (W) which are incident on the absorber (A).

rest.

The Langevin radiation pressure can be found by adapting the methodology from Rooney & Nyborg [156]. If F is the force acting on a body bounded by an arbitrary surface S enclosing a body with density ρ and fluid velocity v, then F can be defined by eularian mass conservation:

$$F = \frac{\partial \rho v}{\partial t} - \int_S \rho \mathbf{v}(\mathbf{v}\cdot\mathbf{n})\, \mathrm{d}S \tag{2.3}$$

Where $\partial \rho \mathbf{v}/\partial t$ is the rate of change in momentum, and the integral over S represents the transport of momentum across S. Assuming F and $\mathbf{v}$ are collimated along the x-axis as shown in Fig. 2.11, and letting $\mathbf{i}$ be the unit vector in the x-direction, then

$$\mathbf{v} = v\mathbf{i}, \tag{2.4}$$

$$F = \frac{\partial \rho v}{\partial t} - \int_S \rho v^2(\mathbf{n}\cdot\mathbf{i})\, \mathrm{d}S. \tag{2.5}$$

Integrating this across the surface S, we have

$$F = \frac{\partial \rho v}{\partial t} + \left(\rho v^2\right) s. \tag{2.6}$$

Because we wish to find the steady-state pressure incident upon the interface, the time average of the equation components is taken. Because the time dependent term of Eq. 2.6 at steady state is equal to zero, this equation can be written as:

$$F/s = P_l = \langle \rho v^2 \rangle \tag{2.7}$$

Where F/s is simply the force per area, P_l is the Langevin radiation pressure and $\langle\rangle$ denotes a time averaged quantity [156]. As $\langle \rho v^2 \rangle$ is equivalent to the total acoustic energy in a unit volume [153], Langevin's result, $P_l = E$ holds true. For the case of a sinusoidally oscillating driving force, P_l can be further be decomposed and represented as

$$P_l = \langle \rho v^2 \rangle = \frac{1}{T} \int_0^T \rho v^2 \, \mathrm{d}t = \frac{1}{2} \rho \omega^2 \xi_0^2, \tag{2.8}$$

where ω is the frequency of oscillation and ξ_0 is the displacement amplitude of the oscillator. Given that the velocity of the oscillator can be written as $v_0 = \omega \xi_0$, the Langevin radiation pressure can then be written as $P_l = \frac{1}{2} \rho v_0^2$.

The Rayleigh radiation pressure is similar to Langevin's result, though adds a hydrostatic pressure term resulting from the nonlinear propagation of an ultrasonic acoustic wave through a media, whose nonlinearity parameter, B/A comes from the first two terms in the taylor series expansion of the equation for the instantaneous change in pressure [157], given by the Taylor series expansion

$$p - p_0 = A \left(\frac{\rho - \rho_0}{\rho_0} \right) + B/2 \left(\frac{\rho - \rho_0}{\rho_0} \right)^2 + \cdots, \tag{2.9}$$

where B and A represent the nonlinear modulus and A the adiabatic bulk modulus [158]. Here, larger values of B/A represent fluids which are more strongly nonlinear, and will thus have a larger hydrostatic static pressure component..

From Rooney [156], the Rayleigh radiation pressure under the influence of sinusoidal oscillation is:

$$P_r = \left[1 + \frac{B}{2A} \right] \langle \rho v^2 \rangle = \left[\frac{1}{2} + \frac{B}{4A} \right] \rho v_0^2 \tag{2.10}$$

Where P_r is the Rayleigh radiation pressure. Given that B/A for water is 5.0, the Rayleigh pressure in water is given by $P_r = \frac{7}{4} \rho v_0^2$.

While these relationships hold for the interaction between a traveling wave and a planar surface much larger than the acoustic wavelength, different relationships hold where the object acted on

is on the order of the size of the acoustic wavelength or smaller. For a traveling acoustic wave interacting with a particle for $R \ll \lambda$, the acoustic force was deduced by King [159] as

$$F_{tw} = 64\rho \left(\frac{\omega}{c}\right)^4 R^6 v_0^2 \frac{1+\frac{2}{9}(1-(\rho/\rho_p)^2)}{(2+\rho/\rho_p)^2} \tag{2.11}$$

In the case of a standing wave field, characterized by zero phase velocity, however, motion is restricted to within one half of the acoustic wavelength where the particles collect at the acoustic pressure nodes or antinodes, depending on whether the acoustic contrast factor $\phi > 0$ or $\phi > 0$, with the standing wave acoustic force F_{sw} on the particle given by

$$F_{sw} = -\left(\frac{\pi P_0^2 V_p \beta_f}{2\lambda}\right)\left(\frac{5\rho_p - 2\rho_f}{2\rho_p + \rho_f} - \frac{\beta_p}{\beta_f}\right) sin(2kx), \tag{2.12}$$

where p_0 is the pressure amplitude, V_p the particle volume, λ the wavelength, ρ_f and ρ_p the density of the fluid and particles, μ the viscosity and β_p and β_f are the compressibility of the particle and medium. The sin term reflects the periodicity of the pressure field, repeating every $k/2$ in the x direction, where $k = \omega/\lambda$ is the wavenumber. The force scaling between a traveling and standing acoustic wave differs primarily with respect to the particle dimensions, with R^6 in Eq. 2.11 and R^3 in eq. 2.12. The applicability of these forces in microfluidic systems is discussed later in Section 2.4.3. However, direct acoustic pressure on particles and interfaces is not the only acoustic phenomena that can be exploited; the nonlinear propagation of a compressional wave through a fluid medium will also result in motion of of the fluid itself, called acoustic streaming, which is described in the following section.

2.3.3 Acoustic streaming

The propagation of an acoustic wave through a physical medium produces a second-order nonlinear body force, namely a force acting much like gravity through the bulk of the fluid, in the direction of wave propagation resulting in local fluid flow. This flow is called *acoustic streaming*, or *quartz wind* when the fluid through which the acoustic wave propagates is air [10]. The ability for acoustic waves propagating through a fluid medium to induce momentum flux was first observed by Lord Rayleigh when examining a standing wave field between two plates [160]. Fluid flow driven by acoustic streaming has since been utilized for microfluidic mixing, centrifugation and pumping [137]. Recirculation in a droplet driven by acoustic streaming is depicted in Fig.

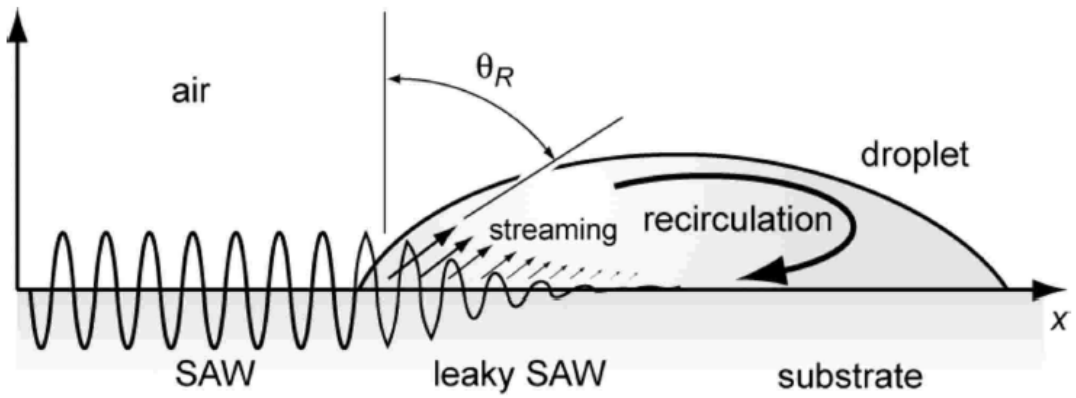

Figure 2.12: A SAW incident on a fluid body will undergo amplitude attenuation, transferring acoustic energy to the fluid with the resulting wavefronts propagating at the Rayleigh angle θ_R. Attenuation of the acoustic beam in the fluid itself gives rise to a momentum flux, with this momentum transfer resulting in a bulk fluid motion known as acoustic streaming. Reproduced with permission from [25]. Copyright 2009, AIP Publishing LLC.

2.12. The principle advantage of acoustic streaming in microscale systems over other methods are the lack of moving parts. Pumping, for example, has traditionally been accomplished pneumatically with bulk fluid pumps, though the drive toward small-scale devices has driven research into methods compatible with microscale fabrication, leading to the development of electrohydrodynamic [161] and acoustic [162, 163] microfluidic pumping methods. Of these methods, acoustically derived flows can be driven to higher velocities while requiring significantly lower voltages and without the need for a charge carrier in the fluid [25]. Acoustic pumping has been accomplished with thickness mode vibration [164, 165, 166], flexural plate waves [163, 167] and surface acoustic waves (SAW) [168, 142]. Though these methods differ in their fabrication, frequency range and suitable applications, their fundamental mechanism of action in generating fluid flow via an acoustically generated body force is the same.

An understanding of acoustic streaming is important when making use of acoustic fields in microfluidic systems, where acoustic streaming will always be present in some form, even if it is not desired. To enhance this understanding, this streaming mechanism is described in the following sections.

Acoustic streaming is the result of the nonlinear propagation of sound waves through an elastic medium, whereby the advancing compressed phase of the wave travels faster than the dilated part, resulting in a net force in the direction of wave propagation. The streaming force can be derived from newtonian mechanics, where the sum of all forces F acting on a control volume V is equal

to the change in momentum: Newton's second law [169]. If we define a control volume without respect to an external reference frame, it makes sense to formulate this law in terms of the material derivative, which is the change in a quantity γ that a given sampling point traveling through a field in which γ varies is determined. The general material derivative is

$$\frac{D\gamma}{Dt} = \frac{\partial \gamma}{\partial t} + \mathbf{u} \cdot \nabla(\gamma). \tag{2.13}$$

Applying the material derivative Newton's second law, we have

$$\frac{D}{Dt} \int_V \rho \mathbf{u} \mathrm{d}V = \int_V F \mathrm{d}V. \tag{2.14}$$

When we eliminate the integrand and fully expanding the left hand side this equation equation,

$$\frac{\partial(\rho \mathbf{u})}{\partial t} + \mathbf{u} \cdot \nabla(\rho \mathbf{u}) = F, \tag{2.15}$$

which when expanded takes the form

$$\mathbf{u}\frac{\partial \rho}{\partial t} + \rho \frac{\partial \mathbf{u}}{\partial t} + \rho(\mathbf{u} \cdot \nabla)\mathbf{u} + \mathbf{u}\nabla \cdot \rho \mathbf{u} = F. \tag{2.16}$$

Because the body force producing acoustic streaming is a time-averaged phenomena, it makes sense to take the time-average of equation (2.16) to find the force, arriving at the same result as others [170, 171, 172]. Here the time average is denoted by $\langle\rangle$ and with the body force being

$$F = \langle \rho(\mathbf{u} \cdot \nabla)\mathbf{u} + \mathbf{u}\nabla \cdot \rho \mathbf{u} \rangle. \tag{2.17}$$

Note here that the time-average of F results in dropping of all $\frac{\partial}{\partial t}$ terms. This result is equivalent to that derived from Lighthill [153], who derived the body force alternatively in terms of the Reynolds stress σ, with

$$\sigma = \overline{\rho u_i u_j}, \tag{2.18}$$

where the body force is given by the spatial gradient of the Reynolds stress, or momentum flux, in the x_1, x_2 and x_3 direction, represented in Einstein notation as

$$F_j = -\frac{\partial \overline{\rho u_i u_j}}{\partial x_i}. \tag{2.19}$$

This alternative definition is equivalent to equation (2.16) in that the body force is defined as the change in momentum flux, and can be expanded to yield the same result as equation (2.17). Equation (2.17) can be further simplified by making use of the continuity equation, which (at steady state) sets

$$\nabla \cdot \rho \mathbf{u} = 0. \tag{2.20}$$

Applying this equation to the previously derived definition of the body force yields the following relationship, used by others [173, 10, 174]

$$F = \langle \rho(\mathbf{u} \cdot \nabla)\mathbf{u} \rangle. \tag{2.21}$$

The streaming force resulting from a decaying substrate wave vibration as in SAW can be found by including a measure of the attenuation of the particle velocity in the fluid with a corresponding attenuation of the SAW on the water-loaded piezoelectric substrate. This velocity, in the x-z plane, is given by [171]:

$$\begin{aligned} u_x &= \xi_0 \omega e^{(\mathrm{j}\omega t)} e^{(-\mathrm{j}k_L x) exp(-\alpha k_L z)} \\ u_z &= -\mathrm{j}\alpha \xi_0 \omega e^{(\mathrm{j}\omega t)} e^{(-\mathrm{j}k_L x) exp(-\alpha k_L z)} \end{aligned} \tag{2.22}$$

where ξ_0 is the maximal surface displacement, the SAW number $k_L = k_r + \mathrm{j}k_i$ is a constant with the imaginary k_i component representing the attenuation of a leaky SAW when loaded with later [175] (as opposed to a Rayleigh type SAW without water loading with an attenuation coefficient of only k_r) and

$$\alpha = \sqrt{1 + \left(\frac{c_s}{c_l}\right)^2} \tag{2.23}$$

The streaming force $|\boldsymbol{F}|$ can then be calculated using $|\boldsymbol{F}| = \sqrt{F_x^2 + F_z^2}$ from the pythagorean theorem. Applying (2.22) to equation (2.17), the body force is found to be:

$$\boldsymbol{F} = -\rho_0 (1 + \alpha_1^2)^{3/2} \xi_0^2 \omega^2 k_i e^{(2k_i x + 2\alpha_1 k_i z)} \tag{2.24}$$

Here, the body force at any point (x, z) is determined by the coupling at the solid-fluid interface $\alpha_1 = j\alpha$ and the attenuation of the traveling surface wave under water loading k_i. Because of these

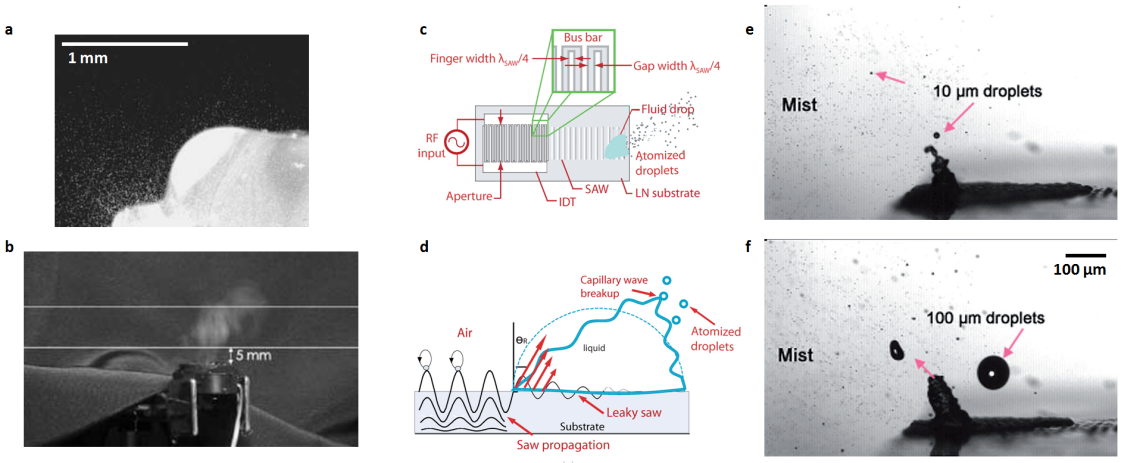

Figure 2.13: Atomization is the process through which capillary instabilities resulting from acoustic actuation result in droplet break-off from a larger liquid bulk. Shown here for a (a) a fluid atop a (b) bulk-mode vibrating transducer and a (b-f) SAW device. (b,c) In a SAW atomization system (e,f) droplets of different characteristic dimensions are produced. (a) Reproduced with permission from [177]. Copyright 2002, Springer. (b-f) Reproduced with permission from [35]. Copyright 2009, The Royal Society of Chemistry.

attenuation factors, the force in a given body of fluid of length scales greater than $\sim 10\lambda$ will not be of uniform magnitude throughout the path of the acoustic beam. It is this asymmetry which is utilized in some acoustic streaming applications such as microcentrifugation [176], separation and mixing [94] using SAW.

2.4 Relevant applications of SAW

These phenomena, acoustic pressure and acoustic streaming, are the mechanisms by which SAW is able to manipulate particles, cells and fluid interfaces in microfluidic systems. Some relevant applications demonstrating the manner in which these forces can be applied to microfluidic lab-on-a-chip and therapeutic systems, as well as existing gaps in the field that are addressed by the work in this thesis, are detailed in the following subsections.

2.4.1 Atomization

Atomization is the process by which a bulk fluid is converted to a distribution of water-in-air droplets. The ability to atomize fluids is important in for several high value applications, such as nebulization therapy, where a therapeutic agent is solubilized in a liquid whereafter the atomized droplets are inhaled for purposes such as drug delivery [35], and mass spectrometry [179].

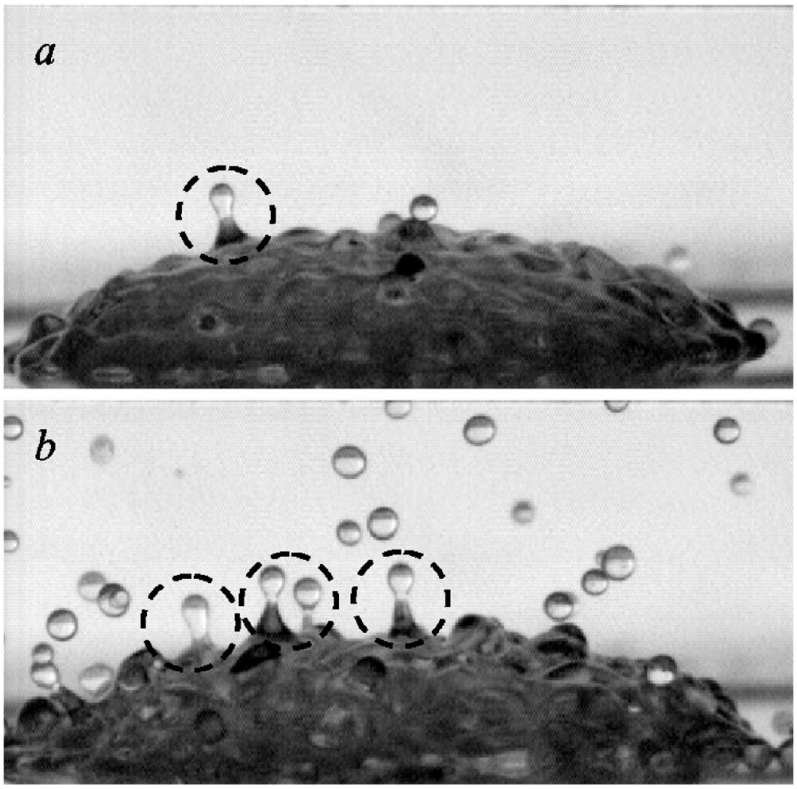

Figure 2.14: Images of droplet breakup. (a) Subthreshold capillary wave amplitude results in a vibrating surface, with no or few droplets produced. (b) Atomization occurs when the capillary stabilization forces are overcome in the presence of sufficient external forcing in the process of liquid thread formation and subsequent droplet pinch-off. Image reproduced with permission from [178]. Copyright 2007, AIP Publishing LLC.

There are currenly several atomization methods, including flow focussing [180], electrospraying [181] and ultrasonic actuation (including SAW) [182, 183]. Of these methods, actively controlled ultrasonic ones hold substantial promise for applications such as nebulization therapy, with the ability to accurately control timing, dosage and, with proper characterization and physical understanding, the size of the droplets produced. Two ultrasonic atomization concepts are shown in Fig. 2.13, making use of bulk acoustic waves (a,b) and SAW (c-f). Among acoustic actuation methods, SAW has the particular advantage of surface concentrated displacement resulting in efficient energy transfer into the fluid placed on top, as opposed to a bulk ultrasonic transducer which will invariably leak otherwise useful energy into its mountings and surrounds. This efficiency is particularly important for portable, point of care nebulization therapies [35].

In ultrasonic atomization, whether driven by SAW or a bulk transducer, droplet breakup occurs through a process of viscous-shear driven capillary wave excitation [35]. That is, the substrate wave vibrations are coupled into a fluid on top of it, driving capillary waves on the fluid surface, where the spectral density (the representative magnitude of different frequencies) of these waves is dictated by dissipative influences of wave turbulence [184]. When the the amplitude of these capillary waves is sufficiently high, a droplet is formed through the generation of a capillary instability in a liquid thread, with subsequent droplet pinch off creating one or more droplets; this process is visualized in Fig. 2.14. The threshold capillary wave amplitude for droplet formation is determined by the magnitude of the different physical parameters, given by [185, 186]

$$a_c \sim 2\frac{\mu}{\rho}\left(\frac{\rho}{\pi\gamma f_c}\right)^{1/3}, \tag{2.25}$$

where f_c is the capillary frequency. Of particular importance is the droplet size resulting from this breakup process, which determines which lung regions (trachea, bronchiole of alveoli) are targeted by nebulization therapy, with smaller droplets depositing in deeper lung regions. This wavelength has been previously determined from the Kelvin equations for capillary waves, given by [187]

$$\lambda = \left(\frac{2\pi\gamma}{\rho f_e^2}\right)^{1/3} \tag{2.26}$$

where f_e is the frequency of substrate excitation. Previous work with low frequency excitation suggested that this excitation frequency corresponds to the capillary frequency by the simple relationship $f_c = f_e/2$. For SAW, however, there is little reason to believe either the Kelvin equation

or this relationship hold, especially given the spectrally dispersive nature of wave propagation through nonlinear media at high frequencies [184] or the thin film nature of SAW atomization [34]. An analysis determining the capillary frequency would be best served in this case by analyzing the physical parameters which give rise to a characteristic capillary wavelength. In a thin film where the capillary stress in the vertical direction dominates over the horizontal one, as is the case in thin-film SAW atomization, this wavelength can be deduced from a viscous-capillary stress balance, with [188]

$$\frac{\gamma H}{L^2} \sim \frac{\mu U}{H} \tag{2.27}$$

where L and H are the relevant length and height length scales and $U \equiv \lambda f$. Rearranging gives the characteristic capillary wavelength

$$\lambda \sim \frac{\gamma H^2}{\mu f L^2}. \tag{2.28}$$

where the capillary wavelength is sensibly determined by the physical parameters underlying wave propagation. However, it is not clear in the literature what the relationship between λ and the resulting droplet size is. In Chapter 4, Eq. 2.28 is used as the basis for elucidating the parameters and relationships pertinent to estimating droplet size during SAW atomization. Understanding of the breakup mechanisms and parameters is relevant not only for the purpose of SAW atomization, but also for the formation of droplets for inkjet printing [25], biological sample preparation [189], and the formation of microfluidic droplets in two-phase lab-on-a-chip systems [27].

2.4.2 Concentration

Concentration in microfluidic systems is a highly important function for diagnostic applications, vastly increasing sensitivity and decreasing both reaction time and amount of reagent and sample required [190], all vital functions for a well-implemented lab-on-a-chip system. For example, the concentration of red blood cells from plasma is required for a variety of blood diagnostic procedures [191, 192]. While this step can be performed in a laboratory setting in a centrifugal system, working on the microscale presents challenges when attempting to perform similar processes, especially with regard to the difficulties in integrating micro-scale moving parts capable on generating sufficient force. SAW is well suited to the task of particle concentration, being non-contact

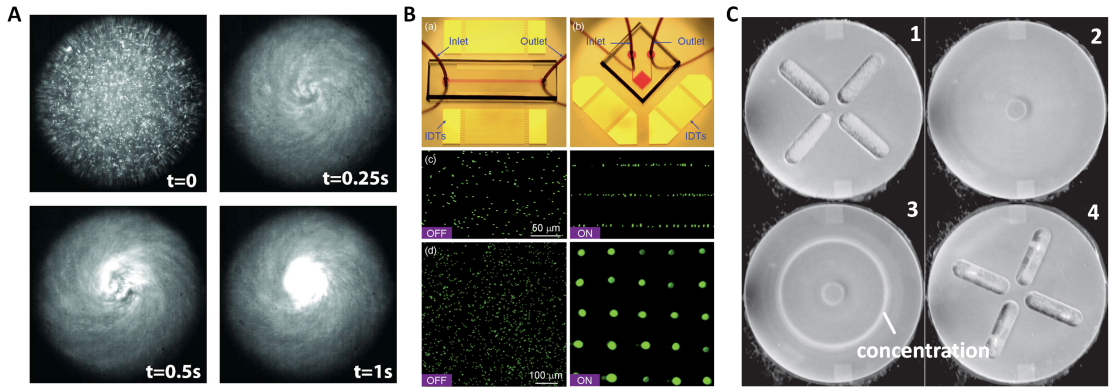

Figure 2.15: SAW particle concentration can be accomplished via several independent mechanisms. (A) Viscosity-induced shear stress results in particle migration to the center of a droplet actuated by asymmetrical acoustic streaming. (B) A standing wave acoustic force created by a set of opposing IDTs results in patterning of particles at the acoustic nodes in both a (a,c) 1D and (b,d) 2D field. (C) In a novel method, a small (mm-scale) disc is placed on a SAW device via a viscous coupling layer, and is induced to spin by asymmetric application of SAW. Concentration in this case is mediated by centrifugal forces. (A) Reproduced with permission from [94]. Copyright 2008, AIP Publishing LLC. (B) Reproduced with permission from [101]. Copyright 2009, The Royal Society of Chemistry. (C) Reproduced with permission from [194]. Copyright 2012, Wiley Online Library.

and not requiring moving parts. Three different mechanisms have been demonstrated for the purpose of particle concentration using acoustic forces. The most utilized methodology, especially for constant-throughput systems, relies on the application of a standing wave in a closed channel, where particles and cells are drawn to acoustic nodes and antinodes, as determined by the sign of their acoustic contrast factor [111, 16], where the acoustic force generated in the direction of this node or antinode was given in Eq. 2.12. Concentration is also possible in rotational systems driven by SAW. By generating acoustic streaming asymmetrically in a body of fluid to create rotational flow, particle migration to the vortex center occurs due to local shear stresses on particles [94, 193]. Alternatively, Glass et. al developed a novel method to incorporate a centrifugal mechanism for SAW particle concentration [194]. By placing a millimeter scale structure containing open channels on top of a SAW device, with energy transfer occurring via a liquid coupling layer, it was possible to spin this structure when a SAW is applied asymmetrically. With particles placed inside the rotating channels, particle concentration occurs via the centrifugal force due to the high rotational speeds (1000's of rpm) made possible [133]. Though this system is not strictly micro scale and may have only limited application, it is nonetheless an impressive display of how substrate displacements on the order of nanometers can be translated to continuous velocities measured in m/s.

However, despite the advantages SAW confers with regard to simple and effective on-chip concentration, there are currently gaps in the literature with regard to the ability to concentrate these particles using other mechanisms and in different systems that would enhance the versatility of SAW-based concentration. Traveling waves, for example, are especially suited to the task of concentration due to their long-range action; while a standing wave is only able to concentrate within half of an acoustic wavelength, a traveling wave can conceivably act over the entire length of a chamber and therefore concentrate a far greater amount of material. Similarly, applying these forces to concentrate particles in two-phase, oil and water systems, or creating suitable geometries for not only concentration, but also controlled on-demand particle and cell release, could make many new SAW-based digital microfluidic applications possible. In Chapters 5 and 6 these concepts are explored, where traveling SAW is used for particle concentration in both a two-phase system and for the controlled concentration, sorting and release of particles.

2.4.3 Sorting

The ability to sort between different particle and cell populations is a necessary function in many biomedical applications, with diverse examples including drug discovery [28], blood analysis [195, 15], cancer screening [196] and on-chip evolutionary assays [197, 198]. Here, different sorting methods are used based on their suitability for different tasks. Taking cancer screening as an example, high specificity in sorting is required, with circulating tumor cells (CTCs) – only a few microns larger and slightly stiffer than similar cells in the blood – requiring a method that is able to efficiently discriminate using only small differences in cell properties. On chip, sorting is accomplished using any of the methods discussed in Section 2.2.2, with sorting occurring either continuously, where different particle or cell types are acted upon differentially by a constantly applied force pervading the media in which they are suspended, or on an individual basis, where optical [197, 199], electrical [200] or acoustic detection [201] can be used to analyze microfluidic vesicles independently, whereafter a pulse of one of these external forces are applied. Which sorting paradigm is used depends on what properties are selected for, as well as the throughput and sensitivity specifications for an application. SAW has been used as an external acoustic force in both cases, where an acoustic field is either applied continuously or sporadically to selectively sort two populations [79, 202]. SAW has particular advantages for sorting in microfluidic systems, given the specificity with which the field can be localized and shaped, it's ability to be easily

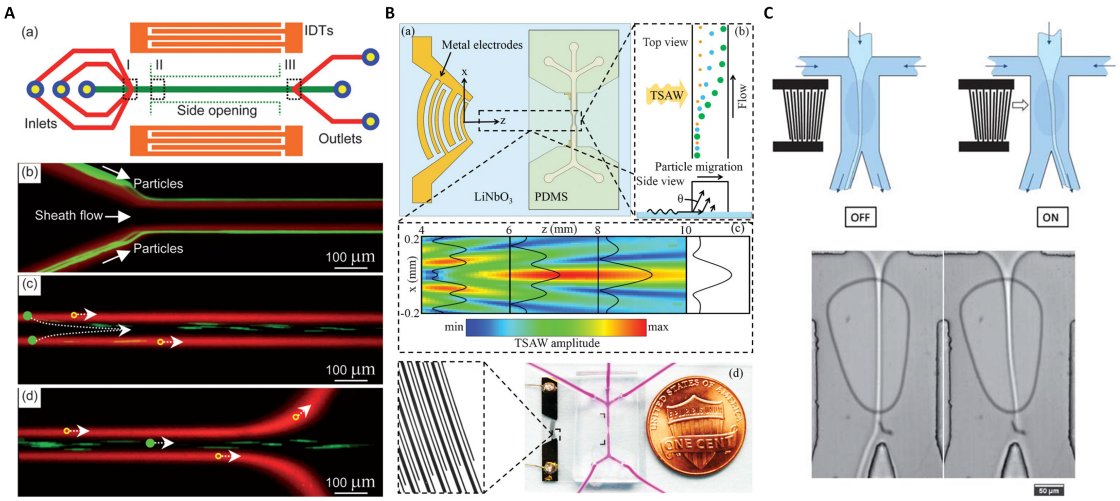

Figure 2.16: Particle separation and sorting using SAW is based on the differential force that is applied to different microfluidic species as determined by their different size or acoustic contrast. Separation of different particle sizes, for example, has been demonstrated using (A) standing wave SAW, with the acoustic force $F \sim R^3$ or (B) traveling waves, with $F \sim R^6$. (C) These forces can also be used for more generalized sorting, with particles, cells or fluid streams directed towards a desired outlet when a SAW is applied. (A) Reproduced with permission from [202]. Copyright 2009, The Royal Society of Chemistry. (B) Reproduced with permission from [203]. Copyright 2013, The Royal Society of Chemistry. (C) Reproduced with permission from [79]. Copyright 2010, The Royal Society of Chemistry.

integrated into planar microfluidic systems and perhaps most pertinently the ability to tune this sorting with its modifiable pressure amplitude and duration of application, from milliseconds up. SAW actuated sorting has been demonstrated using both standing wave and traveling wave forces: which force is dominant in a system is a function of the orientation, dimensions and layout of the IDTs and channels making up the device. In a standing wave, particles or cells migrate in half a SAW wavelength toward the nodes or antinodes of an acoustic pressure field depending on the sign of their acoustic contrast value, ϕ, with the force applied scaling with the size of the particle, $F \sim R^3$, as described in Eq. 2.12. Exposed to a traveling wave, sorting is a function of the lateral displacement in a given time period, with particles moving in the direction of SAW with larger particles exposed to a greater acoustic force with $F \sim R^6$, as described in Eq. 2.11. Examples of standing wave and traveling wave sorting are shown in Fig. 2.16.

On the face of it, traveling waves might seem the more sensible option for sorting, given the greater contrast in force between given particle sizes and the greater displacements that can be produced, not being limited to one-half of a SAW wavelength; in the standing wave SAW separation system demonstrated by Shi et. al [202] particles were more than 300% different in diameter.

However, it should be noted that the traveling wave force is typically weaker for micron-scale particles [204], and as a result it can be difficult to create a system where spurious standing waves arising from internal reflection do not instead dominate particle motion. Similarly, the fact that the majority of the acoustic force is directed vertically, rather than the horizontal direction in which sorting takes palce, and the vortices created by acoustic streaming can reduce both device and separation efficiency. Destgeer et. al [203] circumvented the first of these limitations by using a high-frequency device with thin channel walls to reduce energy available for reflection. However, sorting efficiency here was even less impressive, with a 400% difference in particle diameter. For high-sensitivity applications such as the sorting and detection of CTCs, the existing literature on SAW sorting is simply insufficient, a disappointment given the supposed advantages of SAW for microfluidic applications. To address this shortcoming, it is shown to be possible to use SAW for deterministic sorting in Chapter 7, with sorting between particle diameters with less than a 6% difference demonstrated.

Chapter 3

Microfabrication

Microfabrication procedures are integral to the production of both microfluidic channels and the SAW devices that are used to manipulate particles and cells within these channels. In this chapter the steps required are described for the reliable production of micro scale features on both lithium niobate, the piezoelectric material used in part to produce SAW, and in PDMS, the material used to construct the enclosed channels, chambers and other features.

3.1 Overview

Fundamental to the production of microfluidic lab-on-a-chip systems are the microfabrication procedures that make this possible. Here, steps that have been refined and widely used in the microelectronics industry are used to make micron-scale features that, in the case of a saw microfluidic device, are used to both generate a SAW and contain the fluid in which the SAW acts. These features are typically patterned using photolithography, a process that had its beginnings in the printing industry for the reproduction of text and images. To produce micro-scale features for a SAW device UV light is selectively exposed to regions of a thin layer of photoresist, a polymer material that at a molecular scale will either cross-link, creating a more stable structure, or degrade into smaller molecular weight fragments. Developing in an appropriate solvent will remove the more weakly bound regions; by exposing only limited regions of the photoresist patterns can be made almost arbitrarily small, creating down to sub-micron features. Further processes using these features can be used to create electrodes, pattern other materials and fabricate a wide variety of etched structures. The following sections describe the specific procedures required to produce both the SAW device and the microfluidic channels which are bonded to this device.

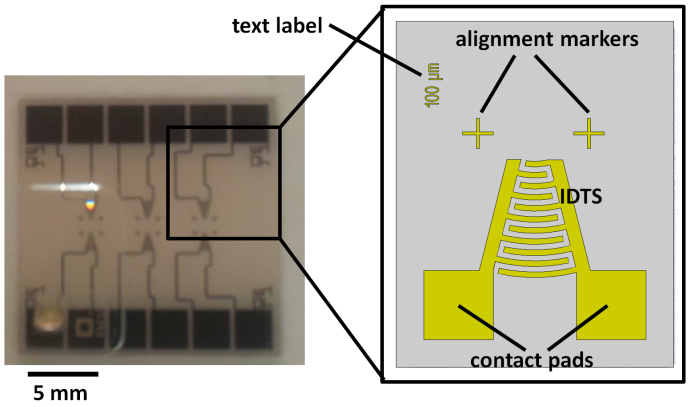

Figure 3.1: A properly implemented and practical SAW device is composed not only of the IDTs that are used to generate a SAW, but also the electrode pads that are used to apply the AC signal, markers for the purpose of aligning PDMS chambers and channels on the device and readable text that describes the device type and/or SAW wavelength (labeled in inset). An example device, comprised of six separate devices, is shown here.

3.2 SAW device fabrication

To create a SAW device, the structures comprising the IDTs, contact pads, text description and alignment markers are patterned on a piezoelectric substrate. These different structures are shown in Fig. 3.1. The material choice for these patterns is limited to ones which are good electrical conductors: Gold (Au) and aluminium (Al) are suitable metals, where a thin metal adhesion layer (5–10 nm) comprised of either chromium (Cr) or titanium (Ti) between the conductor and lithium niobate is used to prevent electrode lift-off. The thickness of the conducting metal layer is dependent on design considerations: a thicker metal layer (up to 1 μm) is more suitable for high-power applications, with lower electrical resistance than a thin metal layer, which will result in a small resonant-frequency shift resulting from metal mass loading.

In the work contained in this thesis, the process begins with a pristine, 0.5 mm thick 128° Y-cut X-propagating lithium niobate wafer, chosen because of the large electromechanical coupling coefficient in this crystal orientation [205]. This wafer is then spin-coated with a layer of photoresist, then heat treated to remove remaining photoresist solvents. To pattern features on this photoresist, a photomask is used to selectively block certain regions of exposure to UV light. These patterns are realized during development, in which regions that have been exposed to light (in the case of a positive resist) or not exposed to light (for a negative resist) are dissolved in an appropriate developer. These developers and suitable UV exposures are listed in Table 3.1.

Metal features can be created created through what is known as the lift-off process. Here, after metals are deposited in a layer of constant thickness across a wafer onto which a photoresist has been patterned, the application of a solvent will dissolve any photoresist on which metals are deposited, thereby 'lifting off' any metals that were not directly deposited on the substrate (see steps 5,6 in Fig. 3.2). The metals deposited using high-vacuum e-beam evaporation where an electron beam is used to heat a sample of metal, which evaporates in a manner analogous to the evaporation of water; when sufficiently heated, individual atoms at the surface gain sufficient energy to overcome bonds within the metal. These atoms radiate in straight paths in all directions until, possible to the large mean free path afforded in a high vaccuum, until they encounter a surface onto which they deposit, including any wafers. By varying both the metal temperature and the exposure time, the thickness of the deposited metal can be defined.

Following metal deposition and lift off, the final step in the process of creating a fully functional SAW device is dicing, where cuts are made along pre-defined lines using a high speed (30,000 rpm), small width ($\sim 30\ \mu$m) cutting tool.

3.3 Chamber fabrication

Chambers are created in a parallel process similar to that used to create the SAW device. Here, photolithography is used to create a mould containing micron-scale features on a silicon wafer. The features that are created on the silicon surface are the inverse of those that end up being patterned in the final chamber, with the patterned wafer serving as a mould on which a liquid PDMS is poured and then cured. There are two distinct pathways to create the patterns of required depth, depending on the photoresist used. If a thick phtoresist such as SU-8 is used, which can be layered in thicknesses of up to 100's of microns, the patterned photoresist is immediately usable as a PDMS mould. However, it may be more desirable to etch directly into the silicon to produce these features, especially if a specific chamber height or a more robust and reusable mould is required. Here, the photoresist pattern is used as a mask for selective deep reactive ion etching (DRIE), where the repeated application of etchant (SF_6) and passivation (C_4F_8) plasma steps results in isotropic, near vertical etching into exposed areas of the silicon substrate [206]. For larger etch depths ($>20\ \mu$m) it may be appropriate to use a metal Cr mask, patterned using the same liftoff process as in Fig. 3.2 as a photoresist mask, which would otherwise eventually be removed in a deep etch. Both of these pathways are shown in Fig. 3.3. The maximum chamber height is limited

Table 3.1: Microfabrication processes

Facility/process	**Materials**	**Function**	**Process variables**
Spin-coater	Delta-80 (SUSS MicroTech, Garching, Germany)	create a thin layer of photoresist on a substrate	3000 rpm for 30 seconds, heat treat at 100° for 90 s
Mask aligner	EVG 6200, photomask (NFC masks, Minneapolis, MN, USA)	align the photomask with the wafer in the correct crystollographic orientation and expose	AZnlof2070: 65-75 mJ/cm^2, AZ 1512: 75 mJ/cm^2, AZ 4562: 150 mJ/cm^2, SU-8 2050: 225 mJ/cm^2
Developer	AZ 400K, AZ 726 MIF (Clariant, Weisbaden, Germany)	remove exposed/unexposed regions of photoresist	AZnlof2070: AZ 726 MIF, AZ 1512: AZ 726 MIF, AZ 4562: AZ 400K
Metal deposition	e-beam evaporator (intlvac nanochrome 1, Niagra Falls, NY, USA)	deposit metals in a thin ($<$1 m) layer to create electrodes or a mask for silicon etching	Pressure $<$7e-6 Torr, Cr: $<$0.6 Å/s @ 3%, Al $<$2 Å/s @ 23%, Au $<$2 Å/s @ 13%
DRIE	PLASMALAB100 ICP380 (Oxford Instruments, Wiesbaden, Germany)	etch vertically into silicon in all regions except those covered by a metal or photoresist mask	Forward power = 20W, ICP power 900W, 8 seconds SF6, 6 seconds C4F8
Lift-off	Acetone, Sonicator (Hilsonic G52, Wirral, UK)	remove any photoresist and metals on top of that photoresist, leaving patterned metals on the substrate	sonication until complete lift-off
Wafer dicer	Dicing saw (Disco DAD321, Tokyo, Japan)	section the wafer into individual SAW devices	cutting speed: 3 mm/s @ 30000 rpm
Bonding	Plasma cleaner (Harrick Plasma PDC-32G-2, Ithaca, NY, USA)	Activate surfaces for bonding	22 s for PDMS, 5 min for LN at 18W and 0.1 mbar

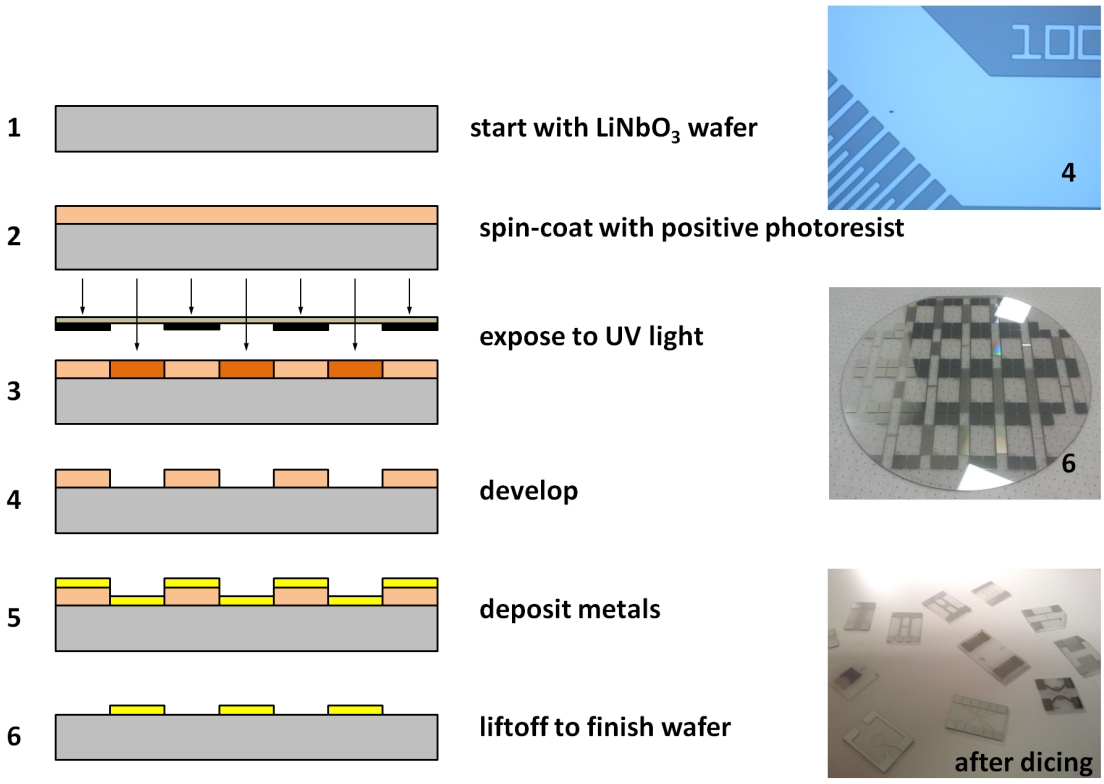

Figure 3.2: Fabrication procedures in the lift-off process to produce patterned metals on a piezoelectric substrate: the SAW device. (1-2) A $LiNbO_3$ wafer spin-coated in photoresist is (3) selectively exposed to UV light @ 387 nm, which after (4) development results in patterned features. Subsequent (5) metal deposition and (6) lift-off results in patterned metals on $LiNbO_3$. Dicing the wafer results in finished devices ready for bonding.

by the size of the features on the PDMS mould. In practice, maximum chamber heights are on the order of ~ 500 μm, a result of the available SU-8 photoresists and, in the case of DRIE, the thickness of typical silicon wafers and the relatively slow etch rate (it would take several hours to etch 500 μm of silicon).

3.4 Device assembly

The SAW device and PDMS chamber are joined through the bonding process to create fully enclosed chambers and channels in which fluid can flow and be acted on by acoustic fields generated by SAW. This process is shown in shown in Fig. 3.4. The fundamental technique underlying this process is the surface activation of both the PDMS and lithium niobate by exposure to an oxygen plasma, resulting in $-$OH surface terminations [207, 208, 209]. Bringing these surfaces into contact with one another results in a chemical reaction, producing H_2O and leaving a single layer of

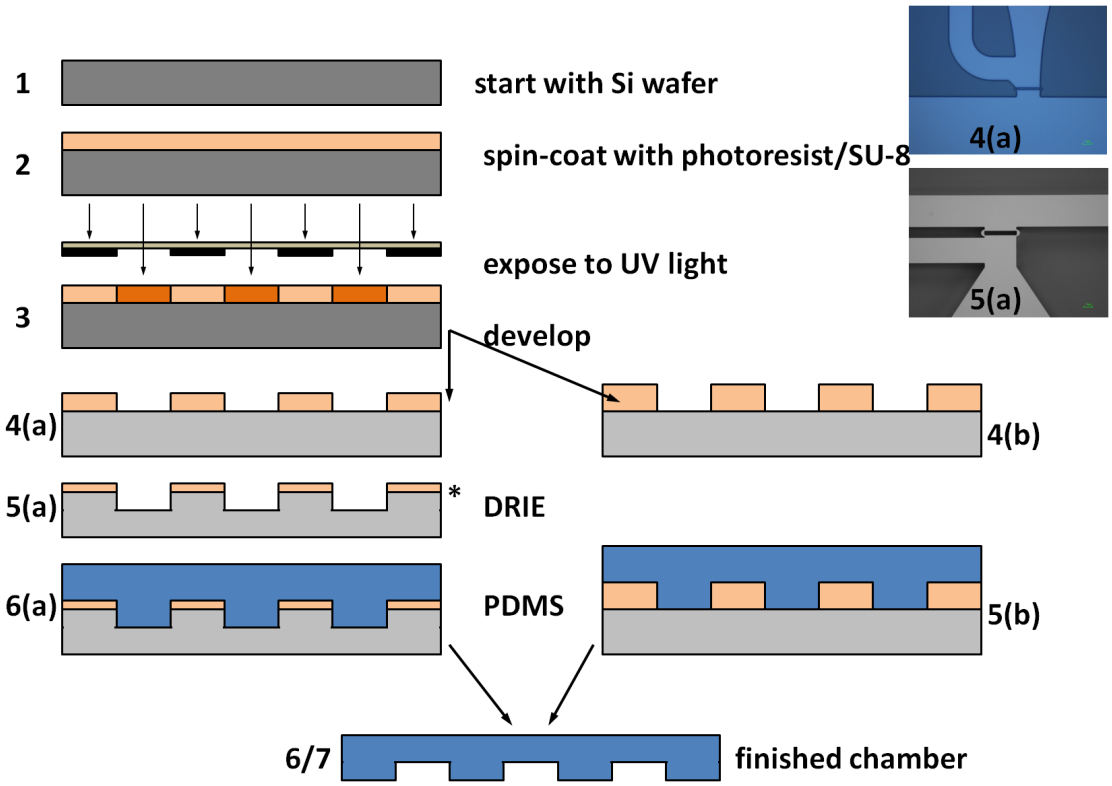

Figure 3.3: Fabrication options to produce a PDMS chamber. (1-2) A silicon wafer spin-coated in photoresist is (3) selectively exposed to UV light @ 387 nm, which after (4a,4b) development results in patterned features. These features, if at the right height, can (5b) be directly used to produce a finished PDMS chamber. Alternatively, the photoresist (or a metal on silicon patterned by lift-off) can (5a) be used as a mask for deep reactive ion etching (DRIE), resulting in a silicon mould for PDMS.

oxygen atoms covalently bonded to each of the two surfaces [210]. The parameters used for this exposure are listed also in Table 3.1.

3.5 Experimental setup

It is important to control the device temperature for the sake of mitigating spurious effects on fluid properties in a microfluidic SAW device, where both density and viscosity of a fluid can change with varying temperature. Additionally, it is especially vital to control fluid temperature when cells or other biological specimens are being analyzed in order to prevent cell death or abnormal cell responses. For these reasons a method to control temperature on the device is required, an excellent candidate being the thermoelectric peltier cooler, a heat pump which can actively cool/heat either side of a series of doped semiconductor junctions with the application of a DC electric potential. To demonstrate the potential for such a system to maintain device temperature as measured at

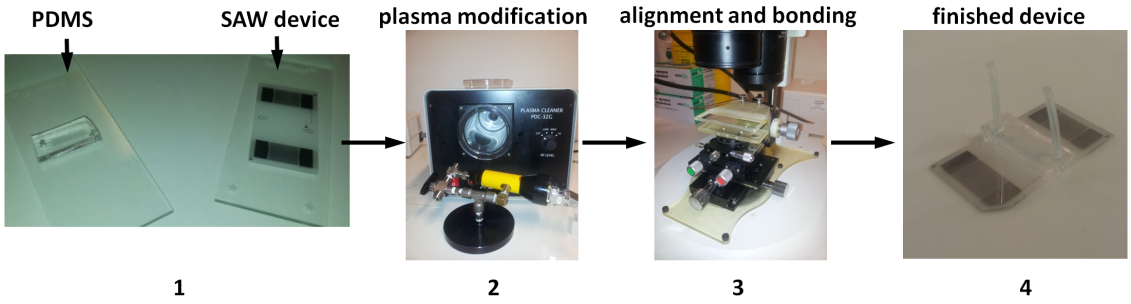

Figure 3.4: A PDMS chamber and SAW device can be bonded together to create fully enclosed fluid chambers in which SAW can be used to manipulate particles and cells. Here, (1) patterned PDMS and a SAW device are (2) exposed to an oxygen plasma. These surface-activated components are then (3) aligned and brought into contact with one another, resulting in (4) a finished device.

the site of a microfluidic channel acted on by SAW, Fig. 3.5 shows the measured SAW device temperature with the application of SAW (on the same device presented later in Chapter 5 using a thermal imaging camera [FLIR i7, Meer, Belgium]) when mounted on a glass slide or peltier cooler. Due to its higher thermal conductivity, even a passively used peltier device will maintain substantially lower temperatures. With sufficient voltage, it is possible to select the steady state temperature at which the device will operate provided a consistent SAW power is used, or at least to limit short term thermal fluctuations.

To drive the SAW devices used in this thesis, a suitable and flexible platform is also required that can accommodate and test a wide range of different SAW devices, which may have different spacings between electrode contact pads, different numbers of IDT pairs and different distances between opposing pairs of IDTs. Further requirements include a stable platform whose dimensions are compatible with operation on a microscope, necessary to visualize micro scale components and to observe device operation, and the integration of the aforementioned active cooling system to maintain stable fluid temperatures to mitigate heat-related effects. In constructing such a platform, these last two requirements have the potential to be especially difficult to reconcile with the limitation in total platform height, where the heated side of a peltier thermoelectric cooler requires heat dissipation and also therefore its own heatsink and air cooling system. With access to a high-quality 3D printer (Objet Eden 260V, Stratasys Ltd, Eden Prairie, MN) it was possible to construct a bespoke platform that integrated these components whilst fitting within the allowable size envelope of ≈ 2 cm. Here, a SAW device rests directly on the thermoelectric cooler, which is

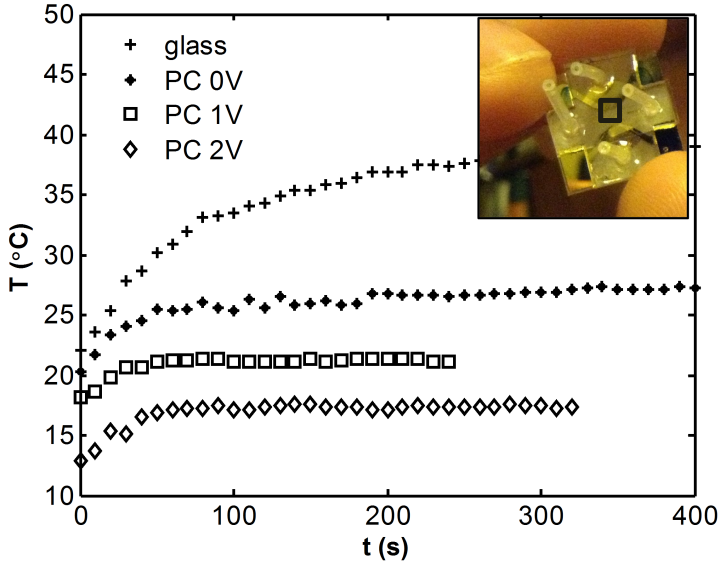

Figure 3.5: A thermally conducting heat pump such as a thermoelectric cooler can be used to choose the steady state device temperature and limit long-term temperature changes. Here, the device is measured at the site of the microfluidic channel subject to SAW (black box in inset) mounted on either a either a thermally non-conductive glass slide or a peltier cooler [PC] (at 0 V, 1 V or 2 V). SAW power is 0.4 W.

itself bonded onto a heat sink with an integrated fan unit. This platform system is shown in Figs. 3.6(a,b).

Additionally, whereas it may have been possible to solder devices individually, this would reduce the ease and rapidity with which devices can be exchanged and would require a separate mechanism to keep the device in contact with the actively cooled platform. With this in mind, spring loaded electrical probes were utilized which serve the simultaneous functions of contacting the electrode pads and holding the device against the platform. Because the 3D printed probe mount is detachable from the platform, these mounts can also be interchanged to suit different electrode pad spacings, yielding a flexible system which is suitable for use with essentially any SAW device, provided an appropriate probe mount is used. Some different probe mounts that can be used in concert with the device platform are shown in Fig. 3.6(a,b).

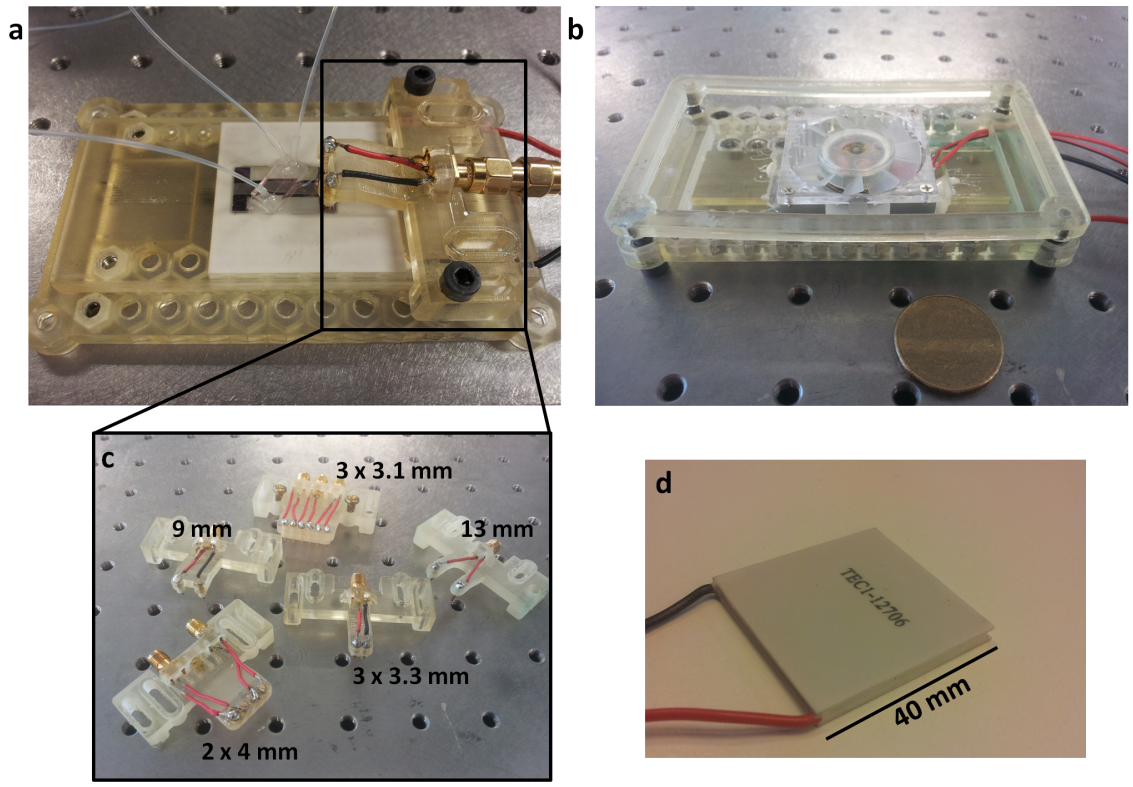

Figure 3.6: (a) The device platform (shown here with representative SAW device) integrates a thermoelectric heat pump that moves heat generated by the SAW device to (b) a combined heat-sink/fan on the underside of the platform. (c) This platform allows for flexible removal of different-sized probe mounts. (d) The thermoelectric device itself is a 40 mm square unit bonded with thermally conductive paste to the heat sink. By applying different electric polarizations the active side can be heated as well as cooled, if this is required.

Chapter 4

SAW atomization droplet size

In Chapter 4 a systematic exploration of the physics the determine droplet size during SAW atomization is performed. SAW atomization is a developing technique for the production of atomized droplets for the purpose of pulmonary therapy, where different droplet sizes can be used to target different lung regions. Previously there was little understanding of either the droplet sizes that are produced during extremely high frequency excitation or the principles and scaling laws that determine what these droplet sizes are. Here, we formulate a theory of the distribution of droplet diameters and test it successfully against experimental results.

4.1 Introduction

In Chapter 2 the concept of atomization was introduced, wherein high-frequency SAW can be used to create an aerosol with application for nebulization therapy. It is known that the lung region targeted by such a therapy is dependent on the droplet size; smaller droplets will progress into deeper lung structures than will larger ones. If then droplet size is known and can be reliably tuned, then the trachea, bronchioles or alveoli can be selected as the site for drug absorbtion, a useful ability in nebulization therapy. For example, in the relief of asthma symptoms it is desirable for a relaxant or steroid to target the upper lung regions [211]. At issue is the control over droplet size that is produced from common nebulization methods, with metered dose inhalers for asthma treatment, for example, producing a wide range of aerosol droplet diameters [212, 213]. In making this diameter range more monodisperse and tunable, more drug can be reliably and efficiently delivered to the required lung regions. To this end, SAW has seen development for use in nebulization therapy, with initial results suggesting that a relatively monodisperse droplet size distribution is produced

[35]. However, if this method is to find widespread use for nebulization therapy with ability to target different lung regions, a thorough physical understanding of the parameters determining droplet size is required. Furthermore, though there are some extant analytical models prescribing the droplet distribution produced during acoustic actuation, there is no reason to believe that these models will necessarily apply to high-frequency SAW, especially if the physical dimensions and mechanisms are different. In order to develop this understanding, an experimental and theoretical analysis of SAW atomization was performed. It was observed in preliminary SAW atomization experiments for this work that droplets arise from a hitherto undescribed thin film, itself produced from high-frequency excitation. Knowing this, a droplet size model was then developed that incorporated a viscous-capillary force balance, which itself is a function of the relative length scales of the thin film, numerically modeled using a lubrication approximation of the Navier Stokes equation. This model was then used to simulate the scaled film length, a function of an acoustic Weber number, and found to match the experimentally measured film length. Because the acoustic Weber number determines film dimensions, which themselves influence droplet size, this model was also used to determine the droplet size scaling, again a good fit for the experimentally measured droplet size. It was found here that, in contrast to models estimating droplet size in bulk-wave acoustic excitation where $D \sim f^{-2/3}$, that $D \sim f^{-1}$.

4.2 Publication

The following publication was reproduced from [34] with permission from The American Physical Society.

Monash University

Declaration for Thesis Chapter 4

Declaration by candidate

In the case of Chapter 4, the nature and extent of my contribution to the work was the following:

Nature of contribution	Extent of contribution (%)
I was chief investigator for this work. I was responsible for device fabrication, the experimental work in the paper, post-processing of experimental and numerical results, with contributions to writing of the paper.	65

The following co-authors contributed to the work. If co-authors are students at Monash University, the extent of their contribution in percentage terms must be stated:

Name	Nature of contribution	Extent of contribution (%) for student co-authors only
Dr. Ofer Manor	Contributions to theory, numerical model development, contributions to writing and overall supervision	
Dr. Andreas Winkler	Preliminary experiments, contributions to concept development, experimental setup and review of drafts	
Dr. Hagen Schmidt	Corresponding author with review of drafts	
Prof. James Friend	Contributions to writing, overall supervision and review of drafts	
Prof. Leslie Yeo	Contributions to theory, writing, overall supervision and review of drafts	

The undersigned hereby certify that the above declaration correctly reflects the nature and extent of the candidate's and co-authors' contributions to this work.

Candidate's Signature	[redacted]	**Date:** 3/15/14
Signature 1	[redacted]	**Date:** 6/5/14
Signature 2	[redacted]	**Date:** 3/21/14
Signature 3	[redacted]	**Date:** 3/19/14
Signature 4	[redacted]	**Date:** 25/3/2014
Signature 5	[redacted]	**Date:** 1/4/2014

Atomization off thin water films generated by high-frequency substrate wave vibrations

David J. Collins,[1,4] Ofer Manor,[2,4] Andreas Winkler,[3] Hagen Schmidt,[3] James R. Friend,[2,4] and Leslie Y. Yeo[2,*]

[1]*Monash University, Clayton, Victoria 3800, Australia*

[2]*Micro/Nanophysics Research Laboratory, RMIT University, Melbourne, Victoria 3000, Australia*

[3]*IFW Dresden, Dresden, Freistaat Sachsen D-01069, Germany*

[4]*The Melbourne Centre for Nanofabrication, Clayton, Victoria 3800, Australia**

(Received 10 September 2012; published 20 November 2012)

Generating aerosol droplets via the atomization of thin aqueous films with high frequency surface acoustic waves (SAWs) offers several advantages over existing nebulization methods, particularly for pulmonary drug delivery, offering droplet sizes in the 1–5-μm range ideal for effective pulmonary therapy. Nevertheless, the physics underlying SAW atomization is not well understood, especially in the context of thin liquid film formation and spreading and how this affects the aerosol production. Here, we demonstrate that the film geometry, governed primarily by the applied power and frequency of the SAW, indeed plays a crucial role in the atomization process and, in particular, the size of the atomized droplets. In contrast to the continuous spreading of low surface energy liquids atop similar platforms, high surface energy liquids such as water, in the present case, are found to undergo transient spreading due to the SAW to form a quasisteady film whose height is determined by self-selection of the energy minimum state associated with the acoustic resonance in the film and whose length arises from a competition between acoustic streaming and capillary effects. This is elucidated from a fundamental model for the thin film spreading behavior under SAW excitation, from which we show good agreement between the experimentally measured and theoretically predicted droplet dimension, both of which consistently indicate a linear relationship between the droplet diameter and the mechanical power coupled into the liquid by the SAW (the latter captured by an acoustic Weber number to the two thirds power, and the reciprocal of the SAW frequency).

DOI: 10.1103/PhysRevE.86.056312 PACS number(s): 47.35.Rs, 47.55.nd, 47.61.−k

I. INTRODUCTION

Surface acoustic waves (SAWs), beyond their versatile potential for rapid and controllable microfluidic actuation [1,2], have the powerful ability for easily atomizing liquids to generate micron dimension aerosol droplets [3–6]—a capability that is important in numerous processes from spray painting, inhalation therapy, and mass spectrometry to inkjet, agricultural, and more recently bioprinting. SAW atomization, in both standing [7] and traveling [8] wave configurations, has considerable advantages over other conventional nebulizers, and, in particular, ultrasonic atomization, in that it uses significantly less power, does not require orifices (e.g., nozzles) or meshes, is suited to producing aerosols within the size range of 1–5 μm for optimal inhalation therapy [9], and can be operated using a simple chip-scale platform comprising a piezoelectric substrate patterned with interdigital transducers (IDT) by means of standard photolithographic techniques [10] or coupled to a superstrate [11,12]. In addition, it has been shown that SAW atomization can be used to rapidly synthesize single and even multilayered composite polymer nanoparticles [13–15] or to rapidly produce polymer array patterns on substrates without necessitating physical or chemical templating [16]. Further, the typically high frequencies and low powers required for atomization do not result in shear- or cavitation-induced molecular damage, especially large biomolecules such as DNA, peptides, or proteins [17], which is particularly crucial for applications in pulmonary drug delivery [9,18] or mass spectrometry [19–21].

Despite the progress in demonstrating the potential of SAW atomization for these applications, there is a remarkable lack of physical and theoretical insight into the mechanisms underpinning atomization and, in particular, the relationship between the SAW frequency and power with the dimension of the resultant atomized droplets; the SAW frequency, in particular, has long been touted as a means for controlling the droplet size, crucial to any aerosolization process. Early attempts to study ultrasonic [22,23] and SAW [13,24] atomization simply proposed correlations between the aerosol dimension and the applied frequency. Subsequent work, in contrast, attempted to unravel the physics governing the atomization process by employing scaling theory to reveal the dominant role of capillary and viscous stresses in the destabilization of the air-liquid interface leading towards its breakup to form atomized droplets, and provided experimental measurements of the free surface vibration to dispel the prevailing view that the SAW frequency plays a dominant role in governing the atomized droplet dimension; instead, these studies hinted at the influence of the geometry of the source liquid (either a sessile drop or a thin film) spreading atop the atomization platform under SAW excitation, from which the atomized drops are ejected [5,25]. It was suggested that thin film geometries led to smaller droplets and higher atomization rates compared with that obtained using sessile drops as the source liquid geometry [5,17], although this was based on scaling arguments and preliminary experimental observations.

Here, we study the mechanism by which various system parameters (in particular, the applied frequency and power) govern the spreading of SAW-induced thin liquid films atop atomization platforms [17], and how the characteristics of the thin film, as a consequence, influence the size of the

*[redacted]

atomized droplets. Water films are assumed here, not merely for simplicity, but because water is a common drug excipient and carrier for biological agents in aerosol applications. In particular, we elucidate the specific mechanism controlling the thickness of the spreading film, highlighting the behavior of these high surface energy water films in distinct contrast to the behavior of low surface energy silicone oil films [26]: the discrepancy between the continuous spreading of silicone oil films and the transient spreading of water films leading to their quasisteady behavior is directly related to the characteristic difference observed in the resultant film heights.

The rest of the paper is organized as follows. In Sec. II, we briefly discuss the current physical understanding of the mechanics underpinning SAW atomization. This is followed by a description of the experimental procedure carried out to investigate SAW atomization in Sec. III. We then formulate a theory to model the spreading of the water film in Sec. IV, from which we obtain predictions for the quasisteady film shape. These predictions then facilitate a comparison with the experimental data in Sec. V. Finally, we summarize our findings in Sec. VI.

II. SAW ATOMIZATION

Unlike *bulk* ultrasonic transducers, the SAW energy is isolated along the *surface* of the piezoelectric substrate that constitutes the atomization platform, exponentially decaying within a few wavelengths into the substrate depth. When the SAW comes into contact with the leading edge of the liquid, however, it is diffracted into the liquid phase at the *Rayleigh angle* $\theta_R = \sin(c_l/c_s)$ subtended to the vertical axis, where c_l is the sound velocity in the liquid and c_s is the SAW velocity on the substrate [2,27]. The SAW thus comprises an efficient energy transfer mechanism from the solid substrate to the liquid, and generates sound waves in the liquid that give rise to an acoustic radiation pressure [28] as well as a streaming flow that is a consequence of a collection of mechanisms [1], including Eckart streaming [29,30] and Schlichting streaming [31,32]. The acoustic radiation pressure is a consequence of the steady, time-averaged stress imparted on the drop-film interface due to the mismatch in the acoustic impedance across the interface upon the impact and subsequent reflection of the sound waves. Eckart flow is a steady vortical flow in the liquid bulk arising from the energy dissipated during viscous attenuation of axially polarized sound waves over length scales much larger than the sound wavelength in the liquid, whereas Schlichting streaming describes flow within a submicron-thick viscous boundary layer immediately adjacent to the substrate surface along which the SAW traverses [32]. Despite its confinement, the latter is, nevertheless, not only capable of altering the contact angle between the liquid body and solid substrate, but also displacing the three-phase contact line [33,34]. As such, the acoustic radiation pressure and both the Eckart and Schlichting streaming mechanisms are likely to govern the geometry and wetting properties of the parent liquid on the atomizing platform.

The influence of these properties on the atomization process, in particular, and hence on the size and production rate of the aerosol droplets has been previously implied [5]. Atomization ensues above a threshold power [5,35] beyond which capillary forces are no longer able to stabilize the interface from perturbations imposed by the substrate acceleration and the consequent streaming in the parent liquid. The dimension of the ejected droplets D, formed during the pinch-off and breakup of the destabilized wave crests, then corresponds to the most dangerous wavelength associated with the instability, which can be estimated from a dominant capillary-viscous stress balance [5]

$$D \sim \lambda \sim \frac{\gamma H^2}{\mu f L^2}. \tag{1}$$

γ is the gas-liquid surface tension, μ the liquid shear viscosity, and f the SAW frequency, whereas H and L are the characteristic height and length scales of the parent liquid film or drop, respectively. We shall show later that the shape of the parent liquid film or drop (i.e., H and L) is dependent on the SAW frequency and amplitude. Of particular note in Eq. (1) is the $D \sim 1/f$ relationship, distinct from the $1/f^{2/3}$ scaling in correlations based on the subharmonic capillary wave excitation that have previously been reported, originally for ultrasonic transducers [22], but often prescribed wholesale for SAW atomization with little regard for the markedly different physics between the systems [24]. It is also questionable whether the small amplitude perturbation assumption implicit in the derivation of these linearized models holds, especially when the breakup of the interface to produce aerosol droplets during the atomization process is typically associated with large amplitude interfacial deformation. Below, we provide empirical evidence to support this inverse frequency scaling, *as yet unverified*. In addition, we note the influence of the aspect ratio H/L (i.e., the geometry of the parent liquid drop or film) on the ejected droplet size in Eq. (1): $H/L \sim 1$ for a sessile drop whereas $H \ll L$ for a thin film. We show that H is related to the wavelength of the sound waves generated in the liquid due to the leaky SAW, and develop a numerical simulation for the spreading of the quasisteady film to predict L as a function of the various system parameters; in particular, L is found to evolve with the mechanical power emitted by the SAW that is then transferred to the liquid. These H and L values are then used in Eq. (1) to predict the droplet sizes, which compares favorably with the trends observed in the experimental data acquired over the range of applied frequencies tested (13–124 MHz).

III. EXPERIMENT

We employed 13–132 MHz Rayleigh SAW devices comprising 7-nm chrome/175-nm gold interdigital transducers (IDTs) patterned using standard photolithography on a 0.5-mm thick 128° Y-cut, X-propagating single crystal lithium niobate (LN) piezoelectric substrate [10], as depicted in Fig. 1. We examined the following frequencies: 13.2, 18.9, 22.0, 26.4, 33.0, 44.0, 66.1, 99.1, 123.9, and 132.1 MHz using IDTs with 25, 33, 33, 33, 31, 29, 25, 20, 50, and 20 finger pairs, respectively. The SAW was generated by applying a sinusoidal electric voltage to the IDT using a signal generator (SML01; Rohde & Schwarz, North Ryde, NSW, Australia) and amplifier (10W1000C; Amplifier Research, Souderton, PA). The voltage across the SAW device, measured using an oscilloscope (Wavejet 332/334; LeCroy, Chestnut Ridge,

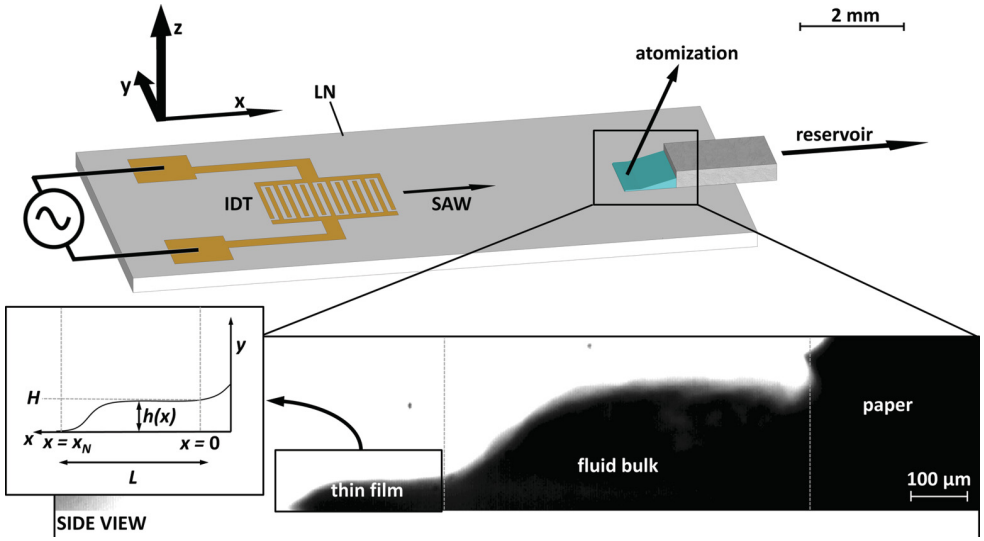

FIG. 1. (Color online) Schematic illustration of the SAW atomization device comprising a lithium niobate (LN) substrate on which interdigital transducer (IDT) electrodes were patterned. The liquid to be atomized was supplied from a reservoir (not shown) through a paper wick. As illustrated by the expanded-view image, the SAW drew out a meniscus from the paper, comprising a thin advancing film and a bulk region, both of which are characterized by different length scales, capillary frequencies, and resultant droplet sizes. The majority of the atomized droplets, however, originated from the thin film region with characteristic height and length scales denoted by H and L, respectively, both of which are small compared to the width of the film, which, in turn, is set by the width of the paper wick.

NY), then determines the SAW surface-normal displacement velocity, subsequently measured using a laser Doppler vibrometer (LDV, UHF–120; Polytec GmBH, Waldbronn, Germany); this was also used to verify the existence of a traveling SAW. Under SAW excitation, the liquid to be atomized (deionized water; Milli-Q 18.2 MΩ.cm, Millipore, Billerica, MA), initially housed in an external reservoir, was delivered to the SAW device for atomization using a capillary wick consisting of polyester-cellulose clean room paper (C1; LymTech, Chicopee, MA) with a width similar to that of the IDT aperture, and that was placed in contact with the edge of the device [17], as illustrated in Fig. 1. The SAW device itself was placed on a Peltier cooler (CP85438; CUI Inc., Tualatin, OR) to mitigate spurious effects from evaporation, a step not previously taken in other SAW atomization experiments. The film spreading dynamics were observed using a high-speed camera (iSpeed, Olympus, Yokohama, Japan) at 1500–10 000 fps, whereas droplet sizes were measured via laser diffraction (Spraytec, Malvern Instruments, Malvern, UK); three separate measurements over a 15 s duration were taken for each SAW frequency.

Contact between the edge of the wetted paper wick and the hydrophilic LN substrate surface led to the formation of a meniscus between the two substrates, as sketched in Fig. 2(a). Under the influence of SAW beyond a sufficient power level, the meniscus was observed to spread in a direction opposite to that of the SAW propagation, forming a liquid bulk with characteristic height and length scales that are several times the sound wavelength in water λ_l [Fig. 2(b)]. The pullout of water from the wetted paper is known to result from the interaction between the flow in a thin viscous boundary layer that forms in the meniscus immediately above the LN substrate and the free air-water interface [26,32,34]. Further spreading of the water body atop the LN substrate then results in two characteristic fluctuating regions [Fig. 2(c)]: a bulk region adjacent to the paper that retains a similar characteristic length and thickness as before, and a thin front-running film region with a characteristic length roughly corresponding to two SAW wavelengths (i.e., $L \equiv 2\lambda_{\mathrm{SAW}}$) and a thickness that appears to scale with λ_l. Next, we discuss the mechanism and parameters that govern the characteristic height H and length L of this thin front-running film region, whose interface subsequently breaks up to produce the atomized droplets [Fig. 2(d)].

IV. THEORY

A. Film height

We treat the interaction between the SAW-induced sound wave in the liquid, emitted from the LN surface ($y = 0$) at an angle $\theta_R \approx 22^\circ$ to the vertical y axis (see Fig. 1), and the free air-water interface ($y = h$) as a simplified model in which the sound wave is emitted from a simple piston, offset from the horizontal axis $y = 0$ by θ_R towards a horizontal fully reflecting surface at $y = h$. To leading order in θ_R, the piston can be assumed horizontal ($y = 0$), emitting sound waves along the vertical y axis with a wavelength equal to the vertical component of the original sound wavelength $\lambda_v = \lambda_l \cos\theta_R$. Under these conditions, the time-averaged energy density in the liquid between the piston and the free surface of the film follows [28]

$$\langle E\rangle \approx \frac{\rho\xi_0^2\omega^2(\beta+1)}{4\beta\cos^2(2\pi h/\lambda_v)\sin^2(2\pi h/\lambda_v)}, \qquad (2)$$

where ρ, ξ_0 and $\omega = 2\pi f$ are the liquid density, SAW vertical displacement amplitude, and SAW angular frequency, respectively, as seen in Fig. 3(a). The heights $h/\lambda_v = n/4$ ($n = 1,2,3,\ldots$) correspond to acoustic resonance modes with

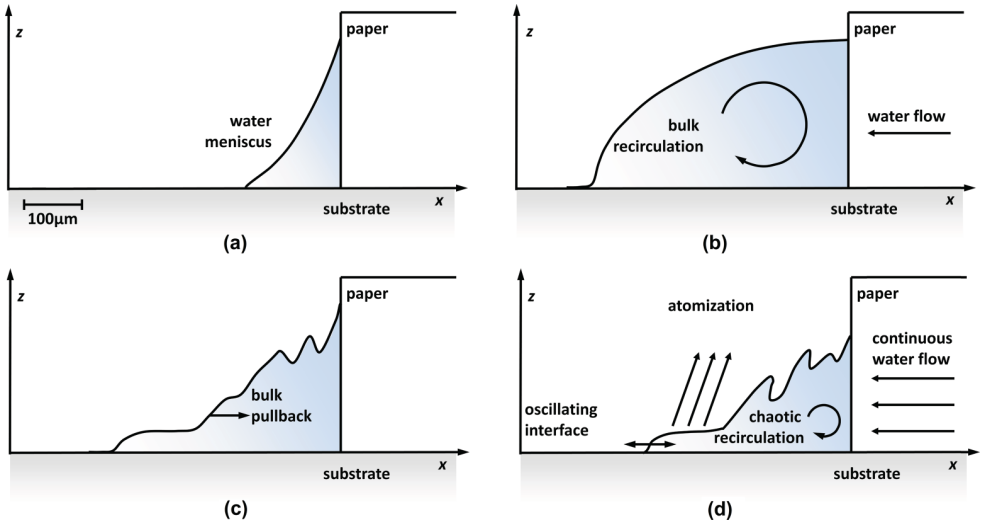

FIG. 2. (Color online) (a) At rest and prior to SAW actuation, a liquid meniscus formed between the wetted paper and the LN substrate. (b) Application of the SAW results in the pullout of a liquid bulk with height and length scales several times the liquid wavelength λ_l. (c) After ~50–500 ms, the leading edge of the liquid bulk was observed to retreat, (d) leaving behind a thin film region from which atomization occurred. The film and chaotic bulk liquid regions interacted dynamically, with the film moving horizontally and occasionally being obscured completely by the bulk region.

an unbounded acoustic energy density in the film, delivering an unbounded radiation pressure intensity at and normal to the planar liquid free surface and rendering an inevitable change in the film inclination or thickness until the acoustic resonance is suppressed. On the other hand, $h/\lambda_v = n/8$ ($n = 1,3,5,\ldots$) is associated with the local minima in the acoustic energy density, a balance between this in the form of the corresponding local minima in radiation pressure intensity with the capillary stress then leads to stable film heights. Depending on the initial height of the film, or the height of the region from which the thin film is pulled out [for example, the bulk region to the right of $h\,(x = 0)$ in the inset of Fig. 1], the film then assumes an equilibrium height at the next energy minima [Fig. 3(b)]. In this case, the thin advancing film at the far left of Fig. 3(c) is observed to obey $h \approx 7/8\lambda_v$ at different applied frequencies and power levels. In fact, we observe, quite uniquely for thin liquid films, the entire film and bulk region in its transient state to occasionally exhibit traits of such energy minimization, apparent in the stable *stair-stepping* of the film height at multiple odd integers of one-eighth wavelengths seen in Fig. 3(c). In an earlier study [26], silicone oil films drawn out from a similar platform by SAWs were observed to follow $h \approx 3/8\lambda_v$ [see the lone experimental point denoted by the square in Fig. 3(b)]. The reason for the difference in the characteristic film height between water and silicone oil is as yet unclear, although the key difference between water and silicone oil is in the surface tension, roughly 72 mN/m for water and 20–30 mN/m for silicone oil, which renders a different initial three phase contact angle formed between each liquid and the solid substrate (roughly 10–20° for silicon oil and 60–70° for water at rest). In any case, having found a relationship that estimates the characteristic film height $H \approx 7/8\lambda_v$ to be used subsequently in Eq. (1), we now turn to formulate a model that describes the mechanism governing the film length l.

B. Film length

The thin film geometry in the inset of Fig. 1 is governed by an interplay between capillary and acoustic effects; the latter is excited by SAWs that propagate at the substrate surface in the direction opposite to that of the film spreading [26], and comprise compressional motion in the liquid film that, to first approximation, can be modeled as the horizontal and vertical particle displacement of a sound wave in an unbounded fluid [36]

$$\begin{aligned} s_x &= \xi_0 e^{j\omega t} e^{-jk_L x} e^{-\alpha k_L z}, \\ s_z &= -j\alpha\xi_0 e^{j\omega t} e^{-jk_L x} e^{-\alpha k_L z}, \end{aligned} \tag{3}$$

respectively. Here, the attenuation of the sound wave is neglected since the characteristic sound attenuation length scale $4\rho c_l^3/3\omega^2\mu \approx 0.1$–$0.01$ m [37] is large compared to the thickness of the thin film for the range of frequencies investigated. In the above, x and z are the horizontal and vertical coordinates in the film, respectively, originating at the liquid-solid interface and the neck bordering the thin film and the water bulk shown in Fig. 1, t is time, and, $k_L = k_r + jk_i$ is the SAW wave number, taken to be a constant with the complex component $k_i^{-1} \approx \rho_s c_s \lambda_{SAW}/\rho c_l \approx 9\lambda_{SAW}$ representing the SAW characteristic attenuation length under an unbounded fluid [38] and $\alpha = [1 - (c_s/c_l)^2]^{-1/2}$; ρ_s is the substrate density. The nonisotropic Rayleigh acoustic radiation pressure on the free surface of the film may then be described by [34]

$$\mathbf{p_r} = \left\langle \frac{\mathbf{vv}}{2\,|\mathbf{v}|^2} + \mathbf{I}\frac{B}{4A} \right\rangle \rho\,|\mathbf{v}|^2\,, \tag{4}$$

where $|\mathbf{v}| = |\partial \mathbf{s}_x/\partial t, \partial \mathbf{s}_z/\partial t| \approx \xi_0\omega$ is the magnitude of the harmonic sound particle velocity, $\mathbf{I}$ is the identity tensor, and A and B are Fox and Wallace coefficients [39], respectively; the angled parentheses denote the time averaging of the inner quantity [i.e., $\langle\zeta\rangle \equiv (1/2\pi)\int_0^{2\pi} \zeta\, dt$].

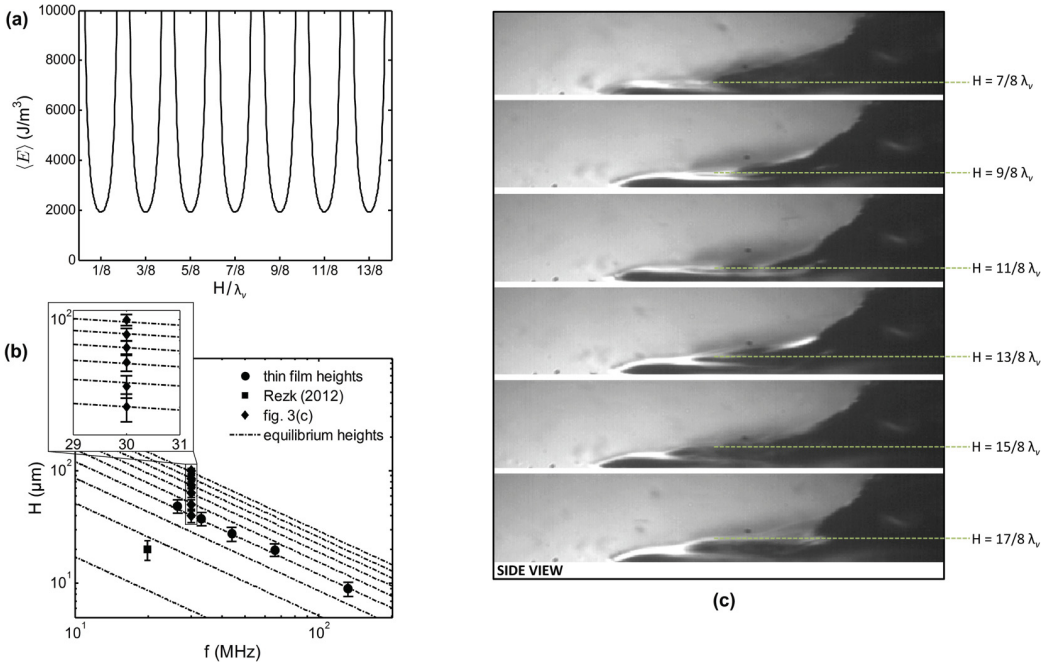

FIG. 3. (Color online) (a) Acoustic energy density, wherein local energy minima occur at odd one-eight integers of the vertical component of the sound wavelength $\lambda_v = \lambda_l \cos\theta_R$, calculated here for $\omega/2\pi = 33$ MHz and $\xi_0 = 7.3$ nm. This corresponds to an acoustic Weber number $\mathrm{We} \equiv \rho(\xi_0\omega)^2 L/\epsilon\gamma$, a measure of the power applied to the film, of 7.7; $\xi_0\omega$ is the characteristic velocity of the elements in the fluid as the sound wave traverses and L is twice the SAW wavelength. (b) The circle data points represent equilibrium film heights H (Fig. 1) and are observed to correspond to the local energy minima, or more specifically, seven-eighths times the vertical component of the wavelength $\lambda_v = \cos(\theta_R)\lambda_l$. The SAW frequencies associated with the experimental points from left to right are 26.5, 33.0, 44.0, 66.1, and 132.1 MHz, and the corresponding range in We numbers, which do not appear to significantly contribute to the thin film height, are (4.2–13.1), (3.7–14.8), (5.5–9.1), (2.4–6.8), and (1.1–2.4), respectively. The square data point at 20 MHz is taken from an earlier study [26] where silicone oil in place of water was used and the diamond data points (magnified in the figure inset) represent the equilibrium and additional transient film heights between $7/8\lambda_v$ and $17/8\lambda_v$, observed with a 30 MHz device. (c) Upon initial application of the SAW, a transient state can develop in which the water meniscus exhibits different stable heights that correspond to odd one-eighth multiple integers in addition to the $7/8\lambda_v$ equilibrium height. This image was taken of a liquid meniscus in the same setup as that described in Fig. 1 when subject to a 30 MHz signal, modulated here with a 300 Hz sinusoidal amplitude signal to prolong the transient stage of the thin film formation, thus enabling us to capture it.

Over short $\mathcal{O}(\omega^{-1})$ time scales, mass and momentum transfer are governed by Eq. (3). Over long times, mass and momentum transfer commensurate with the hydrodynamic time scales are governed by the second-order steady component of the flow field, generated by the $\mathcal{O}(|\mathbf{v}|)$ SAW and the corresponding sound particle velocity in Eq. (3). After expanding the continuity and Navier-Stokes equations in a small parameter defined by the Mach number $\mathrm{Ma} = |\mathbf{v}|/c_l$ and subsequent time averaging, these satisfy [29,40]

$$\nabla \cdot \mathbf{u} = 0, \tag{5}$$

$$-\nabla p + \mu\nabla^2\mathbf{u} + \mathbf{F} = 0, \tag{6}$$

to $\mathcal{O}(v_0\mathrm{Ma})$. Here, $\mathbf{u}$ and p are the steady components of the second-order velocity and hydrodynamic pressure fields in the film and $\mathbf{F} = -\langle\rho(\mathbf{v}\cdot\nabla)\mathbf{v} + \mathbf{v}(\nabla\cdot\rho\mathbf{v})\rangle$ is an effective body force over long times that originates from the divergence of the Reynolds stress tensor $\rho\mathbf{vv}$. The appropriate boundary conditions are then prescribed by the no-slip condition at the solid substrate

$$\mathbf{u}|_{z=0} = 0, \tag{7}$$

the normal stress jump at the free surface $z = h$

$$-(p\mathbf{I} + \mathbf{p_r})\cdot\mathbf{n} + \mu(\nabla\mathbf{u} + \nabla\mathbf{u}^T)\cdot\mathbf{n} = \gamma\nabla\cdot\mathbf{nn}, \tag{8}$$

where $\mathbf{n}$ is the outer unit normal to the air-water interface, and mass conservation in the film

$$\frac{\partial h}{\partial t} = -\frac{\partial(\overline{u}_x h)}{\partial x}. \tag{9}$$

We now expand the equations and boundary conditions that govern the nonvanishing (over long times) flow component [i.e., Eqs. (5)–(8)] in the small parameter $\epsilon \equiv H/L$ and ignore the next order correction in Ma, justified by the difference in magnitudes between $\epsilon \approx 10^{-1}$ and $\mathrm{Ma} \approx 10^{-3}$; given that H and L are small compared to the width of the film, which, in turn, is determined by the width of the paper wick, it is not unreasonable to assume a two-dimensional model. The problem is then rendered dimensionless using the following set of transformations:

$$\begin{aligned}&\left(x, k_L^{-1}\right) \to \left(x, k_L^{-1}\right) L, \quad (z,h) \to (z,h)\, H, p \to (\epsilon\gamma/L)\, p,\\ &(u_x, u_z) \to \left(\epsilon^3\gamma/\mu\right)(u_x, \epsilon u_z),\end{aligned} \tag{10}$$

in which the scaling for the velocity and force in the film are chosen to satisfy the balance between acoustic streaming and

capillary effects. Omitting $O(\epsilon)$ and smaller contributions, the integral mass and momentum conservation equations in the quasisteady film are then given by [41]

$$\frac{\partial}{\partial x}\int_0^h u_x\, dy = 0, \tag{11}$$

$$\frac{\partial^2 u_x}{\partial z^2} = \frac{\partial p}{\partial x} - F_x. \tag{12}$$

Due to the small attenuation of the SAW and thus the sound wave in Eq. (3) (i.e., $k_i \ll 1$) the horizontal component of the body force when in contact with the thin film may be expressed as [36]

$$F_x = -\mathrm{We}\left(1+\alpha_1^2\right)k_i, \tag{13}$$

where $\mathrm{We} \equiv \rho(\xi_0\omega)^2 L/\epsilon\gamma$ is an *acoustic* Weber number that captures the relative contributions from the inertial forcing and the stabilizing capillary stresses. In addition, the absence of any externally applied pressure gradients

$$\frac{\partial p}{\partial z} = 0, \tag{14}$$

together with Eq. (8) then renders the scaled hydrodynamic pressure

$$p \approx -\frac{\partial^2 h}{\partial x^2}. \tag{15}$$

Finally, the boundary conditions on the solid substrate and at the free surface are

$$u_x|_{z=0} = 0, \qquad \frac{\partial u_x}{\partial z}|_{z=h} = 0. \tag{16}$$

Equations (8), (11), (12), and (16) then give rise to the quasisteady thin film equation

$$\frac{\partial}{\partial x}\left[h^3\left(\frac{\partial p}{\partial x} - F_x\right)\right] = 0, \tag{17}$$

where, owing to the weak attenuation of the SAW along the thin front-running film region (see Fig. 1), the contribution of the radiation pressure p_r to the hydrodynamic pressure p, mediated by Eq. (14), is roughly uniform, therefore eliminating any net contribution of p_r to the film shape in Eq. (17). The boundary conditions at the interface in the neck between the thin film and bulk regions (Fig. 1) can then be specified by

$$h|_{x=0} = 1, \qquad \left.\frac{dh}{dx}\right|_{x=0} = 0. \tag{18}$$

Given the highly smooth, chemically homogeneous, and hydrophilic nature of the LN substrate, and following [34], we postulate that the three-phase contact angle at the advancing front of the thin film at $x = x_N$ vanishes under the high applied powers required for SAW atomization. The mechanism responsible for the vanishing contact angle arises from the interaction between the dominant Schlichting flow [32] and the free surface in a viscous boundary layer immediately above the substrate possessing a characteristic thickness $\delta \equiv (\mu/\rho\omega)^{1/2}$, where the contributions from the bulk flow considered earlier are small. It can then be assumed that the vanishing contact angle gives rise to the existence of a thin front-running precursor film with a thickness that scales as δ, irrespective of the bulk flow, such that the following boundary conditions can be imposed:

$$h|_{x\to\infty} \approx \delta/H, \qquad \left.\frac{dh}{dx}\right|_{x\to\infty} = 0. \tag{19}$$

Equations (17) to (19) were solved numerically using the MATLAB boundary value problem solver bvp4c [42]. Rather than using a coordinate transformation to handle the infinite domain, the computational spatial domain was limited to a maximum length of 20 units to reasonable accuracy, allowing for a numerical error below 0.1% on a mesh of 10 000 points. The calculated geometry was further found to be insensitive to arbitrary values of the precursor film thickness, spanning $[0.1\delta/H, 10\delta/H]$.

V. RESULTS AND DISCUSSION

Equation (17) presents the competing mechanisms that govern the thin film geometry, whereby the capillary pressure within the film, mediated by the hydrodynamic pressure p, minimizes the deformation of the free surface; in the absence of SAW, the acoustic stresses embodied by the volume force F_x are absent and the meniscus then spreads to form a film that completely covers the solid substrate under the fully wetting condition of Eq. (18). Under the influence of external acoustic stresses, however, the body force F_x drives an opposing flux of liquid volume in the SAW propagation direction from the thin film *back* towards the water reservoir. Ignoring rapid fluctuations that occur on the free surface of the film, this competition between the capillary and acoustic volume force then leads to a quasisteady film shape over long times that satisfies global volume conservation (i.e., no net volume flux across the film cross section). Figure 4 shows the effect of We on the quasisteady film shape: increasing We, equivalent to higher applied powers and hence surface displacement velocities, leads to an increase in the acoustic body force F_x, that, in turn, generates a larger volume flux from the film towards the reservoir, resulting in a shorter film length. The numerical solution decays with an increase in We and appears to agree well with experimental measurements of the maximum length of the thin film region observed, defined as the distance from the end of the bulk region [i.e., $x = 0$ (taken to be at the intersection between the height of the uniform thin film region $y = H$ with the tangent of the curved free surface just outside the film in the bulk region)], to the location of the apparent contact line at $x = x_N$, as sketched in the inset of Fig. 1; $x = x_N$ is determined at the limit of visual detection where the film height corresponds to one pixel in the experimental digital image.

To further quantify the decay in the film length with We, we introduce the functional form of the normal stress at the free surface and acoustic body force in the film, and omit the noncontributing radiation pressure term. The Weber number We may then be eliminated from the film equation [Eq. (17)] by rescaling the spatial coordinate as $x \to xL\mathrm{We}^{-1/3}$ in place of the preceding scaling to give the generalized film equation

$$\frac{\partial}{\partial x}\left\{h^3\left[\frac{\partial^3 h}{\partial x^3} - \left(1+\alpha_1^2\right)k_i\right]\right\} = 0. \tag{20}$$

Equation (20) underscores the balance between the competing capillary and acoustic body forces, rendering the film length

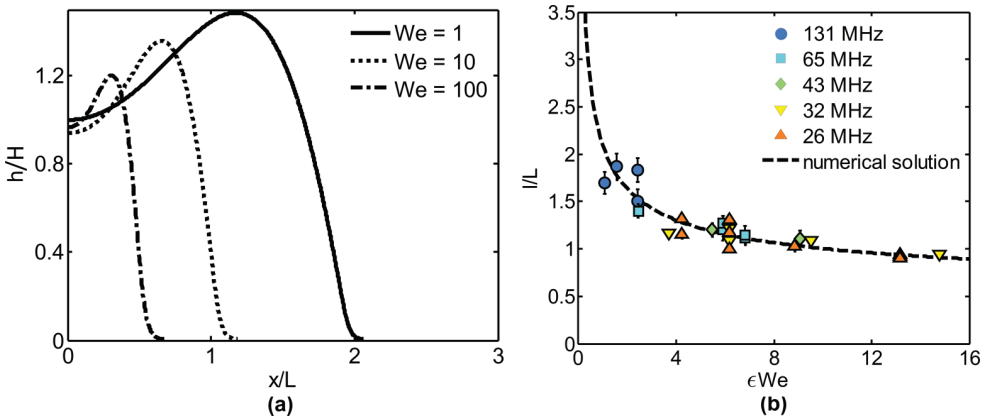

FIG. 4. (Color online) (a) Quasisteady film shape for different acoustic Weber numbers $\mathrm{We} = \rho(\xi_0\omega)^2 L/\epsilon\gamma$. Higher powers (and hence surface displacement velocities) and larger SAW wavelengths are observed to give rise to shorter films. (b) Single measurements of scaled maximum observed film lengths l/L for different applied frequencies (26–131 MHz) and powers (2.6–10.2 W), with resulting We values showing good agreement with the numerical result predicted by the solution of Eq. (17). It can be seen that both the experimentally measured and numerically predicted film lengths progress to an asymptote beyond $\epsilon\mathrm{We} \gtrsim 4$. The error bars indicate the measurement error related to the pixelation of the original digital imagery.

to decay as $\mathrm{We}^{-1/3}$ and generalizing the result shown in Fig. 4(b).

Although a thin film was clearly observed, the *onset* of atomization only occurred above a critical $\epsilon\mathrm{We} \approx 1$. Above $\epsilon\mathrm{We} \gtrsim 4$, however, we observe the film length l to be insensitive to We. Given that H is fixed for a given applied frequency (Sec. IV A), it then follows from Eq. (1) that the ejected droplet dimension scales with the inverse of the applied frequency, which was first suggested in [5] but without experimental corroboration. This $1/f$ relationship for the droplet dimension, distinct from the $1/f^{2/3}$ scaling previously suggested [22–24], is therefore experimentally verified for the first time here in Fig. 5(b) in which the droplet sizes are the mass median diameters obtained from the size distribution of the ejected droplets [an example of which is shown in Fig. 5(a) for an applied frequency of 22 MHz]. The trimodal distribution in Fig. 5(a) is typical of that observed across the range of frequencies employed: The small and intermediate droplet sizes, with peaks close to mass median diameters of approximately 1 (peak 1) and 15 μm (peak 2), originated from droplets that were observed to be ejected from the thin film region (Fig. 1), whereas the largest droplets corresponding to the last peak at the extreme right with dimensions on the order of 100 μm were observed to be ejected from the bulk region (Fig. 1). These large droplets can be excluded from the following discussion as the model in the current study pertains solely to the dynamics of the thin film region.

In particular, we recall from Sec. IV A that the film height, in dimensional terms, can be approximated by $h \sim H \approx 7/8\lambda_v$, implying that $h \sim H \sim 1/f$. Since $L \equiv 2\lambda_{\mathrm{SAW}} \sim 1/f$ and thus $l \sim L\mathrm{We}^{-1/3} \sim \mathrm{We}^{-1/3}/f$, it then follows that both h and l scale inversely with f, and consequently the film aspect ratio $h/l \sim H/\left(L\mathrm{We}^{-1/3}\right)$ is independent of f and is instead dependent on We, or, more specifically, the mechanical power transmitted by the SAW into the liquid, manifested by the term $\rho\xi_0^2\omega^2$ in the definition of We. Correcting for the actual film aspect ratio h/l in place of the characteristic power independent height to length scale ratio H/L in Eq. (1) then leads to

$$D \sim \frac{\gamma H^2}{\mu L^2}\frac{\mathrm{We}^{2/3}}{f}, \tag{21}$$

suggesting that the ejected droplet sizes scale linearly with $\mathrm{We}^{2/3} f^{-1}$, consistent with that observed in Fig. 5(b).

VI. CONCLUSION

SAW atomization comprises a powerful means for the generation of micron dimension aerosol droplets from a miniature microfluidic platform for various applications across spray painting, mass spectrometry, and drug delivery. The key advantages of the platform are its low power, miniaturizability into a small handheld portable platform, and, due to the high frequencies employed, the absence of shear or cavitation damage to biomolecules—an important criterion if the device is to be used for pulmonary delivery of next generation therapeutics such as peptides, proteins, and nucleic acids. Nevertheless, little is understood about the physics associated with SAW atomization systems; in the absence of work to revisit the fundamentals, there has been a tendency to inappropriately adopt theories developed for bulk ultrasonic atomization, rather inappropriate due to the substantial differences in the nature and mechanics of the acoustic excitation between the two methods of atomization.

Here, we examined the mechanisms that underpin the hydrodynamics associated with SAW atomization of droplets from a thin liquid film source, with the intent of providing a more rigorous verification of the role of the parent liquid source geometry and hence the inverse frequency scaling of the atomized droplet dimension alluded to in a previous study [5]. The size of water droplets produced from the atomization of a spreading meniscus drawn out by the SAW from a wet permeable paper strip connected to a reservoir was measured using laser diffraction. These appear to have different sizes depending on the region along the elongated meniscus film they are atomized from. Larger 100 μm droplets

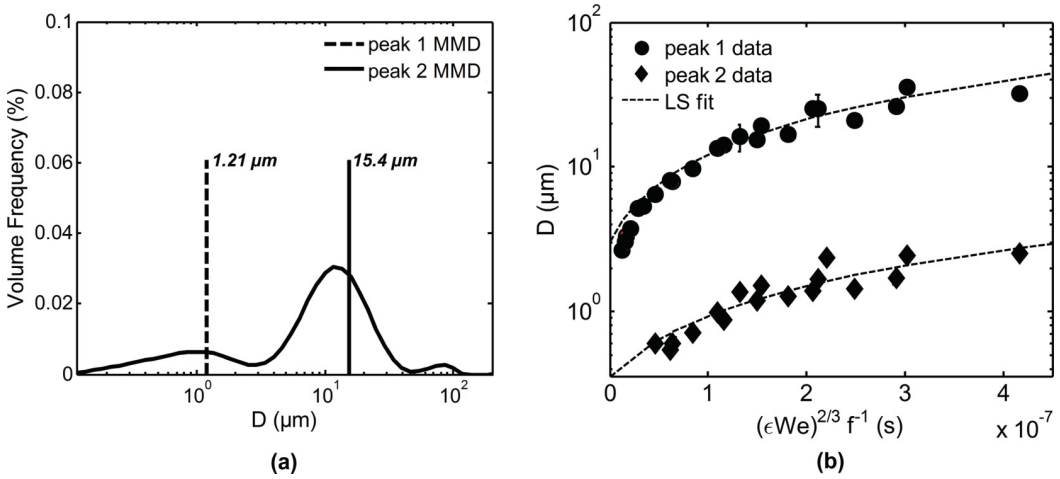

FIG. 5. (a) Experimentally measured aerosol size distribution via laser diffraction, obtained at $\omega/2\pi = 22$ MHz and an applied power of 5.2 W, corresponding to $\epsilon\mathrm{We} = 8.0$; these data are also a qualitative representation of the results obtained at other applied frequencies and powers. Three distinct peaks in the droplet sizes are observed. Peaks 1 and 2 correspond to droplets produced as a consequence of atomization off the thin film region illustrated in Fig. 1 with mass median diameters (MMDs) D of 1.21 and 15.4 μm and standard deviations of 1.04 and 9.4, respectively, computed from the volume frequency histogram of discrete droplet diameters. A third peak comprising droplets with diameters on the order of 100 μm can also be seen. These droplets are ejected from the bulk region illustrated in Fig. 1 (as only very few droplets are ejected from this region, these are not the subject of the present study that focuses on atomization from the thin film region). (b) Variation in the mass median droplet diameter D with $(\epsilon\mathrm{We})^{2/3} f^{-1}$. The data points represent the experimentally measured droplet MMD data for a range of frequencies (13–124 MHz) for each of the two peaks (i.e., peak 1 and peak 2) with droplets produced via atomization from the thin film region, and the dotted lines represent least-squares (LS) linear fitting, demonstrating the linear relationship between D and $(\epsilon\mathrm{We})^{2/3} f^{-1}$. Error bars show one standard deviation between the three 15 s measurements taken at each frequency. We also note that peak 1 failed to develop at lower values of $(\epsilon\mathrm{We})^{2/3} f^{-1}$, where frequencies exceed 98MHz ($\epsilon\mathrm{We} \lesssim 1$).

were ejected from a bulk liquid region immediately adjacent to the edge of the paper strip from which the meniscus is drawn. Smaller droplets, of typically submicron and micron dimension that are relevant for inhalation therapy, however, were ejected from a thin front-running film ahead of the bulk region. Given the interest in the use of SAW atomization to obtain large quantities of these small aerosol droplets, we focused our investigation on the spreading dynamics of this thin film region, for which a theoretical model was derived. A numerical simulation to predict the equilibrium shape of the thin film as a function of relevant system parameters revealed that the length of the thin film region was determined from a competition between capillary and acoustic forces, captured through a dimensionless acoustic Weber number, that over long times balances to form a quasisteady film. Good agreement was obtained between the theoretically predicted and experimentally measured film lengths for a range of applied powers (2.6–10.2 W) and frequencies (26–131 MHz). The film height, on the other hand, is determined by self-selection of the energy minimum state associated with the acoustic resonance present in the liquid film. Not only do we verify the resultant inverse frequency scaling using the height and length predictions with the experimental measurements, we also, for the first time, explicate the role of the applied power beyond simply influencing the onset of atomization at a critical SAW amplitude: Increasing the power drives stronger streaming in the film in the direction opposite to its spreading, therefore producing shorter films, that, in turn, lead to larger droplets, at least at moderate power levels. The film length, nevertheless, was observed to approach an asymptotic limit at higher powers, diminishing its influence on the droplet sizes as the power is further increased.

[1] J. Friend and L. Yeo, Rev. Mod. Phys. **83**, 647 (2011).
[2] L. Y. Yeo and J. R. Friend, Biomicrofluidics **3**, 012002 (2009).
[3] K. Chono, N. Shimizu, Y. Matsui, J. Kondoh, and S. Shiokawa, Jpn. J. Appl. Phys. **43**, 2987 (2004).
[4] M. Kurosawa, T. Watanabe, A. Futami, and T. Higuchi, Sens. Actuators A: Physical **50**, 69 (1995).
[5] A. Qi, L. Yeo, and J. Friend, Phys. Fluids **20**, 074103 (2008).
[6] J. Ju, Y. Yamagata, H. Ohmori, and T. Higuchi, Sens. Actuators A: Physical **145**, 437 (2008).
[7] J. Ju, Y. Yamagata, H. Ohmori, and T. Higuchi, Sens. Actuators A: Physical **147**, 570 (2008).
[8] M. Alvarez, J. Friend, and L. Yeo, Nanotechnology **19**, 455103 (2008).
[9] A. Qi, J. Friend, L. Yeo, D. Morton, M. McIntosh, and L. Spiccia, Lab Chip **9**, 2184 (2009).
[10] R. White and F. Voltmer, Appl. Phys. Lett. **7**, 314 (1965).
[11] R. P. Hodgson, M. Tan, L. Yeo, and J. Friend, Appl. Phys. Lett. **94**, 024102 (2009).

[12] J. Reboud, R. Wilson, Y. Zhang, M. H. Ismail, Y. Bourquin, and J. M. Cooper, Lab Chip **12**, 1268 (2012).
[13] J. Friend, L. Yeo, D. Arifin, and A. Mechler, Nanotechnology **19**, 145301 (2008).
[14] M. Alvarez, L. Y. Yeo, J. R. Friend, and M. Jamriska, Biomicrofluidics **3**, 014102 (2009).
[15] A. Qi, P. Chan, J. Ho, A. Rajapaksa, J. Friend, and L. Yeo, ACS Nano **5**, 9583 (2012).
[16] M. Alvarez, J. Friend, and L. Yeo, Langmuir **24**, 10629 (2008).
[17] A. Qi, Y. Yeo, J. Friend, and J. Ho, Lab Chip **10**, 470 (2009).
[18] L. Yeo, J. Friend, M. McIntosh, E. Meeusen, and D. Morton, Expert Opin. Drug Deliv. **7**, 663 (2010).
[19] S. Heron, R. Wilson, S. Shaffer, D. Goodlett, and J. Cooper, Anal. Chem. **82**, 3985 (2010).
[20] J. Ho, M. K. Tan, D. B. Go, L. Y. Yeo, J. R. Friend, and H.-C. Chang, Anal. Chem. **83**, 3260 (2011).
[21] S. H. Yoon, Y. Huang, J. S. Edgar, Y. S. Ting, S. R. Heron, Y. Kao, Y. Li, C. D. Masselon, R. K. Ernst, and D.-R. Goodlett, Anal. Chem. **84**, 6530 (2012).
[22] R. Lang, J. Acoust. Soc. Am. **34**, 6 (1962).
[23] F. Barreras, H. Amaveda, and A. Lozano, Exp. Fluids **33**, 405 (2002).
[24] M. Kurosawa, A. Futami, and T. Higuchi, in *Proceedings of the International Conference on Solid-State Sensors and Actuators* (Chicago, IL, 1997), pp. 801–804.
[25] M. Tan, J. Friend, O. Matar, and L. Yeo, Phys. Fluids **22**, 112112 (2010).
[26] A. R. Rezk, O. Manor, J. R. Friend, and L. Y. Yeo, Nat. Commun. **3**, 1167 (2012).
[27] K. Länge, B. Rapp, and M. Rapp, Anal. Bioanal. Chem. **391**, 1509 (2008).
[28] B. Chu and R. Apfel, J. Acoust. Soc. Am. **72**, 1673 (1982).
[29] C. Eckart, Phys. Rev. **73**, 68 (1948).
[30] J. Vanneste and O. Bühler, Proc. R. Soc. London A **467**, 1779 (2011).
[31] H. Schlichting, Phys. Z. **33**, 327 (1932).
[32] O. Manor, L. Y. Yeo, and J. R. Friend, J. Fluid Mech. **707**, 482 (2012).
[33] P. Brunet, M. Baudoin, O. B. Matar, and F. Zoueshtiagh, Phys. Rev. E **81**, 036315 (2010).
[34] O. Manor, M. Dentry, J. Friend, and L. Yeo, Soft Matter **7**, 7976 (2011).
[35] A. Yule and Y. Al-Suleimani, Proc. R. Soc. London A **456**, 1069 (2000).
[36] S. Shiokawa, Y. Matsui, and T. Ueda, in *Proceedings of the IEEE Ultrasonics Symposium* (IEEE, Tahoe, NV, 1989), pp. 643–646.
[37] J. Lighthill, J. Sound Vib. **61**, 391 (1978).
[38] R. Arzt, E. Salzmann, and K. Dransfeld, Appl. Phys. Lett. **10**, 165 (1967).
[39] F. Fox and W. Wallace, J. Acoust. Soc. Am. **26**, 147 (1954).
[40] W. Nyborg, J. Acoust. Soc. Am. **25**, 68 (1953).
[41] R. V. Craster and O. K. Matar, Rev. Mod. Phys. **81**, 1131 (2009).
[42] J. Kierzenka and L. Shampine, ACM Trans. Math. Software **27**, 299 (2001).

Chapter 5

On demand droplet production and encapsulation

Chapter 5 builds off in part the principles from Chapter 4, here producing droplets in a water-oil system as opposed to water and air. A water-in-oil droplet is a powerful microfluidic tool as allows for the compartmentalization of reactions; in doing so microfluidics becomes digital, potentially performing many different reactions simultaneously, though this would require methods for production and handling of individual droplets. Here we use SAW for the on-demand production of microfluidic droplets, and further demonstrate the capability to simultaneously pre-concentrate and encapsulate particles, here serving as an analogue for cells, within these droplets.

5.1 Introduction

In Chapter 4 we saw SAW used for the production of micron scale water droplets in air in order to characterize their size distribution for nebulization therapy. However, it is also possible to produce droplets in fluid-fluid mixtures as well. In Chapter 2 we introduced the concept of a water-in-oil droplet as a method for the compartmentalization of fluid reactions on-chip, with the advantages of preventing undesired diffusion barriers and making digital, multi-reaction microfluidic systems possible. In order for a lab-on-a-chip platform to be truly digital, however, the timing of droplet production is required. Though techniques exist to do this [71, 70, 214], they require externally mounted pressure sources and often produce droplets on the scale of 100s of microns and larger, both factors which practically limit either the number of reactions that can be performed or the size to which devices can be miniaturized. By incorporating a pressure source directly into the platform

where these droplets are produced, it is possible to integrate a larger number of these sources without a burdensome level of external connections. In this publication, SAW is used to generate these pressure sources on-chip. In contrast to a previously demonstrated acoustic droplet generator that required that integration of a complex piezo actuator stack into a PDMS device, SAW can be combined in a straightforward way, with the piezoelectric substrate itself forming the 2D base for the microfluidic structure as well as the IDTs. In this work, SAW was used to direct focussed acoustic pressure on a water-oil interface, ejecting individual water-in-oil droplets with each SAW pulse. By tuning the duration and power of the pulse for a given flow rate of a continuous oil phase, it is possible to define the volume of the droplets that are produced. From a 20–30 μm wide interface, droplets were produced in the range of 10s of picoliters. Additionally, because an acoustic field pervades the entire medium prior to the interface, SAW was also used to pre-concentrate particles at sub-threshold power levels. After concentration, a droplet can be produced that encapsulates these concentrated particles. Additionally, to further understand the mechanism by which droplets are produced, a simple 2D analytical model was constructed that simulates the shape of a water-oil interface subject to acoustic pressure, shown in the supplementary information following the publication. It was found that, while the directional force was able to deform the interface, the bulk of the interfacial movement is a result of the increase in hydrostatic pressure with the application of SAW.

5.2 Publication

The following publication and supplementary information was reproduced from [27] with permission from The Royal Society of Chemistry.

Monash University

Declaration for Thesis Chapter 5

Declaration by candidate

In the case of Chapter 5, the nature and extent of my contribution to the work was the following:

Nature of contribution	Extent of contribution (%)
I was chief investigator for this work. I was responsible for device design iterations and fabrication, experimental design, experimental work, numerical work, post processing and interpretation of results and writing of the paper.	80

The following co-authors contributed to the work. If co-authors are students at Monash University, the extent of their contribution in percentage terms must be stated:

Name	Nature of contribution	Extent of contribution (%) for student co-authors only
Dr. Tuncay Alan	Overall supervision and review of drafts	
Prof. Kristian Helmerson	Contributions to concept development and draft review	
A/Prof. Adrian Neild	Overall supervision and review of drafts	

The undersigned hereby certify that the above declaration correctly reflects the nature and extent of the candidate's and co-authors' contributions to this work.

Candidate's Signature	[redacted]	**Date:** 7/5/14
Signature 1	[redacted]	**Date:** 7/5/14
Signature 2	[redacted]	**Date:** 9/5/14
Signature 3	[redacted]	**Date:** 7/5/14

Lab on a Chip

RSC Publishing

PAPER

View Article Online
View Journal

Surface acoustic waves for on-demand production of picoliter droplets and particle encapsulation†

Cite this: DOI: 10.1039/c3lc50372k

David J. Collins,[a] Tuncay Alan,[a] Kristian Helmerson[b] and Adrian Neild*[a]

Microscopic water-in-oil droplets are a versatile chemical and biological platform whose dimensions result in short reaction times and require minuscule amounts of reagent. Methods exist for the production of droplets, though the vast majority are only able to do so in continuous flows, restricting the ability to independently control reactions of individual droplets, a prerequisite for programmable digital microfluidics. Here we present a novel method to produce individual picoliter-scale droplets on-demand using surface acoustic waves (SAW). Acoustic forces arising from SAW act on the oil–water interface, creating a droplet whose volume is defined by the applied power, duration of the force and system geometry. Additionally, this method is able to pre-concentrate particles simultaneously with droplet production, meaning that particles and cells, even if in a dilute mixture, can be easily encapsulated. Our method is expected to be applicable to high-throughput screening, bioreactor creation and other microfluidic processes.

Received 21st March 2013,
Accepted 30th May 2013

DOI: 10.1039/c3lc50372k

www.rsc.org/loc

Introduction

Over the past decade there has been a growing interest to develop miniaturized high throughput screening (HTS) platforms[1,2] that can replace the full functionality of microtitre plate technology on a single chip for improved efficiency and reduced costs.[3,4] This expectation, along with the recent advances in microfluidics, has attracted significant attention to droplet based systems to encapsulate reagents and targets[5,6] such as proteins or cells[7,8] into nano-to-pico-liter volumes, for subsequent reaction, transport and analysis in an enclosed microscale system.[9]

Working with samples at such small length scales enables different reagents in different concentrations to be assayed, promising orders of magnitude reduction in both the amount of reagents and the time scales compared with conventional processes.[10,11] Similarly, (1) concentration gradients that may be undesirable in a single-fluid microfluidic system can be avoided, with different phases of fluid – usually oil and water – acting as a barrier to diffusion and, (2) using a droplet as a chamber for a reaction in a two-fluid-phase microfluidic device with droplet production and analysis components integrated on-chip also allows these processes to be performed without the need for fluid handling, with the fleetingly small reaction volumes reducing the need to perform separate mixing steps. Further, nanoliter droplets encapsulating cells and particles in nanoliter volumes[7] produced in a digital microfluidic device can be used as bioreactors,[8,12,13] though until now the ability to concentrate and produce encapsulated particles on demand for a digital microfluidic device has remained elusive.

Different methods have been developed for the purpose of producing droplets in microfluidic systems, where significant effort has been made to develop and characterize T-junctions[10,14–16] and flow-focusing systems.[17,18] To produce droplets a continuous fluid flow of two immiscible fluids (typically oil and water) are required, with a constant stream of monodisperse droplets resulting from the combination of these two fluid streams. Technologies used to drive these flows, most often peristaltic pumps or syringe pumps, dispense constant flow rates but are poorly suited to accurate manipulation of discrete volumes in the sub-nanoliter range, making on-demand production of individual droplets difficult to control. Further, in most microfluidic devices the pressure gradient source is located distances away from the device that are orders of magnitude larger than the length scales of that device, introducing time delays and additional reagent volumes and causing pressure gradients to depend on the length of connecting tubing.

For digital microfluidic systems to be able to produce droplets on-demand pressure gradients should be discretely controlled on-chip. Methods that have the demonstrated ability to create localized pressure gradients sufficient to deform a fluid interface include electrowetting arrays,[19,20] electrohydrodynamic,[21] pyroelectrohydrodynamic jetting[22] and piezoelectric acoustic devices.[23–27] These mechanisms have been applied for open air droplet movement, though are

[a]Department of Mechanical and Aerospace Engineering, Monash University, Clayton, VIC 3800, Australia. [redacted]
[b]School of Physics, Monash University, Clayton, VIC 3800, Australia

† Electronic supplementary information (ESI) available: Interface deformation modeling (Discussion 1) and videos of droplet production (Video 1) and particle encapsulation (Videos 2 and 3). See DOI: 10.1039/c3lc50372k

limited in relevance to high-throughput systems by factors including large minimum reaction volume, slow translocation speed, requirement for a fluid-air interface and difficulty integrating the actuation components into a planar microfluidic system. However, acoustic forces are unusual in that they can create a time-averaged force on both fluid-fluid interfaces [27–29] and particles,[30–33] creating the possibility for these two activities to be integrated in the same device. The ability for the acoustic force to affect fluids differently based on their physical properties also allows for their use in two-phase fluid systems, in contrast to open-air systems subject to evaporation and undesired droplet coalescence. Surface acoustic waves (SAWs) are uniquely placed among acoustic actuation technologies. A SAW device is created through the patterning of interdigital transducers (IDTs) on a piezoelectric substrate such as lithium niobate (LN). Compared to most bulk acoustic wave devices, devices using SAW have the advantages of (1) having acoustic energy localized at the surface, permitting efficient energy transfer to a fluid placed on top,[34] (2) being planar and therefore easily integrated with typically 2D microfluidic devices[35,36] and (3) operating at significantly higher frequencies (~10–1000 MHz) with a corresponding wavelength (4–400 μm) encompassing the length scales on most microfluidic devices. To date, these devices have been used for diverse applications including mixing,[37] concentration,[30,32,38] continuous flow pumping,[23,39] jetting[40] and atomization.[25]

Here we present a novel and flexible method for on-demand droplet generation in digital microfluidic systems using SAW. This technique incorporates the SAW device directly into the microfluidic platform and simultaneously integrates steps for concentration, encapsulation and droplet production.

System design and operating principle

The SAW droplet generation system is composed of a microfluidic chamber placed atop a SAW device, shown in (Fig. 1a). The SAW device is composed of a series of gold focused interdigital transducers (FIDTs) arrayed on a lithium niobate (LN) substrate, with the distance between each successive transducer determining the resonant frequency, *f*,

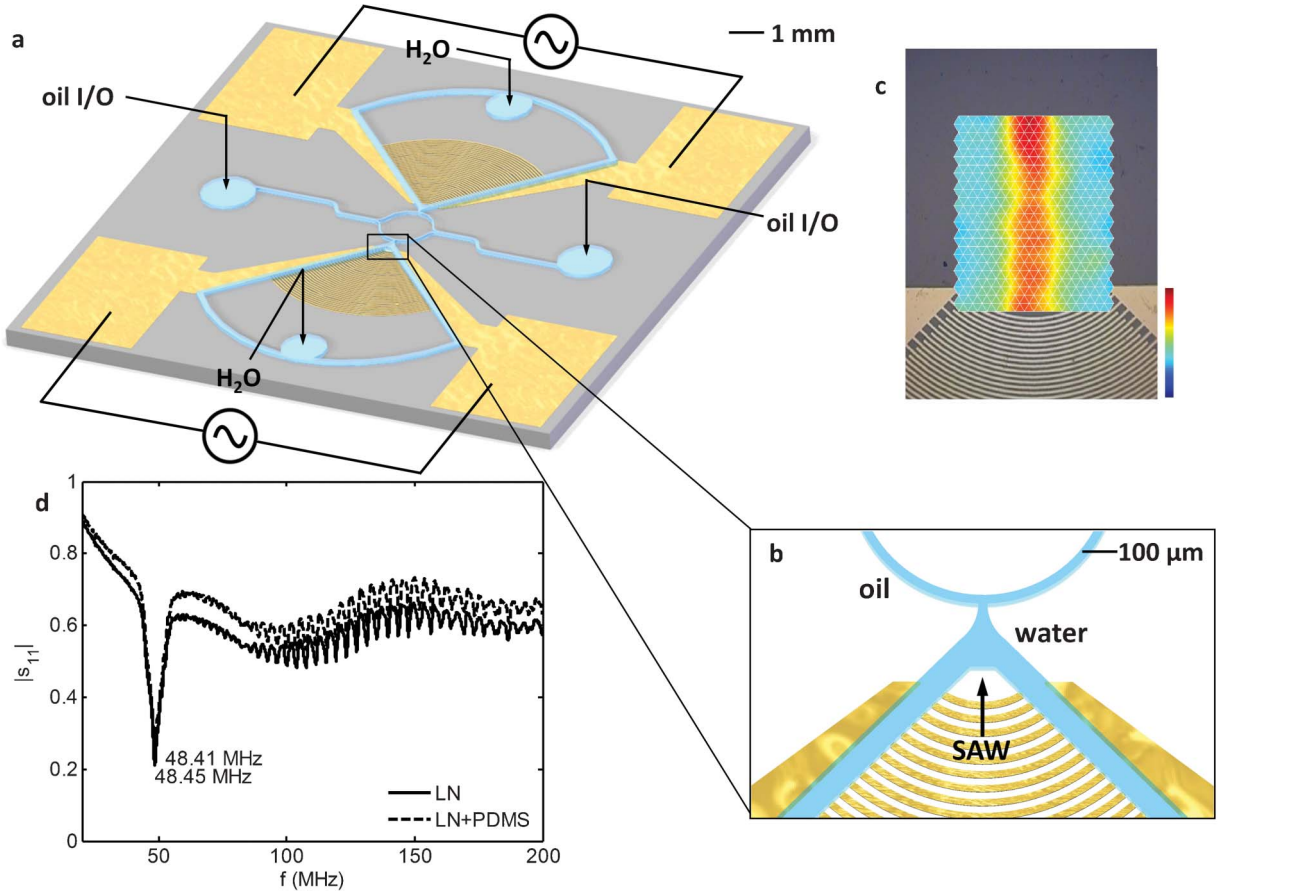

Fig. 1 Sketch of the SAW-controlled picoliter-scale droplet generation system. (a) A continuous oil phase is pumped in either symmetric oil inlet/outlet. Water is pumped in the inlets to the rear of the FIDTs until a steady water/oil interface at the microfluidic T-junction (see (b) inset) is maintained. Application of an AC signal across the electrode pads will produce a SAW, whose RMS amplitude distribution is visualized in (c), and which will act on the water–oil interface, pushing the water phase into the continuous oil phase to produce a water-in-oil droplet. (d) The resonant frequency of a SAW device is determined by its minimum reflection coefficient, or $|s_{11}|$. Loading PDMS atop a 80 μm device makes little difference to the resonant frequency.

of the device (Fig. 1d) according to $f = c_s/\lambda$, where c_s is the sound speed on the substrate surface and λ is the distance between FIDT finger-pairs. When an AC signal is applied across the transducers at this frequency the electromechanical displacement induced in the piezoelectric substrate creates a SAW, the displacement of which decays exponentially with depth into the substrate, attenuating almost completely in the first few wavelengths from the surface.[41]

The mechanics of SAW fluidics are well known: a SAW traveling at a substrate fluid interface will radiate acoustic energy into the fluid at the Rayleigh angle $\theta_R = \sin^{-1}(c_f/c_s)$, where c_f is the sound speed in the fluid. The acoustic wave, now traveling in the fluid, will continue traveling until encountering an interface with a medium of different acoustic properties. The acoustic pressure on an interface has been the focus of several publications by many prominent authors in the field of nonlinear acoustics.[42–45] Generally the acoustic radiation force on a surface in the path of an acoustic beam can here be broken up into what is called the Langevin and Rayleigh radiation pressures; the first of these refers to the time-averaged force tensor in the direction of acoustic propagation on a surface placed in the path of a beam, while the Rayleigh pressure on a surface is the combination of this and the isotropic static pressure induced. Both formulations of acoustic pressure are equally valid, though apply to different systems, depending on whether the interface the acoustic beam acts upon is suspended within a given fluid or is a physical barrier to a region with different acoustic properties. In the case of an acoustic beam acting on an oil–water interface in a closed system, there is no method to transfer the isotropic pressure induced by the beam to the oil side of the interface besides interface deformation, with the static pressure component contributing to that deformation. The Rayleigh pressure, p_r, acting on an interface is given by[43,44]

$$p_r = \langle p - p_0 \rangle + \langle \rho v^2 \rangle \quad (1)$$

where the brackets $\langle\rangle$ denote a time averaged quantity, p is the pressure in the fluid, p_0 is the initial (without acoustic actuation) pressure, ρ is the fluid density, v is the instantaneous fluid particle velocity and $\langle \rho v^2 \rangle$ is the energy density in the fluid $\langle E \rangle$. To a first approximation the fluid particle velocity $v \approx v_0$, where $v_0 = (\xi\omega)$ is the substrate velocity, ξ is the surface displacement and $\omega = 2\pi f$. If the substrate velocity is sinusoidally oscillating as in a SAW, the time average $\langle \rho v^2 \rangle$ is nonzero, resulting in a nonzero pressure term on an interface in the path of the acoustic beam. The static pressure component $\langle p - p_0 \rangle$ arises from the nonlinear propagation of the acoustic wave through the fluid, with the attenuation of acoustic energy in the wave equal to the increase in static pressure. Supplementary Discussion 1 describes and models the roles static and surface pressure arising from SAW have in deforming an oil–water interface.†

Methods

We employed 40 μm and 80 μm wavelength focused SAW devices, comprising 90 and 45 finger-pairs of 90° circular focussed interdigital transducers (FIDTs), respectively, on a 0.5 mm thick, single side polished 128° *Y-cut*, *X*-propagating lithium niobate (LN) substrate. The 10 nm chrome/200 nm aluminium FIDTs were aligned on the substrate with the SAW propagation oriented in the preferred propagation direction on the LN, as shown in Fig. 1. With the exception of the electrode pads, across which an AC signal is applied, the devices were further coated with 70 nm of evaporation-deposited SiO_2 to cover the IDTs and promote adhesion with polydimethylsiloxane (PDMS), which was bonded to the device after exposure to an activated air plasma (Harrick Plasma PDC-002, Ithaca, NY: 450 mTorr, 29.6W, 3 min for the SiO_2-coated LN substrate and 1.5 min for the PDMS). Bonding of the activated surfaces was enhanced by heating the joined surfaces (70 °C, 10 min) immediately following coupling. Several chamber geometries were explored, including devices where the IDTs were covered entirely by PDMS (results in Fig. 2a–e) or fluid (Fig. 2f–g, 3, 4). Both setups are capable of producing water-in-oil droplets, though higher powers are required to produce equivalent results when PDMS is bonded directly to the IDTs due to lossy SAW transmission at the LN-PDMS interface.[46]

Experiments were performed with the device stabilized on a 3D-printed platform and placed on the stage of a microscope (Olympus BX43, Tokyo, Japan) and imaged using a 5MP eyepiece camera (Dino-Lite AM7023B, New Taipei City, Taiwan). Olive oil (viscosity =85 cP, surface tension at oil–water interface is $\approx$0.024 N m^{-1}[47]), comprising the continuous flow stream, was injected into the device using a syringe pump (KD Scientific Legato 210, Holliston, MA, USA), whereas water was manually manipulated using a 1 mL syringe until a steady-state (flat) oil–water interface was achieved. The SAW was generated by applying a sinusoidal voltage across the electrode pads using a signal generator (BelektroniG F10, Freital, Germany) and amplifier. Surface velocity was measured and the traveling wave SAW was visualized in the vicinity of the FIDT focal point using a laser Doppler vibrometer (Polytech GmBH UHF-120, Waldbronn, Germany). Temperature measurements were made using a thermal imaging camera (FLIR i7, Meer, Belgium).

Results

Droplet generation

The simplest geometry for droplet production in microfluidic systems is the T-junction, where a continuous (oil) phase is intersected by a disperse (water) phase. In Fig. 2 a modified T-junction is integrated with a SAW device with the orifice located at the FIDT focal point. Application of SAW to the oil–water interface leads to interface deformation, extending the water into the oil phase leading to droplet production (see Supplementary Video 1). In the context of continuous droplet

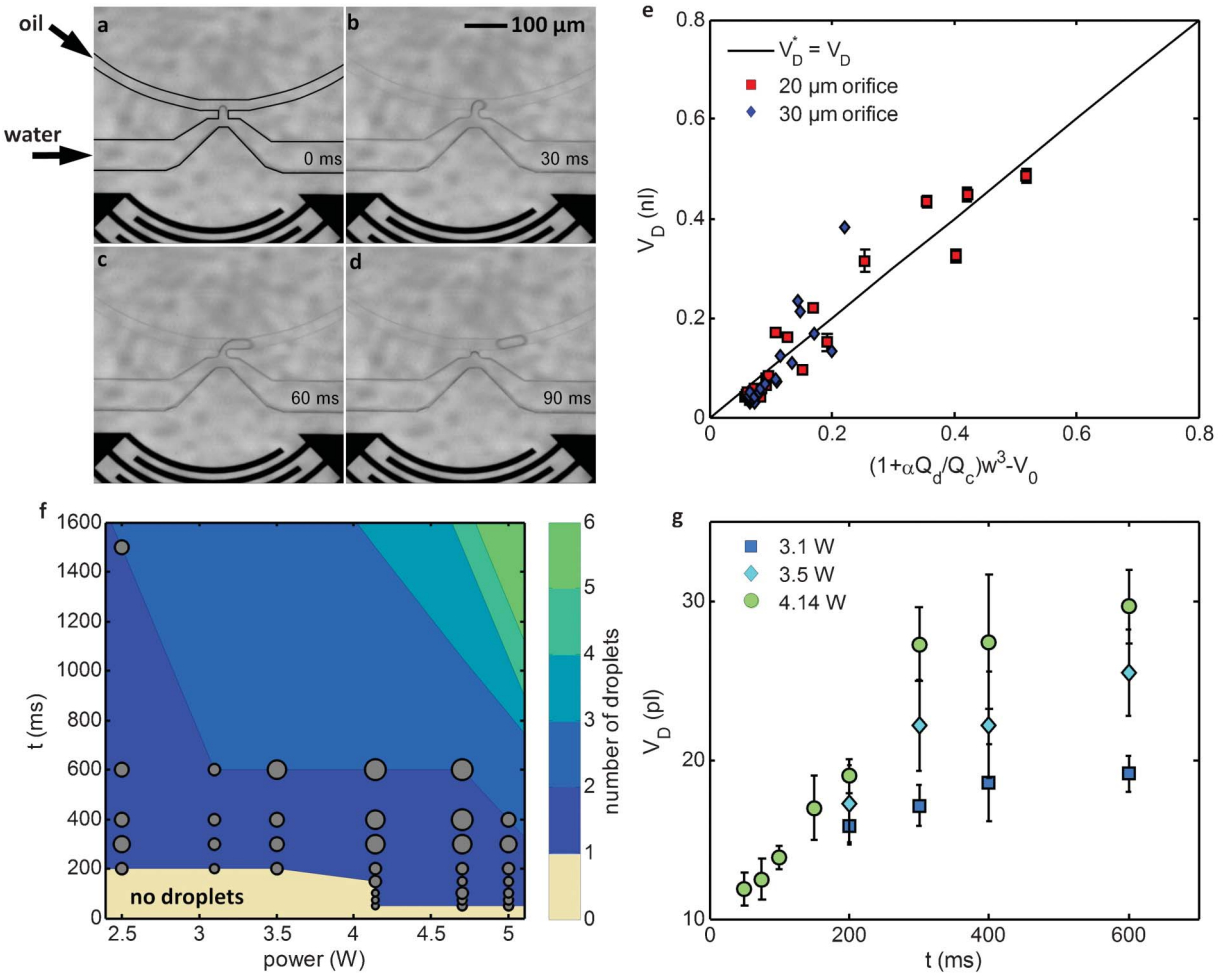

Fig. 2 (a–d) Images (~30 ms apart) of droplet production in a confined system comprised of a 20/30 µm width/height orifice and a 30/30 µm width/height circular channel of radius 745 µm, with (a) showing the water–oil interface immediately after application of SAW, (b–c) showing interface deformation due to acoustic pressure and channel cross flow, and (d) a fully formed droplet in channel. Droplet is produced when SAW of FIDT wavelength 80 µm is applied for 100 ms at 48.4 MHz, starting at (a) and ending at (c). (e) The droplet volume V_D produced with application of SAW is determined by flow rate in the channel. A constant pulse results in an outlet velocity of 2.1 ± 0.5 mm s^{-1}, resulting in a flow ratio Q_d/Q_c essentially solely determined by the oil flow rate. Incorporating Q_d/Q_c, where Q_d is inferred by the ejection rate of water into the oil stream, into eqn (3) yields a satisfactory comparison with measured droplet sizes. (f) The number of droplets produced using a 20/30 µm width/height orifice and channel is determined by the power level (2.5–5 W) and pulse duration (50–1500 ms). (g) The droplet volume (grey circles in (f)) is similarly determined by these factors, with increasing volume for increased power and duration, here shown for 3.1–4.14 W for the case where <2 droplets are produced.

production, the intrusion of the disperse phase into the continuous phase results in droplet break-off, a mechanism that has been well-covered in the existing literature.[14,48–50] The droplet breakup regime is determined by the capillary number Ca = $\mu u/\gamma$, where u is the velocity of the continuous phase in the channel, μ is the fluid viscosity and γ is the interfacial tension, with the critical capillary number Ca* ≈ 0.015 determining the transition from the so-called squeezing to dripping regimes.[14] The velocities characteristic to most microfluidic systems result in Ca < Ca*, where droplet size is unaffected by viscous shear and where droplet formation in a T-junction occurs in a roughly four-stage process: (1) a disperse phase fluid enters a continuous phase channel (Fig. 2a), (2) the disperse phase fills the width of the channel (Fig. 2b), (3) the pressure drop, arising from the thinning boundary layer in the continuous phase, lengthens the disperse phase drop and (4) the thinning neck at the boundary of the orifice (Fig. 2c) breaks to form a drop in the continuous phase channel (Fig. 2d). It is known from Garstecki *et al.* that in this regime the length of droplets in a channel is only determined by the channel geometry and flow rates of the continuous, Q_c, and disperse, Q_d, phases according to the expression[48]

$$\ell/w = 1 + \alpha Q_d/Q_c \quad (2)$$

where ℓ is the length of the drop in the channel, w is the channel width and α is a constant specific to the chamber geometry and of order unity. In a square channel, the predicted droplet volume $V_D^* \sim Lw^2$; subtracting the empty

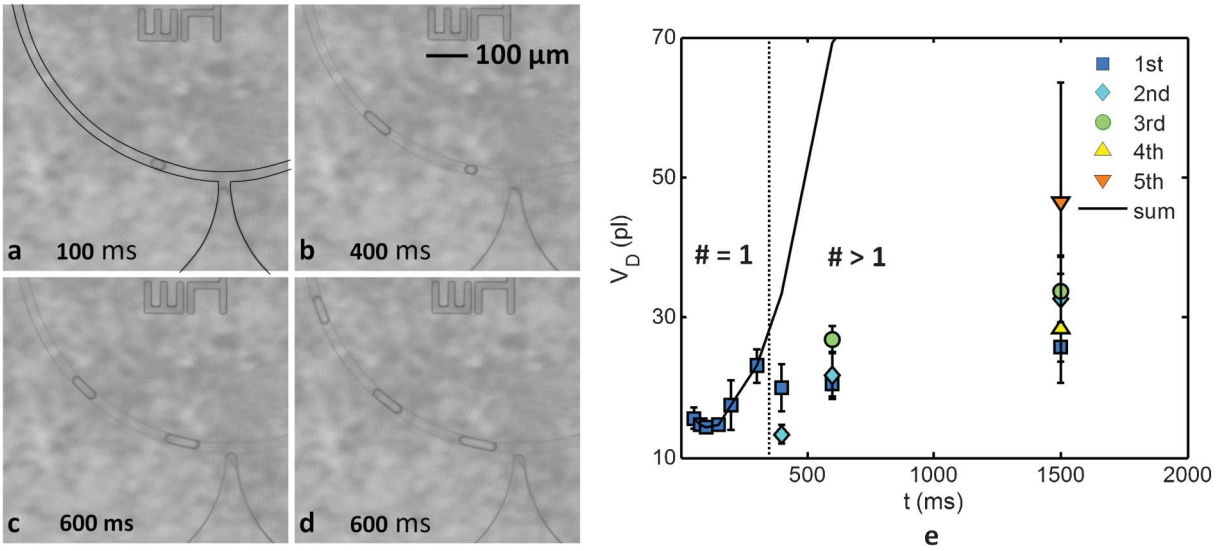

Fig. 3 (a–d) Images showing droplets that are produced for different pulse durations (100–600 ms), with (c) and (d) from the same droplet sequence shown 200 ms apart. (e) The droplet size produced during multi-droplet production is dependent on the duration of the pulse. For pulses less than ~350 ms in duration (here at 5 W), only one (# = 1) droplet is produced (see Fig. 2f). A pulse longer than that required to produce a single droplet can produce additional droplets (# > 1), though the volume of the last droplet in a series may be smaller than the initial droplet if the SAW pulse ceases during formation (b). If this does not occur, subsequent droplets will be larger, suggesting accelerating rates of interface deformation.

volumes at leading and trailing edges of the drop and assuming circular curvature at both ends yields $V_D^* \approx Lw^2 - V_0$, where the subtracted empty volume $V_0 = w^3(1 - \pi/6)$. Incorporating eqn (2), the volume of a drop in a channel is given by

$$V_D^* = w^3(\alpha Q_d/Q_c + \pi/6) \quad (3)$$

where Q_d here is determined by the rate of interface movement on application of SAW. Increasing power and duration results in larger droplets (Fig. 2g), here increasing the effective Q_d.

For a constant Q_c the ejected droplet volume is a function of both the applied power and SAW pulse duration. Finding that the water ejection velocity is constant for a given applied power, the droplet size for increasing flow velocities with $u = Q_c/w^2$ is found to agree with model in eqn (3), observed in

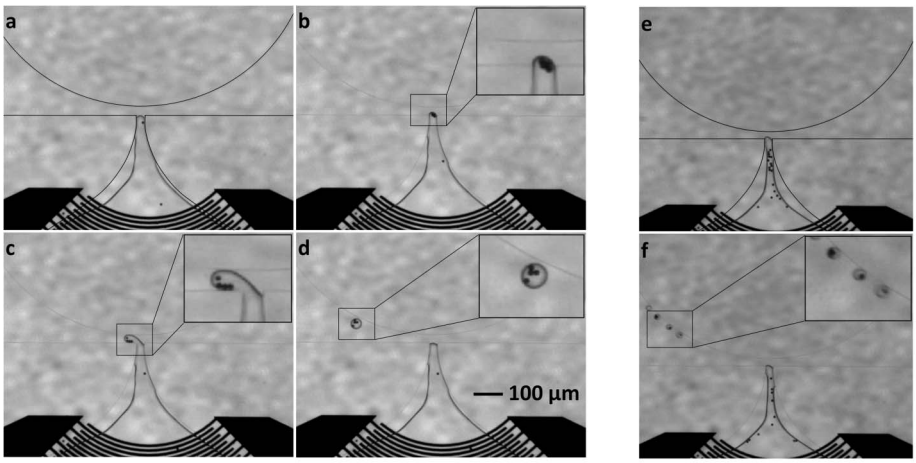

Fig. 4 Two modes of particle concentration and encapsulation during droplet production on a 95.4 MHz (40 µm wavelength) SAW device. (a–d) Discrete droplets encapsulating 10 µm particles are produced when (a) a dilute particle solution at rest is (b) excited by a low-power (1 W) SAW for a set period (2 s), concentrating particles at the interface. (c) The application of a high-power pulse (>2 W) for 100 ms is used to deform the interface, pushing it into the oil phase, which subsequently breaks off due to the pressure differential on either side of the protrusion leading to (d) a water-in-oil droplet encapsulating the particles previously concentrated at the interface. (e,f) Continuous encapsulation of individual particles occurs at higher oil flow rates and application of SAW (here 4 W). (e) The particle solution is semi-concentrated near the orifice whereupon (f) a burst of SAW creates a series of 8 pl droplets each containing one or two particles. The PDMS boundaries are highlighted in (a,e) for clarity.

Fig. 2e. Additionally, the system has the potential to generate multiple droplets with each pulse, with longer durations (>400 ms) at higher powers giving rise to additional droplets (Fig. 2f). The size of the additional droplets is determined by the specific system kinetics for a given power and pulse duration (Fig. 3). Secondary, tertiary, *etc.* droplets are generally larger, though pulse shutoff during the production of a given droplet can result in a smaller secondary droplet (Fig. 3b).

Particle concentration and encapsulation

When an acoustic wave interacts with a particle, much as when it interacts with any interface, it imparts a time-averaged force on that particle in the direction of propagation. In the case of the SAW device setup in Fig. 1 this means that particles located in water can be concentrated at the oil–water interface prior to droplet creation, resulting in an water-encapsulated particle (see Supplementary Videos 2 and 3†), a process that could easily be applied to individual cells. Fig. 4 shows two methodologies to produce encapsulated 10 μm particles. In Fig. 4(a–d) applying a relatively low-power SAW to translate particles for a short period (1–5 s) concentrates particles at the orifice, with a subsequent high-power pulse of short duration (<100 ms) sufficient to displace the interface into the oil flow sufficiently to result in droplet break-off. In Fig. 4(e,f) continuous application of SAW is used to simultaneously concentrate particles near the orifice and produce droplets. It is important to note that the frequency and particle size have significant bearing on the ability for SAW to concentrate particles at the interface. For a particle of radius R subject to a traveling acoustic wave the acoustic radiation force $F_t \sim f^4, R^6$: higher frequencies and larger particles will result in drastically more effective collection.[51] Additionally, the standing wave force for a constant pressure amplitude, where $F_s \sim f, R^3$, will overpower the travelling wave force at lower frequencies. In the setup tested here with the particle solution directly atop the interdigital transducers, a 95.4 MHz device was able to push particles to the interface, while in a 48.4 MHz device particles instead move to the standing wave nodes in between IDT finger-pairs. Most acoustic microfluidic devices utilize standing waves to manipulate particles[38,52–55] because the standing wave force is stronger for frequencies typically utilized. The application here is one of the few cases where the traveling wave force is both dominant and desired for directional particle concentration, a notable exception being a case where 140 MHz SAW was used to direct (substantially larger) ~100 μm droplets.[56] While high-frequency SAW is broadly compatible with biomolecules and cells,[34,55] thermal effects must be considered when relatively high power pulses (here up to 5 W) are used. Over an example test period used to produce droplets (5 pulses over 10 s for time-averaged power densities of 0.4 W) the temperature increase was observed to be <2 °C. For longer test periods, the thermal conductivity of the surface on which the device is placed significantly affects the steady state temperature of the device, with active thermal cooling (as in the case of a peltier cooler) limiting steady-state temperature increases by as little as <3 °C.

Conclusion

In summary, we have developed a novel system for the on-demand production of individual water-in-oil droplets using high-frequency SAW and demonstrated encapsulation of particles in vesicles. Our SAW system offers the advantage of combining droplet production, concentration and encapsulation in a single device, hence allowing direct integration with digital microfluidic devices for chemical or biological assays. Droplet creation here does not require the use of surfactants, emulsifiers or other fluid treatments that may affect chemical or cell processes, and can be powered by readily miniaturizable high-frequency power circuits. Integration of multiple devices integrated on a single platform allows simultaneous parallel processing for biochemical assays. The multiple operating modes for droplet production and particle encapsulation offered by the system presented here, including both single on-demand and continuous production, means this method can be flexibly applied to a variety of microfluidic systems.

Acknowledgements

Fabrication of the SAW actuators and device assembly was performed at the Melbourne Center for Nanofabrication.

References

1 R. Macarron, M. N. Banks, D. Bojanic, D. J. Burns, D. A. Cirovic, T. Garyantes, D. V. Green, R. P. Hertzberg, P. J. W. S. U. Janzen, P. William and G. S. Sittampalam, *Nat. Rev. Drug Discovery*, 2011, **10**, 188.
2 X. Niu, F. Gielen, J. B. Edel and A. J. deMello, *Nat. Chem.*, 2011, **3**, 437.
3 A. Wixforth, *J. Assoc. Lab. Autom.*, 2006, **11**, 399.
4 L. M. Mayr and D. Bojanic, *Curr. Opin. Pharmacol.*, 2009, **9**, 580.
5 S. S. Bithi and S. A. Vanapalli, *Biomicrofluidics*, 2010, **4**, 044110.
6 M. Sun, S. S. Bithi and S. A. Vanapalli, *Lab Chip*, 2011, **11**, 3949.
7 J. F. Edd, D. Di Carlo, K. J. Humphry, S. Köster, D. Irimia, D. A. Weitz and M. Toner, *Lab Chip*, 2008, **8**, 1262.
8 Y.-C. Tan, K. Hettiarachchi, M. Siu, Y.-R. Pan and A. P. Lee, *J. Am. Chem. Soc.*, 2006, **128**, 5656.
9 H. A. Stone, A. D. Stroock and A. Ajdari, *Annu. Rev. Fluid Mech.*, 2004, **36**, 381.
10 H. Song, D. Chen and R. Ismagilov, *Angew. Chem., Int. Ed.*, 2006, **45**, 7336.
11 M. Kiss, L. Ortoleva-Donnelly, N. Beer, J. Warner, C. Bailey, B. Colston, J. Rothberg, D. Link and J. Leamon, *Anal. Chem.*, 2008, **80**, 8975.
12 A. Doerr, *Nature*, 2005, **200**, 5.
13 M. He, J. S. Edgar, G. D. Jeffries, R. M. Lorenz, J. P. Shelby and D. T. Chiu, *Anal. Chem.*, 2005, **77**, 1539.
14 G. Christopher, N. Noharuddin, J. Taylor and S. Anna, *Phys. Rev. E*, 2008, **78**, 036317.

15 J. Xu, S. Li, J. Tan and G. Luo, *Microfluid. Nanofluid.*, 2008, **5**, 711.
16 S. Okushima, T. Nisisako, T. Torii and T. Higuchi, *Langmuir*, 2004, **20**, 9905.
17 S. Anna, N. Bontoux and H. Stone, *Appl. Phys. Lett.*, 2003, **82**, 364.
18 A. Gañán-Calvo and J. Gordillo, *Phys. Rev. Lett.*, 2001, **87**, 274501.
19 M. Pollack, A. Shenderov and R. Fair, *Lab Chip*, 2002, **2**, 96.
20 J. Ding, K. Chakrabarty and R. B. Fair, *IEEE Trans. Comput.-Aided Des. Integr. Circuits Syst.*, 2001, **20**, 1463.
21 C.-H. Chen, D. Saville and I. Aksay, *Appl. Phys. Lett.*, 2006, **89**, 124103.
22 P. Ferraro, S. Coppola, S. Grilli, M. Paturzo and V. Vespini, *Nat. Nanotechnol.*, 2010, **5**, 429.
23 M. Cecchini, S. Girardo, D. Pisignano, R. Cingolani and F. Beltram, *Appl. Phys. Lett.*, 2008, **92**, 104103.
24 A. Bransky, N. Korin, M. Khoury and S. Levenberg, *Lab Chip*, 2009, **9**, 516.
25 D. Collins, O. Manor, A. Winkler, H. Schmidt, J. Friend and L. Yeo, *Phys. Rev. E*, 2012, **86**, 056312.
26 A. R. Rezk, O. Manor, J. R. Friend and L. Y. Yeo, *Nat. Commun.*, 2012, **3**, 1167.
27 L. Schmid and T. Franke, *Lab Chip*, 2013, **13**, 1691–1694.
28 G. Hertz and H. Mende, *Z. Phys.*, 1939, **114**, 354.
29 T. Franke, S. Braunmüller, L. Schmid, A. Wixforth and D. Weitz, *Lab Chip*, 2010, **10**, 789.
30 A. Neild, S. Oberti and J. Dual, *Sens. Actuators, B*, 2007, **121**, 452.
31 S. Oberti, D. Moeller, A. Neild, J. Dual, F. Beyeler, B. Nelson and S. Gutmann, *Ultrasonics*, 2010, **50**, 247.
32 J. Reboud, Y. Bourquin, R. Wilson, G. S. Pall, M. Jiwaji, A. R. Pitt, A. Graham, A. P. Waters and J. M. Cooper, *Proc. Natl. Acad. Sci. U. S. A.*, 2012, **109**, 15162.
33 R. Walker, I. Gralinski, K. Keong Lay, T. Alan and A. Neild, *Appl. Phys. Lett.*, 2012, **101**, 163504.
34 L. Y. Yeo and J. R. Friend, *Biomicrofluidics*, 2009, **3**, 012002.
35 A. Wixforth, *Superlattices Microstruct.*, 2003, **33**, 389.
36 C. J. Strobl, Z. von Guttenberg and A. Wixforth, *IEEE Trans. Ultrason. Ferroelectr. Freq. Control*, 2004, **51**, 1432.
37 R. Shilton, M. Tan, L. Yeo and J. Friend, *J. Appl. Phys.*, 2008, **104**, 014910.
38 J. Shi, X. Mao, D. Ahmed, A. Colletti and T. Huang, *Lab Chip*, 2008, **8**, 221.
39 M. Tan, L. Yeo and J. Friend, *Europhys. Lett.*, 2009, **87**, 47003.
40 M. Tan, J. Friend and L. Yeo, *Phys. Rev. Lett.*, 2009, **103**, 24501.
41 J. Friend and L. Yeo, *Rev. Mod. Phys.*, 2011, **83**, 647.
42 J. Rooney and W. Nyborg, *Am. J. Phys.*, 1972, **40**, 1825.
43 B. Chu and R. Apfel, *J. Acoust. Soc. Am.*, 1982, **72**, 1673.
44 R. Beyer, *J. Acoust. Soc. Am.*, 1978, **63**, 4.
45 T. Hasegawa, T. Kido, T. Iizuka and C. Matsuoka, *Acoustical Science and Technology*, 2000, **21**, 145.
46 S. M. Langelier, L. Y. Yeo and J. Friend, *Lab Chip*, 2012, **12**, 2970.
47 L. Fisher, E. Mitchell and N. Parker, *J. Food Sci.*, 1985, **50**, 1201.
48 P. Garstecki, M. Fuerstman, H. Stone and G. Whitesides, *Lab Chip*, 2006, **6**, 437.
49 P. Garstecki, I. Gitlin, W. DiLuzio, G. M. Whitesides, E. Kumacheva and H. A. Stone, *Appl. Phys. Lett.*, 2004, **85**, 2649.
50 M. De Menech, P. Garstecki, F. Jousse and H. Stone, *J. Fluid Mech.*, 2008, **595**, 141.
51 L. V. King, *Proc. R. Soc. London, Ser. A*, 1934, **147**, 212.
52 A. Nilsson, F. Petersson, H. Jönsson and T. Laurell, *Lab Chip*, 2004, **4**, 131.
53 F. Petersson, A. Nilsson, C. Holm, H. Jönsson and T. Laurell, *Lab Chip*, 2005, **5**, 20.
54 X. Ding, S.-C. S. Lin, B. Kiraly, H. Yue, S. Li, I.-K. Chiang, J. Shi, S. J. Benkovic and T. J. Huang, *Proc. Natl. Acad. Sci. U. S. A.*, 2012, **109**, 11105.
55 J. Shi, D. Ahmed, X. Mao, S.-C. S. Lin, A. Lawit and T. J. Huang, *Lab Chip*, 2009, **9**, 2890.
56 T. Franke, A. R. Abate, D. A. Weitz and A. Wixforth, *Lab Chip*, 2009, **9**, 2625.

Electronic Supplementary Material (ESI) for Lab on a Chip

I. SUPPLEMENTARY DISCUSSION S1 - INTERFACE DEFORMATION USING SAW

The acoustic pressure on an interface has been the focus of several publications by many prominent authors in the field of nonlinear acoustics. [1–4]. The acoustic radiation force on a surface in the path of an acoustic beam can be generally broken up into the Langevin and Rayleigh radiation pressures; the first of these refers to the time-averaged force tensor in the direction of acoustic propagation on a surface placed in the path of a beam, while the Rayleigh pressure on a surface is the combination of this and the isotropic static pressure induced. Both formulations of acoustic pressure are equally valid, though apply to different systems, depending on whether the interface the acoustic beam is confined by the interface it acts upon. In the case of an acoustic beam acting on an oil-water interface, there is no method, aside from interface movement, to transfer the isotropic pressure induced by the beam to the oil side of the interface, meaning this component of the pressure will influence the interface shape and must be taken into account. The Rayleigh pressure acting on an interface is then given by [2, 3]

$$p_r = \langle p - p_0 \rangle + \langle \rho v^2 \rangle, \tag{1}$$

where v is the instantaneous fluid particle velocity and $\langle \rho v^2 \rangle$ is simply $\langle E \rangle$, the energy density in the fluid. To a first order approximation the fluid particle velocity $v \approx v_0$, where $v_0 = (\xi\omega)$ is the substrate velocity, ξ is the surface displacement and ω is the angular frequency. If the substrate velocity is oscillating sinusoidally as in a SAW, the time average $\langle \rho v^2 \rangle$ is nonzero, resulting in a nonzero pressure term in a fluid media placed on top of the substrate. In terms of the Fox and Wallace coefficients [5], which are determined by the first and second order compressibility of a fluid, Eq. (1) can be expressed as

$$p_r = \frac{B}{2A}\langle E \rangle + \langle E \rangle, \tag{2}$$

where the first term on the right side represents the static pressure term, and the second term arises from the nonlinear interaction between the acoustic wave and the water-oil interface. To model the interaction of an acoustic beam arising from surface acoustic waves (SAW) with the water-oil interface, the static pressure terms and the force term at the interface need to be treated separately as the surface topology of the interface will be non-planar during droplet formation. Eq. (2) can then be written as

$$p_r = \frac{B}{2A}\langle E_0 \rangle + \sin\left(\phi(z) - \theta_R\right)\langle E_1 \rangle, \tag{3}$$

where $\sin\left(\phi(z) - \theta_R\right)$ is the vector normal to the interface surface and $\langle E_0 \rangle$, $\phi(z) = \tan^{-1}(\partial h/\partial z)$ the inclination angle of the interface in the $x-z$ plane, where x projects horizontally along the SAW propagation direction and z projects vertically from the substrate to the PDMS upper surface, with h being the distance between any point on the interface and the orifice and $\langle E_1 \rangle$ representing the energy density in the water bulk and at the water-oil interface. Whereas $\langle E_0 \rangle$ is simply equal to $\langle \rho v_0^2 \rangle$ [3], the energy density at the interface must take into account that the oil-water boundary is only partially reflecting, with the energy density given here as a function of the density and sound speeds in oil (ρ_o, c_o) and water (ρ_w, c_w) [2];

$$\langle E_1 \rangle = \frac{2\left[1 + \left(\frac{\rho_o c_o}{\rho_w c_w}\right)^2\right]\langle E_0 \rangle}{\left(1 + \frac{\rho_o c_o}{\rho_w c_w}\right)^2}. \tag{4}$$

At steady state the acoustic pressure at the oil-water interface is balanced by the capillary pressure – $p_c = p_r$. Assuming the interface shape is equivalent in both the $x-z$ and $x-y$ plane, i.e. a square orifice shape with $p_c(x, z(\tau)) \approx p_c(x, y(\tau))$, then p_c is simply twice the value in the $x-z$ plane, with

$$p_c \approx -2\gamma\frac{\partial^2 h}{\partial z^2}, \tag{5}$$

where $\gamma \approx 0.024$ N/m [6] is the value for surface tension at the oil-water interface. Combining the capillary pressure in Eq. (5), the Rayleigh pressure in Eq. (3) and the capillary pressure of an oil-water interface at rest yields the final steady state interface shape equation;

$$2\gamma\frac{\partial^2 h}{\partial z^2} = \frac{B}{2A}\langle E_0 \rangle + \sin\left(\phi(z) - \theta_R\right)\langle E_1 \rangle - \gamma\frac{1}{L}, \tag{6}$$

where L is the length scale of the orifice. If the interface is pinned at the borders of the orifice, the boundary conditions can be specified by

$$h|_{z^*=0} = 0 \qquad h|_{z^*=1} = 0, \tag{7}$$

Equations (6) and (7) were solved numerically on a mesh of 1000 points using MATLAB's boundary value problem solver `bvp4c` [7] on the domain $z^* = [0, 1]$, where $z^* = z/L$ and $x^* = x/L$. The interface shape for different v_0 is given in Fig. 1 for both the Langevin (Fig. 1a) and Rayleigh (Fig. 1b) radiation pressures. Note that if the static pressure term in omitted, the interface shape tends towards θ_R.

[1] J. Rooney and W. Nyborg, American Journal of Physics **40**, 1825 (1972).

[2] B. Chu and R. Apfel, The Journal of the Acoustical Soci-

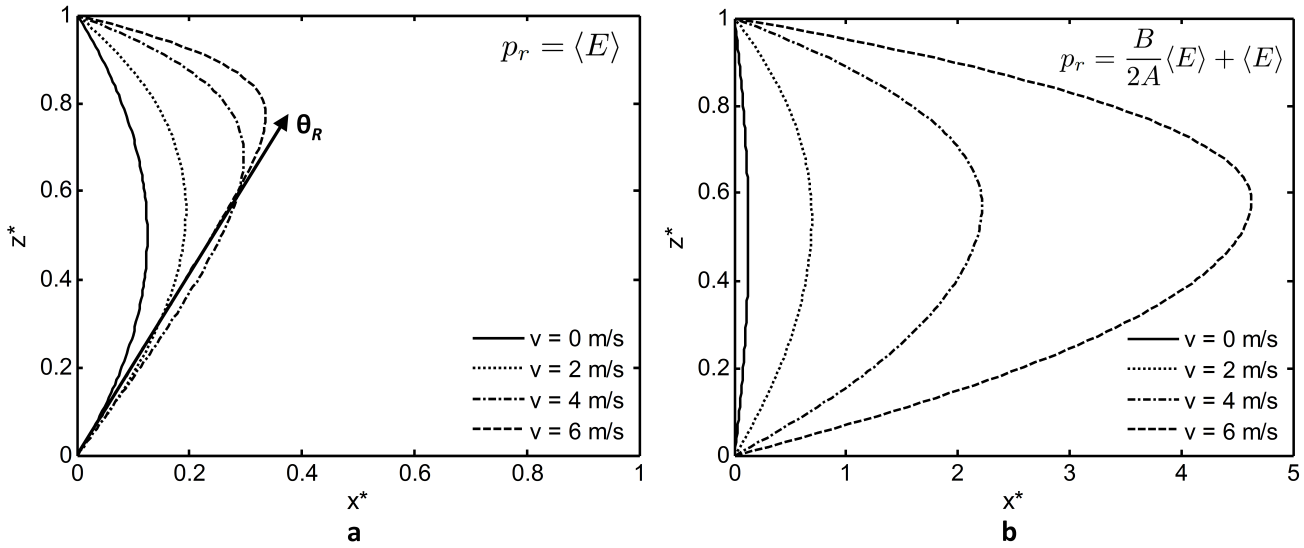

FIG. 1. A fluid-fluid interface (here oil and water) will be deformed by a time averaged second order acoustic radiation pressure, provided the two fluids have a non-zero acoustic contrast. In the case of an incident travelling wave, both the direct interfacial and static pressures pressures will determine the interface shape. (a) Considering only the pressure due to the nonlinear interaction between the interface and acoustic wave (the so-called Langevin radiation pressure), with the waves traveling upward from the SAW substrate at the Rayleigh angle θ_R, this figure shows the steady-state water-oil interface shape for different particle velocities (v = 0, 2, 4 and 6 m/s) in the fluid at a square orifice, where $v \approx v_0 = \xi\omega$, the substrate surface velocity. If only the Langevin pressure is accounted for, the leading edge of the meniscus is generally unable to exceed the line denoted by θ_R, and is unable to advance into the channel sufficiently for droplet formation. (b) Shows the same interface shapes when the static pressure component, due to the nonlinear propagation of an acoustic wave through the fluid medium (water), is taken into account.

ety of America **72**, 1673 (1982).
[3] R. Beyer, The Journal of the Acousical Society of America **63**, 4 (1978).
[4] T. Hasegawa, T. Kido, T. Iizuka, and C. Matsuoka, Acoustical Science and Technology **21**, 145 (2000).
[5] F. Fox and W. Wallace, The Journal of the Acoustical Society of America **26**, 994 (1954).
[6] L. Fisher, E. Mitchell, and N. Parker, Journal of Food Science **50**, 1201 (1985).
[7] J. Kierzenka and L. Shampine, ACM Transactions on Mathematical Software **27**, 299 (2001).

Chapter 6

Particle trapping, concentration and release

As the sophistication of lab-on-a-chip systems increases gating functions such as controlled concentration and release will become increasingly important. In Chapter 6 we expand on the ability to pre-concentrate and release particles on-demand, doing so in this case in a continuous flow, single phase system. This is done at extremely low powers – on the order of milliwatts – and is made possible by the use of an easily fabricated, quasi-3D membrane structure against which particles are pushed and trapped. Because the force used to trap these particles is larger for larger smaller particles, this systems is also demonstrated as a particle sorter, with larger particles trapped and smaller ones continuing in the direction of the flow.

6.1 Introduction

In Chapter 5 a method using SAW was developed to pre-concentrate and encapsulate particles in a two-phase system. This method is directly applicable to digital microfluidic applications such as high throughput screening, where multiple reagents can be independently mixed and analyzed. Here, the ability to produce and release droplets on-demand is critical. However, it may not always be desirable to perform reactions in a two-phase system; washing cells in buffer or nutrient solution, for example, becomes problematic if they cannot be exposed to a continuous flow. With this in mind, the ability to perform similar controlled concentration and release operations on particles and cells in a single phase would be beneficial. Furthermore, these abilities are important in many other potential applications, where increased concentration in a cell sample would, for

example, enhance detection efficiency. As was demonstrated in Chapter 5, SAW can be utilized to move particles in the direction of acoustic propagation. In this Chapter we make use of a different geometry and device combined with SAW to concentrate and release particles on-demand in a single fluid phase. Though particle manipulation strategies have been developed that have the potential to perform similar activities, none have the flexibility and other advantages that this method affords. Here, a traveling wave acoustic force is used to push particles vertically against a physical membrane in the path of a flow containing particles. Doing so confers significant power efficiency benefits. Because the acoustic beam at the SAW-water interface propagates at the Rayleigh angle θ_R, the force on particles in a fluid is primarily directed vertically rather than horizontally, the force direction used in essentially all other SAW particle manipulation systems. Additionally, because the particles are held in place by a physical barrier rather than a virtual one and in a low flow region of the channel (see Appendix B), only a fraction of the acoustic force, and therefore electrical power, is required to hold particles in position. It will be shown here that trapping of 5 μm particles can be filtered and concentrated with power on the order of milliwatts, a low level of power required only in other currently used portable RF devices; using these low levels of power makes the integration of SAW methods into portable point-of-care lab-on-a-chip systems possible.

Further, this flexible design is utilized as a size-dependent particle filter/separator. Due to the size-dependent nature of the traveling wave acoustic force, with $F \sim R^6$, smaller particles experience substantially smaller forces than larger particles. Applying a sufficient force to retain larger particles that is insufficient to do the same for smaller particles, these particle populations can be separated. With the exception of the work presented subsequently in Chapter 7, this method is even more size sensitive than even dedicated SAW-based sorting methods.

6.2 Publication

This article was in review at the time of thesis submissions with *Applied Physics Letters*, but is now presented here in its current published form as of October 2014. The following publication is now reproduced from[215] with permission from The American Institute of Physics.

Monash University

Declaration for Thesis Chapter 6

Declaration by candidate

In the case of Chapter 6, the nature and extent of my contribution to the work was the following:

Nature of contribution	Extent of contribution (%)
I was chief investigator for this work. I was responsible for device design iterations and fabrication, experimental design, experimental work, post processing and interpretation of results and writing of the paper.	85

The following co-authors contributed to the work. If co-authors are students at Monash University, the extent of their contribution in percentage terms must be stated:

Name	Nature of contribution	Extent of contribution (%) for student co-authors only
Dr. Tuncay Alan	Overall supervision and review of drafts	
A/Prof. Adrian Neild	Overall supervision and review of drafts	

The undersigned hereby certify that the above declaration correctly reflects the nature and extent of the candidate's and co-authors' contributions to this work.

Candidate's Signature	[redacted]	**Date:** 7/5/14
Signature 1		**Date:** 7/5/14
Signature 2		**Date:** 7/5/14

The particle valve: On-demand particle trapping, filtering, and release from a microfabricated polydimethylsiloxane membrane using surface acoustic waves

David J. Collins, Tuncay Alan, and Adrian Neild[a)]
Laboratory for Microsystems, Department of Mechanical and Aerospace Engineering, Monash University, Clayton, VIC 3800, Australia

(Received 4 April 2014; accepted 7 July 2014; published online 24 July 2014)

We introduce a surface acoustic wave (SAW) based method for acoustically controlled concentration, capture, release, and sorting of particles in a microfluidic system. This method is power efficient by the nature of its design: the vertical direction of a traveling acoustic wave, in which the majority of the energy at the SAW-water interface is directed, is used to concentrate particles behind a microfabricated polydimethylsiloxane membrane extending partially into a channel. Sorting is also demonstrated with this concentration shown to be size-dependent. Low-power, miniature SAW devices, using methods such as the one demonstrated here, are well placed for future integration into point-of-care diagnostic systems. © *2014 AIP Publishing LLC*.
[http://dx.doi.org/10.1063/1.4891424]

The separation, concentration, and general manipulation of particles and cells are vital functions for many microfluidic systems, where particles serve as surrogates for cells and large biomolecules, but also as therapeutic or diagnostic agents in their own right. With the increasing complexity and digital nature of advanced microfluidic systems, gating functions that control particle and cell movement are becoming increasingly important. Strategies for controlled particle trapping and release include mechanical,[1,2] optical,[3,4] hydrodynamic,[5] magnetic,[6,7] and acoustic methods.[8–10] Acoustic forces are well suited to the task, being non-contact and applicable to a wide range of particle and cell sizes and types, though have not been used extensively for on-chip gating and valves. This is due to lack of suitable geometries, release strategies, fabrication difficulties, and small acoustic force gradients on the scale of a micron-sized particles, especially if lower frequencies ($\lesssim$5 MHz) with relatively large wavelengths ($\gtrsim$500 μm) are used. However, surface acoustic waves (SAWs), with typical wavelengths (4–300 μm) on the order of length scales of microfluidic systems, are well suited to biological assays where items on the scale of cells are manipulated.

To date, the vast majority of applications using SAW exploit the forces in the horizontal plane.[8,11–17] It may, however, be more sensible in some cases to take advantage of the force component in the vertical direction, considering that the major component of the traveling wave force is directed vertically. Due to the value of the Rayleigh angle θ_R, which describes the orientation of the acoustic force relative to the solid/fluid interface, the horizontal force is only a fraction of the vertical one. Despite this, there have been only select cases to date that explicitly utilize this as their mode of operation in closed microfluidic systems. The limiting factor in making use of the vertical force in closed systems, however, is a result of fabrication difficulties. Dentry *et al.*[18] used a 3D fabricated chamber to optimize the pumping force generated using SAW, with a pumping chamber angled at θ_R. In the future, though, 3D printed microfluidic devices will require further optimization and development to integrate with SAW devices to match the device quality and spatial resolution of conventional fabrication techniques.

In this work, we demonstrate the first explicit use of the vertical component of traveling SAW to trap and concentrate particles and release them on-demand. The proposed method makes use of a topographical polydimethylsiloxane (PDMS) feature easily constructed with standard microfabrication techniques and without the need for multilayer processes. By actively trapping and passively releasing particles, we show that it is possible to use this method to both control the timing of particle concentration and also filter them by size, all while making efficient use of the vertical orientation of an acoustic wave generated by SAW. Furthermore, the procedure used to fabricate this 3D structure in PDMS does not require gray-scale lithography, relying instead on the intrinsic changes in etch rates during deep reactive-ion etching (DRIE) when the movement of reactive ions is impeded in a high-aspect ratio feature. It is thought that this method for fabricating simple vertically varying features will find use in other applications where thin quasi-3D PDMS structures, including membranes, rods, and flaps, are required.

When an acoustic wave traveling through a fluid medium encounters an object with non-zero acoustic contrast, that object will be subjected to a time-averaged force.[19] For a particle in an acoustic field, this force is fundamentally due to the interference between the scattered field that it creates and the incident acoustic beam,[20,21] and is always oriented in the direction of the traveling wave acoustic beam.[22] In the case of a traveling substrate-bound wave, such as SAW, these surface displacements will couple into a fluid placed on top of the substrate, with the resulting beam propagating at the Rayleigh angle, given by $\theta_R = \sin^{-1}(c_f/c_s)$, where c_f and c_s are the sound speed in the fluid and the SAW velocity of the substrate. For water and lithium niobate (LN), a piezoelectric material commonly used for SAW applications, this angle is $\approx$22° from the vertical, with the relative magnitude of the vertical to the horizontal components given by

a)[redacted]

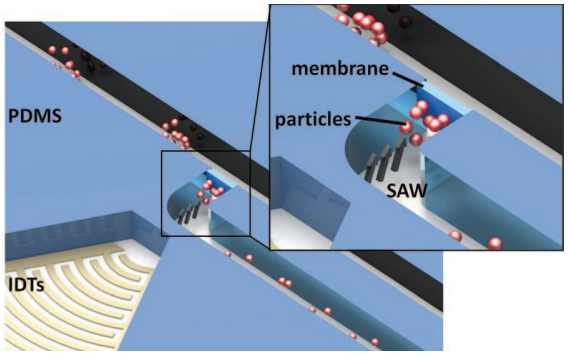

FIG. 1. Controlled release concept: a SAW generated by a series of focussed IDTs on a piezoelectric substrate generates an acoustic field that imparts a force, mostly in the vertical direction, against particles in a fluid flow. Without SAW applied, particles pass through the gap under the membrane unimpeded. However, subject to this force, particles are unable to pass beyond a microfabricated PDMS membrane in their path. This methodology enables on-demand particle concentration and release.

$\cos(22°)/\sin(22°)$; the vertical force is therefore approximately 2.5 times that of the horizontal one.

Figure 1 shows the system concept: a particle solution is injected perpendicular to a continuous flow channel in a T-junction configuration, with particle concentration and controlled release mediated by the application of SAW. Figure 2 shows this process in more detail, especially, with regard to the critical role of a PDMS membrane, which partially protrudes into the channel from which the particles originate. Provided the gap between the channel floor and the bottom of the membrane is sufficiently large, particles pass unimpeded in the direction of fluid flow. With the application of SAW, a traveling wave force is imparted on the particles in suspension, where after they are pushed both against the channel roof and the PDMS membrane.

The SAW device here consists of a circularly focussed 27 finger-pair, 30 μm wavelength (λ) set of 200 nm of aluminium on 7 nm chrome interdigital transducers (IDTs) spanning 25°, where the geometric focal point is 170 μm from the last finger pair, patterned on a 0.5 mm thick 128° *Y*–cut, *X*–propagating lithium niobate ($LiNbO_3$) substrate. The resonant frequency is given by $f = c_s/\lambda$, such that the displacement emanating from one set of finger pairs is reinforced on arrival at a subsequent pair. For $c_s = 3960$ m/s, this condition occurs at $f = 132$ MHz, producing a confined beam approximately 100 μm wide. The PDMS chamber was fabricated on a silicon mould etched using conventional Bosch process deep reactive ion etching (Oxford Instruments PLASMALAB100 ICP380, Abingdon, United Kingdom). The 2 μm thick feature used to produce the membrane results in less influx of etchant ions (SF_6), and therefore a slower etch rate. The result here is that, for a 40 μm deep etch elsewhere, the etch depth within the 2 μm gap is only $\approx$29 μm, yielding (after soft lithography) a PDMS channel with a height of 40 μm in most locations and a 11 μm gap where the 2 μm feature was patterned. To prevent particle adhesion, a 0.2% w/w solution of polyethylene glycol was flushed through the channels prior to use and used as the makeup volume for particle solutions. Demoulding from the silicon wafer was enhanced by finishing the etching process with a passivation step (C_4F_8) to yield a hydrophobic surface layer. The PDMS was then bonded directly to the SAW device (Harrick Plasma PDC-32G, Ithaca, NY, 1000 mTorr, 18 W), with the influx of polystyrene particles (Magsphere, Pasadena, CA, USA) and DI water modulated by a syringe pump (KDS100, KD Scientific, Holliston, MA, USA). The chamber directly above the IDTs is fully enclosed and air-filled to minimize amplitude attenuation.

Figure 3 shows the capture efficiency for different applied power levels and average flow velocities; higher applied power levels, and therefore larger acoustic pressure amplitudes, result in greater capture efficiency for a given flow rate. Once the SAW is turned off, the incoming particle flow is sufficient to dislodge the captured particles within a few hundred milliseconds. A significant advantage of utilizing both the primarily vertical orientation of the traveling acoustic field and a membrane impeding particle flow is the efficiency of this method; a particle need not be actively forced directly against the direction of particle flow, but in this case only pushed vertically by the distance between the channel floor and the base of the membrane and retained against the smaller local flow velocity. The result is that we are able to efficiently capture and concentrate smaller sized particles (which are acted on by a smaller acoustic force) at lower power levels compared to other SAW-based particle concentration work.[23] In the multimedia for Fig. 3, it is observed that particle motion in the meander region will seem to slow down with the application of SAW. While recent work has demonstrated that the application of SAW can potentially alter the local pressure conditions,[11] it is

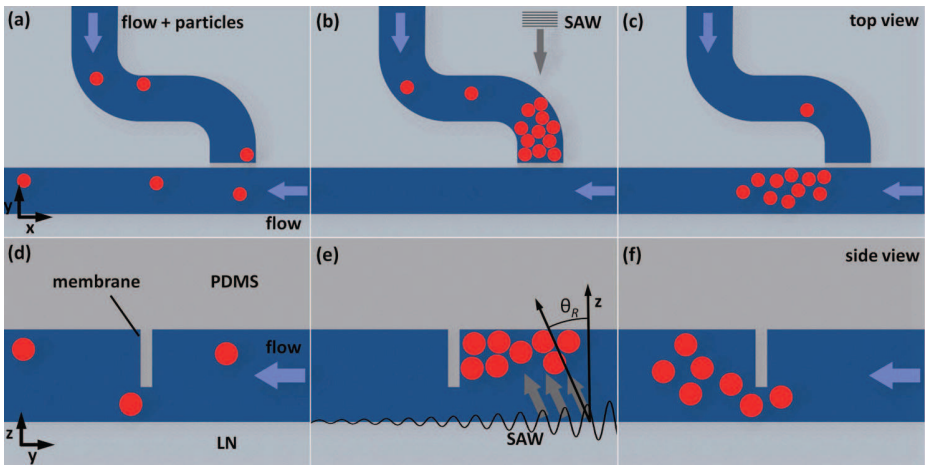

FIG. 2. Diagram of the active process for particle concentration and controlled release in a quasi-3D microfabricated PDMS channel on LN. Without SAW, ((a) and (d)) a continuous dilute stream of particles continues in the direction of fluid flow under the PDMS membrane. (b) and (e) With the application of a SAW generating an acoustic field oriented (primarily vertically) at the Rayleigh angle θ_R, particles are pushed vertically and remain trapped between the membrane and the chamber roof. (c) and (f) With the removal of this pressure source, the now concentrated particles are free to continue in the direction of the flow.

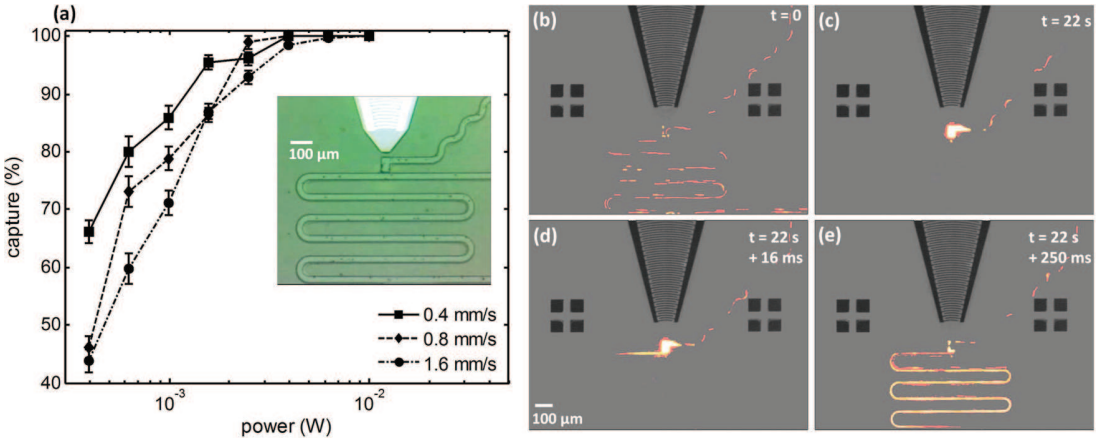

FIG. 3. Experimental results and images of particle concentration and release. (a) The capture efficiency is both power and flow velocity dependent, with lower flow rates and higher powers (with correspondingly higher substrate velocities) resulting in greater capture efficiency. The meander through which the particles flow (inset) is contrast-optimized to show the channel walls, as opposed to the fluorescent images in (b)–(e). (b) Dilute fluorescent 5 μm particles continue unimpeded through a microfluidic meander until the application of SAW. After an arbitrary amount of time, (c) here 22 s, SAW is turned off, leading to ((d) and (e)) near-complete release of the now concentrated particles within a few hundred milliseconds. Images (b)–(e) are with an applied power of 6.2 mW at a flow rate of 1.6 mm/s. Average flow velocities of 0.4 mm/s, 0.8 mm/s, and 1.6 mm/s correspond to flow rates of 0.5 nl/s, 1 nl/s, and 2 nl/s.(Multimedia view) [URL: http://dx.doi.org/10.1063/1.4891424.1]

thought that the change in particle velocity is a result of an acoustic field continuing to propagate into this region pushing particles toward channel edges, rather than as a result of altering fluid velocity. Indeed, the particle outside of this region does not visibly change with the application of SAW.

In the case of a traveling wave, the force applied to a given particle of radius R proportional to R^6 with larger particles therefore subject to a greater time-averaged force.[22] This principle can also be used here to filter and sort particles based on size. When a solution of different particle sizes is subject to the same flow and pressure amplitude conditions, larger particles are preferentially captured behind the PDMS membrane. This is demonstrated in Fig. 4, with 5 μm particles captured and filtered from smaller 2 μm particles. The sorting efficiency here is complete; with sufficient power 100% of the 5 μm are captured and 2 μm particles continuously flowing through the membrane gap. The sorting efficiency (in terms of the proportion of sizes separated) here is comparable to a dedicated traveling SAW separation method,[24] where the SAW is instead oriented orthogonally to the flow direction. However, as the separation ability here is supplementary to the main function of controlled capture and release, separation is limited to instances where, in a population of two distinct particle sizes, only one particle size is significantly influenced by the acoustic force field (with amplitude F_{aco}), while the other's motion is dominated by a viscous drag force F_D. In the case of a population of 2 μm and 5 μm particles, this condition is satisfied, where the 5 μm particles are subject to a F_{aco}/F_D two orders of magnitude greater than that of the 2 μm ones. However, where the particle sizes are more similar, as in the case of a 5/7 μm population, no effective sorting is observed. This is partly due to the varying local viscous drag in the vicinity of the membrane, which is almost zero in the corner near the channel ceiling and at a maximum near the gap between the membrane and the channel floor; a more efficient sorting mechanism would attempt to equalize the local fluid velocity as well as acoustic pressure amplitude experience by all particles as in Ref. 16. Sorting efficiency is also reduced as the particle size approaches that of the wavelength in the fluid ($\approx$11 μm at 132 MHz in water), where the acoustic force scaling is reduced (from R^6 to R^2).[22,25,26] In general, acoustic sorting efficiency is optimized by choosing a

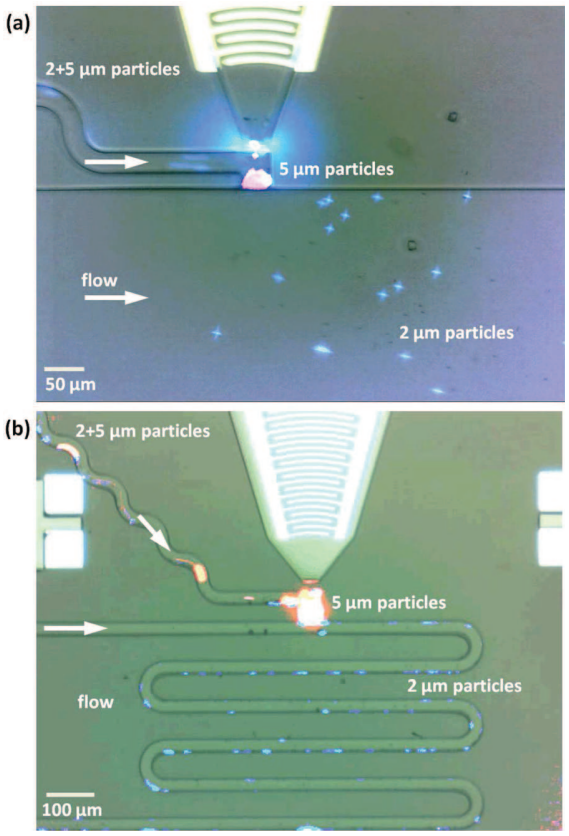

FIG. 4. Experimental images of particle filtering, here with 4 mW of applied power and a particle input flow rate of $\approx$1 mm/s, showing a superimposed optical fluorescent image of 5 μm (red) and 2 μm (blue) particles for both (a) a wide aspect ratio chamber and the same channel from Fig. 3. The larger particles, subject to a greater acoustic force, are wedged preferentially at the corner of the chamber roof and membrane, allowing the smaller 2 μm particles to pass under the membrane into the open chamber unimpeded.

sufficiently high frequency for a given particle population so the increase in force with frequency can be taken advantage of—recent work has demonstrated the significant deflection of 2 μm particles at higher frequencies, something that was not observed here[13]—but not so high that the resulting acoustic wavelength approaches the size of the particle and the differential acoustic force between particle sizes is reduced.

Here, we have demonstrated a SAW-based controlled capture and release mechanism with potential application to a range of microfluidic systems. The low power nature of this method, requiring only milliwatts—on the order of that used in portable RF communication devices—makes it readily applicable to handheld, point of care diagnostic devices. Furthermore, the scale of the SAW device demonstrated here, with an aperture of only 100 μm and totaling less than a millimeter in length, is of the small size needed to be integrated into these systems. Future work in SAW microfluidic lab-on-a-chip systems, moving from the conceptual and demonstration phase, will need to move increasingly in the direction of miniaturization such as that demonstrated here.

We gratefully acknowledge support received from the Australian Research Council, Grant No. DP 110104010. This work was performed in part at the Melbourne Centre for Nanofabrication (MCN) in the Victorian Node of the Australian National Fabrication Facility (ANFF).

[1]F. Beyeler, A. Neild, S. Oberti, D. J. Bell, Y. Sun, J. Dual, and B. J. Nelson, J. Microelectromech. Syst. **16**, 7 (2007).
[2]A. Neild, S. Oberti, F. Beyeler, J. Dual, and B. J. Nelson, J. Micromech. Microeng. **16**, 1562 (2006).
[3]A. H. Yang, S. D. Moore, B. S. Schmidt, M. Klug, M. Lipson, and D. Erickson, Nature **457**, 71 (2009).
[4]D. G. Grier, Nature **424**, 810 (2003).
[5]P. J. Lee, P. J. Hung, R. Shaw, L. Jan, and L. P. Lee, Appl. Phys. Lett. **86**, 223902 (2005).
[6]E. Mirowski, J. Moreland, S. Russek, M. Donahue, and K. Hsieh, J. Magn. Magn. Mater. **311**, 401 (2007).
[7]E. Mirowski, J. Moreland, A. Zhang, S. E. Russek, and M. J. Donahue, Appl. Phys. Lett. **86**, 243901 (2005).
[8]D. Collins, T. Alan, K. Helmerson, and A. Neild, Lab Chip **13**, 3225 (2013).
[9]P. Rogers and A. Neild, Lab Chip **11**, 3710 (2011).
[10]S. Oberti, D. Moeller, A. Neild, J. Dual, F. Beyeler, B. Nelson, and S. Gutmann, Ultrasonics **50**, 247 (2010).
[11]L. Schmid and T. Franke, Appl. Phys. Lett. **104**, 133501 (2014).
[12]J. Shi, H. Huang, Z. Stratton, Y. Huang, and T. J. Huang, Lab Chip **9**, 3354 (2009).
[13]V. Skowronek, R. W. Rambach, L. Schmid, K. Haase, and T. Franke, Anal. Chem. **85**, 9955 (2013).
[14]L. Schmid, D. A. Weitz, and T. Franke, "Sorting drops and cells with acoustics: acoustic microfluidic fluorescence-activated cell sorter," Lab Chip (published online).
[15]L. Johansson, J. Enlund, S. Johansson, I. Katardjiev, and V. Yantchev, Biomed. Microdevices **14**, 279 (2012).
[16]D. J. Collins, T. Alan, and A. Neild, Lab Chip **14**, 1595 (2014).
[17]O. Manor, L. Y. Yeo, and J. R. Friend, J. Fluid Mech. **707**, 482 (2012).
[18]M. B. Dentry, J. R. Friend, and L. Y. Yeo, Lab Chip **14**, 750 (2014).
[19]J. Rooney and W. Nyborg, Am. J. Phys. **40**, 1825 (1972).
[20]H. Bruus, Lab Chip **12**, 1014 (2012).
[21]D. Baresch, J.-L. Thomas, and R. Marchiano, J. Acoust. Soc. Am. **133**, 25 (2013).
[22]L. V. King, Proc. R. Soc. London, Ser. A **147**, 212 (1934).
[23]Y. Chen, S. Li, Y. Gu, P. Li, X. Ding, L. Wang, J. P. McCoy, S. J. Levine, and T. J. Huang, Lab Chip **14**, 924 (2014).
[24]G. Destgeer, K. H. Lee, J. H. Jung, A. Alazzam, and H. J. Sung, Lab Chip **13**, 4210 (2013).
[25]T. Hasegawa and K. Yosioka, J. Acoust. Soc. Am. **58**, 581 (1975).
[26]T. Hasegawa and K. Yosioka, J. Acoust. Soc. Am. **46**, 1139 (1969).

Chapter 7

Virtual deterministic lateral displacement

Chapter 7 presents a method for the sorting of particles with arbitrarily small differences in properties, including size. Particle and cell sorting is a required function in a wide range of pretreatment and on-chip analysis applications. The sensitivity and practicality of existing methods, however, falls short of requirements for many purposes. Here we demonstrate particle sorting with diameter differences of only 6%, which is a far smaller size difference than that realized previously using SAW. The acoustic field is modeled and the experimental results confirmed against this model. Additionally, it is shown to be possible to perform sorting using electrical forces on particles as well by altering some device parameters, with an electric field in the vicinity of the transducers also being produced.

7.1 Introduction

In Chapter 6 traveling SAW was used to capture and release particles on demand, where capture efficiency is dependent on particle size. Making use of this, it was possible to selectively capture larger 5 μm particles from a 5 μm and 2 μm particle mixture. This size difference of $\sim 150\%$ represents a substantial improvement in the size sensitivity reported from other SAW sorting methods ($\sim 300-400\%$) [202, 203], making this method suitable for many applications, such as filtering red blood cells from a solution of platelets. However, many other diagnostic applications require better size selectivity. For example, to detect circulating tumor cells (CTCs) for cancer screening, where these cells may only be a few microns larger than white blood cells [196], sensitivity

on the order of 10% or better is required, a step change in separation efficiency compared with what has been demonstrated previously. In the publication presented here, a new methodology has been developed for the deterministic sorting of particles and cells on a microfluidic chip. Here, an acoustic/electric field is oriented at an angle to the flow direction. From the perspective of sorting by particle size, the balance between the induced force on a particle and opposing drag resulting from fluid flow result in a critical diameter D_{crit}, above which larger acoustic or electric forces, both scaling with $F \sim R^3$, cause the particle to align with the force field, and below which particles continue in the direction of the flow. The acoustic and electric fields are both generated simultaneously, the acoustic field a result of the substrate vibrations produced by the IDTs on a lithium niobate substrate and the electric field produced in the fluid due to the alternating electric potential in the vicinity the IDTs themselves. Interestingly, the field that is relevant for sorting can be chosen by changing the chamber height; the electric force field is dominant in the near field though decays exponentially in the vertical direction, whereas the acoustic force does not decay significantly within a few wavelengths and is dominant in the far field. This is demonstrated through theoretical results, where the respective fields above the IDTs are mapped and compared. This is also shown experimentally, where particles larger than D_{crit} follow electric field nodes in a chamber that is 15 μm high and the the acoustic field in a chamber 45 μm high; this result is readily visible because the electric and acoustic fields are in direct opposition, being 90° out of phase from one another. Finally, the particle trajectories themselves are simulated in a 2D field and compared against experimentally observed displacements.

7.2 Publication

The following publication was reproduced from [215] by permission from The Royal Society of Chemistry.

Monash University

Declaration for Thesis Chapter 7

Declaration by candidate

In the case of Chapter 7, the nature and extent of my contribution to the work was the following:

Nature of contribution	Extent of contribution (%)
I was chief investigator for this work. I was responsible for device design iterations and fabrication, experimental design, experimental work, numerical and analytical work, post processing and interpretation of results and writing of the paper.	80

The following co-authors contributed to the work. If co-authors are students at Monash University, the extent of their contribution in percentage terms must be stated:

Name	Nature of contribution	Extent of contribution (%) for student co-authors only
Dr. Tuncay Alan	Overall supervision and review of drafts	
A/Prof. Adrian Neild	Overall supervision and review of drafts	

The undersigned hereby certify that the above declaration correctly reflects the nature and extent of the candidate's and co-authors' contributions to this work.

Candidate's Signature	[redacted]	**Date:** 7/5/14
Signature 1	[redacted]	**Date:** 7/5/14
Signature 2	[redacted]	**Date:** 7/5/14

Lab on a Chip

PAPER

View Article Online
View Journal | View Issue

Particle separation using virtual deterministic lateral displacement (vDLD)†

Cite this: *Lab Chip*, 2014, **14**, 1595

David J. Collins, Tuncay Alan and Adrian Neild*

Received 10th December 2013,
Accepted 27th February 2014

DOI: 10.1039/c3lc51367j

www.rsc.org/loc

We present a method for sensitive and tunable particle sorting that we term virtual deterministic lateral displacement (vDLD). The vDLD system is composed of a set of interdigital transducers (IDTs) within a microfluidic chamber that produce a force field at an angle to the flow direction. Particles above a critical diameter, a function of the force induced by viscous drag and the force field, are displaced laterally along the minimum force potential lines, while smaller particles continue in the direction of the fluid flow without substantial perturbations. We demonstrate the effective separation of particles in a continuous-flow system with size sensitivity comparable or better than other previously reported microfluidic separation techniques. Separation of 5.0 μm from 6.6 μm, 6.6 μm from 7.0 μm and 300 nm from 500 nm particles are all achieved using the same device architecture. With the high sensitivity and flexibility vDLD affords we expect to find application in a wide variety of microfluidic platforms.

1. Introduction

The separation of particles and cells is fundamental to a variety of chemical, biological and industrial processes,[1,2] where the concentration of a particular analyte is used to increase diagnostic detection efficiency or therapeutic efficacy. Compared to conventional techniques, microfluidic systems can perform particle separation with less reagent, time and cost while taking advantage of forces that may be inapplicable on the macro-scales. Typically separation is enabled by the application of an external field, with efficiency determined by the differential effect the field has on particles with different properties. Microfluidic particle separation in continuous flow systems has been demonstrated using hydrodynamic,[3–5] magnetic,[6,7] optical,[8] dielectrophoretic (DEP),[9–11] acoustic,[12,13] microfabricated electrophoretic arrays[14–16] and passive mechanical methods, including brownian ratchets[17,18] and deterministic lateral displacement (DLD),[19–23] with each of these techniques having different advantages and operating ranges in terms of allowable sizes, sample types and throughput.

A DLD system consists of a microfluidic channel containing a periodic array of pillars such that each subsequent row is offset in the lateral direction. This broken symmetry results in multiple streamlines that co-exist within the channel. Particles with a diameter smaller than a critical value travel with the forward flow, while larger particles are "bumped" sideways.[20,25] In addition to their sensitivity, DLD devices have the additional advantage of being a passive system without pre-treatment requirements. However, as separation depends on the geometric distribution of the pillars, individual devices must be fabricated to suit specific particle size ranges. Similarly, any structural irregularities affect the flow profile (due to the number of pillars there is a large number of sites for potential defects), possibly resulting in stiction and blockages. Moreover, relatively long channel lengths are required to achieve significant lateral displacement.

Here we address these issues by replacing the DLD pillar array with virtual obstacles, combining the principles of DLD with the flexibility of modifiable acoustic and DEP forces. Both acoustic and electric fields act differentially on particles and cells placed within them according to their size and mechanical or electrical properties, translating particles with impressive rapidity.[26]

Using acoustic forces it is possible to sort based on stiffness and density, with certain particles migrating to pressure antinodes and others to the pressure nodes,[13] and is in this sense a deterministic method, though this is only possible in the case where two particle populations have opposite-signed acoustic contrast factors. However, in sorting based on particle size, the fundamental principle of acoustic methods that have been shown to date is based on the size-dependant speed of particle migration in a uniformly applied field; hence sorting is a temporal rather than deterministic effect.

Destgeer *et al.* recently demonstrated a particle separation device using traveling surface acoustic waves (SAW);[27] SAW is an acoustic actuation method that is especially applicable to

Laboratory for Micro Systems, Department of Mechanical and Aerospace Engineering, Monash University, Clayton, VIC 3800, Australia.

† Electronic supplementary information (ESI) available: Video of particle separation (video 1). See DOI: 10.1039/c3lc51367j

microfluidic systems with the ability to easily localize and direct acoustic energy with wavelengths on the order of microfluidic systems (5–300 μm). Here, SAW was used to create a traveling wave acoustic field whose interfacial force scales with particle radius with $F_{tw} \sim R^6$. Alternatively, particle separation can be performed using standing waves, with $F_{sw} \sim R^3$; when an acoustic field is generated in a half wavelength standing wave resonating channel it is possible to move particles from antinodal to nodal positions,[12] though this design is limited in its separation sensitivity due to the short distance ($1/4\lambda$) over which particles are separated. In both cases the particle size differences reported are limited to ~300%, despite the impressive acoustic force scalings. It has not been possible to sort particles deterministically – with particles above or below some critical diameter moving in different directions – in systems where these force scalings are simply applied directly.

Sorting is also possible using DEP, imparting a differential force on particles and cells based on their size and electrical properties. Park *et al.* used an array of electrodes patterned on a glass slide at an angle to the flow direction to sort particle sand cells, separating 1 μm from 10 μm particles and *E. coli* from whole blood.[10] The separation demonstrated here was not deterministic, however, which would require a sharp cutoff between particles with only fractionally different properties, sending particles with particular values in a specific direction without significantly affecting the trajectory of other particles, rather than sorting particles on the basis of a parameter gradient.

To improve on the capabilities of microfluidics for particle separation, we have developed a novel SAW-based dynamically tunable particle sorting method with excellent separation efficiencies. This method makes use of acoustic forces or DEP, where the predominance of either force is determined by the channel dimensions. Particle separation in vDLD is *deterministic* in that particles above a critical size will be sorted from smaller ones, and *virtual* in that the acoustic/electric field – the fundamental equivalent of pillars in a DLD array – is non-material and can be adjusted to suit a given size range. Because the separation of particles for given sizes is determined only by the frequency, voltage/pressure amplitude and flow rate, it is possible to separate particles over a wide size range, from nanometers to micrometers. Importantly, the ability to choose the dominant force permits sorting based on different particle/cell properties; acoustic forces permit sorting based on mechanical properties (compressibility, density), while DEP allows sorting based on electrical properties (permittivity).

The virtual deterministic lateral displacement (vDLD) system employs high frequency SAW and is depicted in Fig. 1. This method is not inherently limited to any particle size range. Importantly, we show that separation with only fractional differences in particle sizes is possible, with the effective separation of 5.0 μm/6.6 μm, 6.6 μm/7.0 μm and 300 nm/500 nm particles, all using the same device. Additionally, we show that this sorting is possible using two distinct forces with the force relevant for sorting dictated by the channel dimensions.

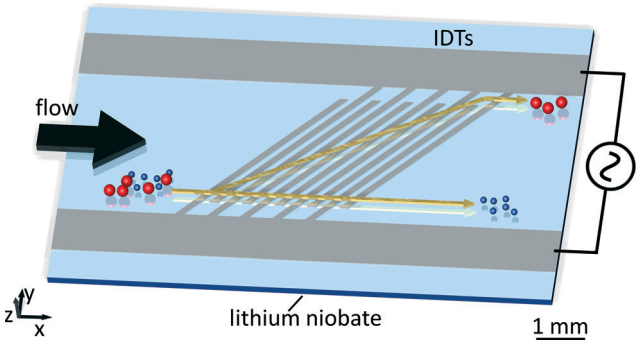

Fig. 1 Sketch of the vDLD operating principle: a solution containing dissimilarly sized particles passes through an acoustic or electric field, created by an array of interdigital transducers (IDTs) on a piezoelectric lithium niobate (LN) substrate. Particles in the vDLD system are subject to both induced forces and viscous drag. Larger particles are captured in the force field and are transported laterally, while smaller particles are not significantly shifted.

System principles

The vDLD system is comprised of a microfluidic channel aligned on top of a high-frequency SAW device, composed of a series of aluminium interdigital transducers (IDTs) arrayed on a piezoelectric lithium niobate (LN) substrate. When an A/C signal is applied across the IDTs at a resonant frequency $f = c_s/\lambda_{SAW}$, where c_s is the sound speed in the substrate and λ_{SAW} is the spacing between successive IDT finger-pairs, the surface displacements emanating from a finger-pair are reinforced by those of nearby finger-pairs. As a result both an acoustic and an electrical field are created in the vicinity of IDTs, as seen in Fig. 2, either of which can be used for sorting. Moreover, both can be used for *deterministic* sorting; in the case of the size parameter, as long as there exists some critical diameter D_{crit} above which particles are trapped in a force field and below which they are not, it is possible to have a sharp cutoff in the lateral displacement of particle sizes. Here we discuss these forces, acoustic and dielectrophoretic, followed by how each determines D_{crit}.

A particle immersed in a standing wave pressure field experiences a maximum time averaged force given by[12]

$$F_{aco}^{max} = -\left(\frac{\pi P^2 V_p \beta_f}{2\lambda}\right)\phi, \quad (1)$$

where

$$\phi = \frac{5\rho_p - 2\rho_f}{2\rho_p + \rho_f} - \frac{\beta_p}{\beta_f}, \quad (2)$$

V_p is the particle volume, λ is the wavelength, ρ_f and ρ_p the density of the fluid and particles, μ the viscosity, β_p and β_f are the compressibility of the particle and medium and P is the acoustic pressure amplitude. In the case of a finite number of finger-pairs, the pressure amplitude varies across the length of the IDT finger-pairs (Fig. 3(a, c)).

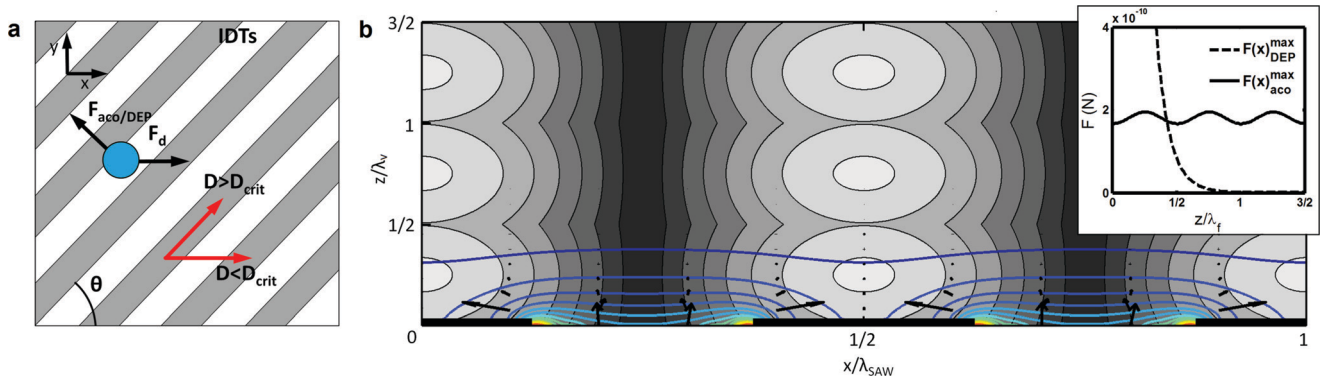

Fig. 2 (a) A particle in the vDLD system is subject to forces of viscous drag F_D, the acoustic force F_{aco} and/or the DEP force F_{DEP}. The predominant force, DEP or acoustic, acting on a particle is determined by its distance above the IDTs. (b) Shows the acoustic pressure field magnitude in gray, the first 10 DEP force potential contours in color and the linearly scaled DEP force vectors in relation to the position of the IDTs (black). For representative values of voltage and pressures (~5 V, ~100 kPa) that are generated on a piezoelectric such as lithium niobate at frequencies on the order of 10's of MHz on polystyrene particles in water, the maximum acoustic force in the *x*-direction $F(x)^{max}_{aco}$ is dominant for heights greater than approximately half of the vertical acoustic wavelength in the fluid λ_v (inset). The DEP force contours were derived from the method in Morgan *et al.*, 2001.[24]

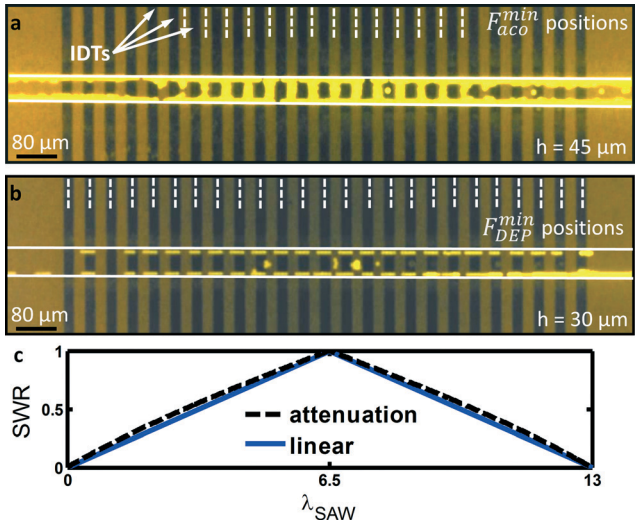

Fig. 3 The height of the microfluidic chamber will determine which force, F_{DEP} or F_{aco}, predominates. (a) The acoustic field is the dominant force above the transducers for larger channel heights, with particle (here with a diameter of 6.6 μm) accumulation at the acoustic nodal positions between the IDTs. (b) Lowering the chamber height increases the horizontal component of the DEP force that can act on the particles, with particles observed to align directly above the transducers, and reduces the relative influence of the acoustic force as evidenced by the smaller number of acoustic nodes that contain particles. Particles are pushed to the edge of the channel due to the acoustic force maximum in the channel center – PDMS at the channel edges attenuates the surface displacements driving the acoustic force – and the flow condition through the channel (0.5 μl min^{-1}). (c) In an acoustic field generated by a finite number of transducers the standing wave ratio (SWR) will vary across the length of the IDTs, modeled as the summation of acoustic displacements from neighboring finger pairs, shown here including and excluding the attenuation of a SAW under water (here with a decay length of 9.24 λ_{SAW} (ref. 28)).

As a by-product of exciting the acoustic field, an electrical field between the IDTs finger pairs is produced as well, though this field is not explicitly required for sorting. A particle immersed in this electrical field will be subject to a time-averaged dielectrophoretic (DEP) force determined by that particles frequency-dependent polarisability relative to the medium, given by

$$F_{DEP} = 2\pi\varepsilon_m R^3 \mathrm{Re}(K)\nabla|E_{rms}|^2, \quad (3)$$

where ε_m is the permittivity of the media, K is the Clausius–Mossotti factor dependent on the relative permittivity of the particle and media, varying between −0.5 and 1, and E_{rms} is the root-mean-square electric field.[29] The acoustic and DEP force fields have been modeled and are shown in their relation to the interdigital transducers and how they evolve vertically from the substrate surface in Fig. 2. Generally speaking, DEP is only relevant in the vicinity of the electrodes, with the force magnitude dropping off exponentially from the substrate surface. In the direction that is relevant to sorting – the *x*-direction – the acoustic force is dominant for $h \lesssim 1/2\lambda_v$ (Fig. 2b). Each force will locate particles to different positions in the vDLD array. For a negative Re(K) value, particles will be vertically repelled and shifted horizontally to locations directly above the IDTs, as shown in Fig. 3b. In contrast, acoustic forces will shift particles to locations of minimum pressure, located between transducers, shown in Fig. 3a. Because DEP pushes particles with a negative Re(K) vertically, the height of the chamber therefore determines which force will be useful for sorting. Regardless of which force this is, the same fundamental behavior is expected because the force in both cases scales with $F \sim R^3$ and its periodic variation with the IDTs. A particle under the influence of either of these forces is also subject to a viscous drag force F_D, given by

$$F_D = -6\pi\mu R u, \quad (4)$$

where μ is the fluid viscosity, R is the particle radius, u is the differential velocity between particle and fluid and $F^{max}_D = -6\pi\mu R v_f$

represents the maximum drag possible, where u is replaced by the fluid velocity v_f. Here, particle separation occurs because of the different scaling of acoustic/DEP and drag forces, with $F_{aco/DEP} \sim R^3$ and $F_D \sim R$. The ability of a particle to pass through an acoustic/DEP force field will be determined by the maximum of each of these forces that are generated, as shown in Fig. 2a (a cross section in the x–y plane).

In the case of the acoustic force, equating eqn (1) and (4) where $u = v_f$, we find the critical particle diameter D_{crit}^{aco} at which the maximum acoustic force will equal the maximum drag force; a particle traveling orthogonally to an acoustic field in a continuous flow with dimensions larger than D_{crit}^{aco} will be trapped at any node/antinode, depending on the acoustic contrast factor ϕ. For most particles and cells, however, ϕ is positive, resulting in particle migration to acoustic nodes. Accounting for an acoustic field at an angle θ to the flow field, D_{crit}^{aco} is found to be

$$D_{crit}^{aco} = 2\cos^2(\theta)\sqrt{\frac{9\mu\lambda v_f}{\pi\beta_f P^2\phi}}. \quad (5)$$

Similarly, the critical diameter for a particle immersed in a DEP force field can be found be equating eqn (3) and (4), with

$$D_{crit}^{DEP} = 2\cos^2(\theta)\sqrt{\frac{-3\mu v_f}{\varepsilon_m \mathrm{Re}(K)\nabla |E_{rms}|^2}}, \quad (6)$$

valid for negative values of Re(K).

Here, θ is chosen based on qualitative design and performance considerations. A large θ will displace particles by large lateral distances, but will have a larger D_{crit} than a small θ value, which conversely will be able to sort smaller particles, though with less lateral displacement.

The presence of a critical diameter, above which particles become trapped and below which they do not, is the basis for deterministic sorting, with trapped particles exiting the force field at a different location to non-trapped particles. However, this will only occur when the particles all experience a similar v_f value. Though the IDTS are oriented in the x–y plane, the field that is generated varies vertically as well;[30] for this we examine the pressure and velocity field in the x–z plane. Two chamber heights were tested experimentally: one with $h = 1/2\lambda_v$ and a second with $h = 3/2\lambda_v$, where λ_v is the vertical component of the standing wave in the fluid. In the case of a chamber with a height such that the DEP force dominates ($h = 1/2\lambda_v$), this is readily realized in that particles will be repelled to the chamber roof. However, in the case where acoustic force determines the particle trajectory, the particles will follow paths where they experience minimal acoustic forces. For example, with a chamber height $h = 3/2\lambda_v$, this occurs at $h = \lambda_v$; the finite size of particles means that the acoustic force will be greater at the chamber roof, and a repellant DEP force prevents particles taking a path across the IDTs at $h = 1/2\lambda_v$. These effects have been observed experimentally: randomly distributed particles immersed in a horizontal flow will slow down as they are pushed into slower-moving flow at the chamber roof when $h = 1/2\lambda_v$, and can be seen to (on average) speed up when $h = 3/2\lambda_v$ as they are pushed into faster moving flow in near the middle of the parabolic flow profile in the z-direction.

Any chamber with height $h \lesssim 3/2\lambda_v$ will result in all particles of the same diameter experiencing the same local forces. Acoustic nodes/antinodes will still be formed for larger chamber heights, however this would reduce the possibility for reliable deterministic displacement due to multiple possible particle trajectories in the z-direction, each with a unique v_f, F_D^{max} and $F_{aco/DEP}^{max}$.

With the criteria established with regard to the height dimensions, attention can be returned to the x–y plane, as this is the plane in which sorting occurs. Fig. 4 and 5 show the deterministic sorting of micro and nano-scale particles, respectively; particles with diameters $D < D_{crit}$ (blue) are able to proceed with minimal lateral displacement, albeit more slowly than the fluid velocity. In contrast, particles above a critical diameter D_{crit}, occurring when the particle velocity that is induced by the acoustic/DEP force is greater than that of the local fluid velocity, will not be able to pass across a force maximum. It is important to note that the local fluid velocity v_f will vary in the y-direction due to the fully developed laminar flow profile. At the start of the chamber (left), with this condition not being met, the larger particles cross from one IDT pair to the next, though are still slightly retarded and laterally shifted. By designing the device such that the particles are introduced into the center of a channel with buffer fluid making up the volume on either side, each lateral displacement in the resulting parabolic velocity field moves the particles into slower flowing fluid so that the acoustic force becomes increasingly dominant, corresponding to increasing lateral shifts. Eventually the fluid flow is reduced such that $F_{aco/DEP}^{max} \geq F_D$; for optimum sorting this condition should occur at the last possible acoustic pressure antinode or DEP force maximum. In the case of an acoustically generated force and a finite set of IDTs, it should be noted that this antinode will occur near the middle of the IDT array (see Fig. 3).

Critical to acoustic deterministic sorting is the ability to control the topographical amplitude of the acoustic field, namely to maintain a relatively constant surface displacement across the with of the IDT aperture. By acting on particles as they pass over the IDTs themselves, in contrast to systems where the IDTs generate an acoustic field outside of the fluid-covered region,[31,32] the amplitude variance across the aperture width that occurs in far field SAW can be avoided,[33,34] while simultaneously eliminating what would otherwise be the significant SAW amplitude attenuation at the LN–PDMS interface.[35]

Methods

The vDLD device here consists of a 13 finger pair 80 μm wavelength set of 5/250 nm chrome/aluminium IDTs arrayed on a 0.5 mm thick, double side polished 128° Y-cut,

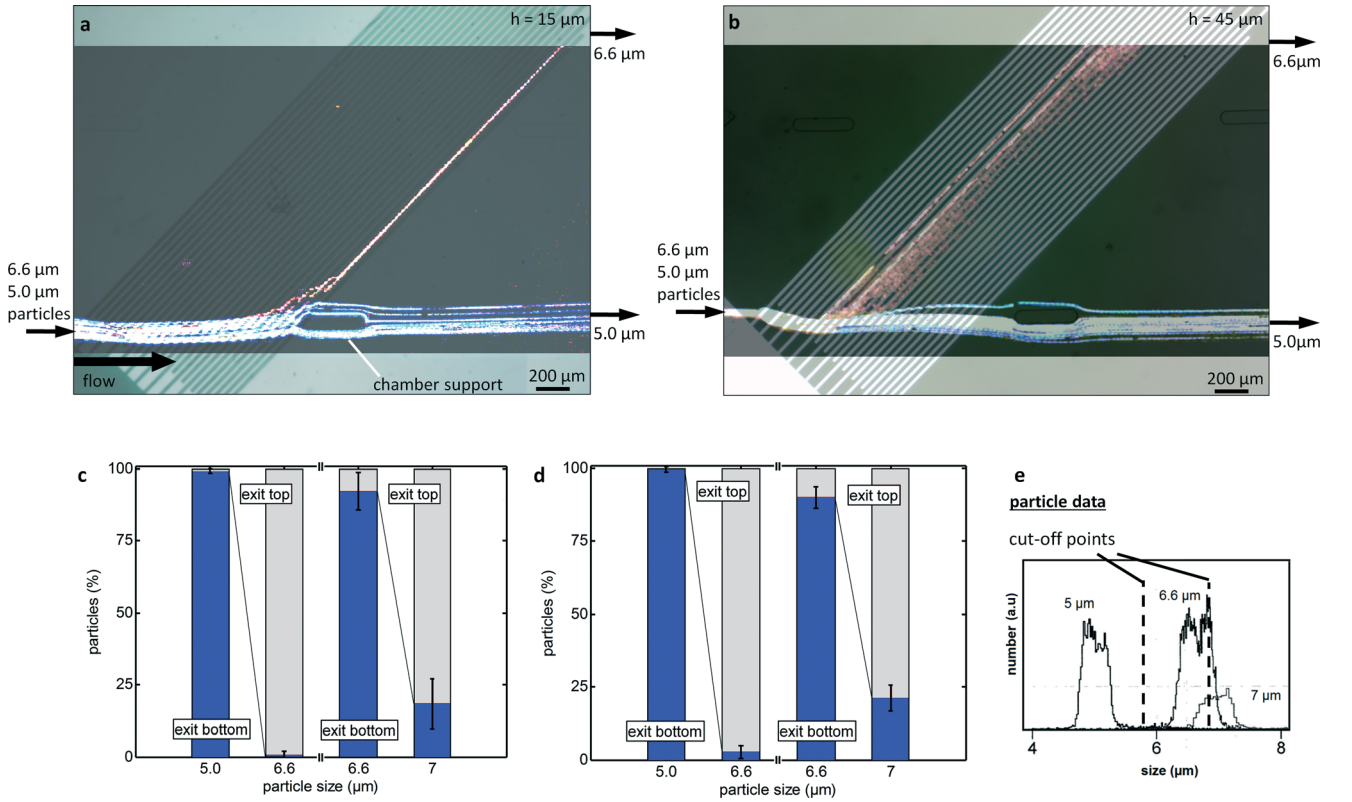

Fig. 4 vDLD particle sorting is possible in devices where either DEP or acoustic forces determine particle trajectory, with captured particles translating on top of the IDTs in the case of DEP and between them in the case of the acoustic force. (a) Maximum intensity plot of fluorescent particles overlaid on a brightfield image of a device with height h = 15 μm and peak-to-peak voltage of 4 V, where a solution of blue 5.0 μm orange 6.6 μm particles passes through a truncated vDLD array with 13 finger-pairs, angled at $\phi \approx 45°$ to the flow direction, with particles of diameters $D > D_{crit}$ being laterally separated from particles with $D < D_{crit}$. The same is shown for a device in which acoustic forces are expected to dominate in (b), with h = 45 μm and applied power of 0.0781 W mm^{-2}, as evidenced by the capture of particles along acoustic nodes in the region of the IDTs where the acoustic force is at a maximum (see Fig. 3). The effectiveness of both forces for particle separation is evidenced by their comparable sorting efficiencies. (c, d) Shows the respective separation efficiencies of two particle population sets ([5.0 μm, 6.6 μm] and [6.6 μm, 7.0 μm]) for devices where h = 15 μm (c) and h = 45 μm (d). Separation efficiency of the particle populations is limited by the existing overlap in their size distributions, given in (e), obtained from the particle manufacturer (Magsphere Inc, Pasadena, CA). Flow rates in both cases are 4.1 μl min^{-1} with a SAW wavelength of 80 μm.

X-propagating LN substrate operating at 49 MHz. To insulate the transducers, prevent corrosion and promote adhesion with the polydimethlsiloxane (PDMS) chamber, the SAW device was coated with 200 nm of SiO_2. The PDMS (1 : 5 ratio of curing agent/polymer) chamber, with height 15 μm or 45 μm, was bonded with the device after exposure to an air plasma (Harrick Plasma PDC-32G, Ithaca, NY, 1000 mTorr, 18 W). Polystyrene particles (Magsphere, Pasadena, CA, USA) enter the laterally symmetric 5 mm wide chamber through a 20 μm particle injection port. Due to the high aspect ratio (up to 300 : 1), 200 μm wide chamber supports were periodically spaced to prevent collapse and maintain chamber height. The buffer solution consisted of deionized water (Miili-Q 18.2 MΩ cm, Millipore, Billerica, MA) with 0.2% polyethylene glycol to prevent particle adhesion. Experiments were visualized using a fluorescent microscope (Olympus BX43, Tokyo, Japan) and imaged using a 5MP C-mount camera (Dino-Lite AM7023CT, New Taipaei City, Taiwan). In order to demonstrate system versatility, all experiments were performed using the same device. The pressure amplitude was determined by $P = v_s pc_f$, where v_s is the substrate velocity, determined using a laser Doppler vibrometer (LDV, UHF-120; Polytech GmBH, Waldbronn, Germany).

Results and discussion

Fig. 4 shows the sorting of 5.0 μm and 6.6 μm particles (green and orange in ESI† video 1), which enter the vDLD array at the middle of the chamber. In both In Fig. 4(a, b), the applied voltage/power and flow rate have been specifically tuned to place the larger 6.6 μm particles in the last few possible force minima for most effective sorting. As discussed previously and shown in Fig. 3, this is located near the middle of the IDT array for the case where the acoustic pressure determines the particle trajectory (h = 45 μm) and at the end of the array when DEP is dominant (h = 15 μm). During the experiment the particles were counted individually, with 99.1 ± 0.7% and 99.3 ± 1.3% of each particle size range successfully separated in the DEP-dominant case, and 99.5 ± 0.5% and 97.3 ± 2.7% in the acoustically-dominant one, where

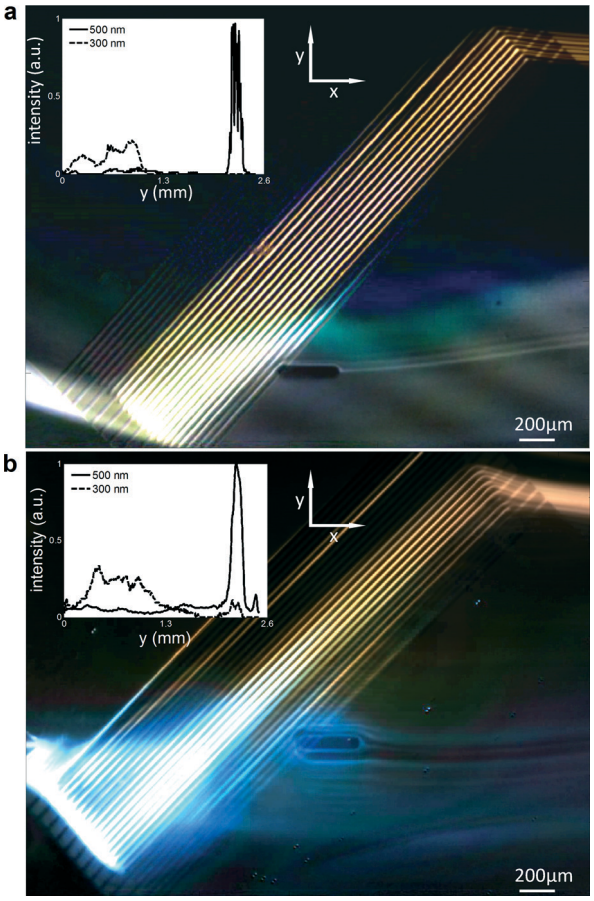

Fig. 5 (a, b) Shows average intensity images with separation of fluorescent blue 300 nm and 500 nm orange (σ_{300} = 39 nm, σ_{500} = 16 nm) particles passing through a vDLD device with (a) h = 15 μm [3.8 V, 0.45 μl min^{-1}, λ_{SAW} = 80 μm] and (b) h = 45 μm [0.369 W mm^{-2}, 1.8 μl min^{-1}, λ_{SAW} = 80 μm]. 500 nm particles are observed to travel at an angle to the flow in the direction dictated by the force field. 300 nm particles subjected to the same force field experience a smaller induced force, with their trajectory determined instead by viscous drag. Insets show intensity plots of fluorescent particles with background subtracted; approximately 87% [in (a)] and 79% [in (b)] of 500 nm particles, as measured by the integral of the intensity profiles, are separated from the 300 nm particles.

larger 6.6 μm particles exit the pressure field separated by the vertical span of the IDTs. Particle separation efficiency is marginally reduced to 80–90% when sorting between 6.6 μm and 7.0 μm particles (less than 6% size difference). However, for both of the particle size ranges separated in Fig. 4 the quantity of unsorted particles, *i.e.* those observed to follow an unintended trajectory, is on the same order of the value of overlap in the particle size distribution (Fig. 4e). Increasing voltage/SAW-amplitude or decreasing flow velocity would cause the larger particles to follow a pressure node encountered earlier, decreasing the sensitivity of the device to the particular size range tested here.

A major advantage of the vDLD system is that particles over a large size range can be similarly separated, requiring only a change of flow rate and amplitude. Using the same devices used to separate micron-sized particles in Fig. 4, we demonstrate the separation of sub-micron particles, showing the viable separation of 300 nm and 500 nm particles (blue and orange, respectively) in Fig. 5. Here, separation efficiency in Fig. 5 (insets) is determined by the normalized image intensity of the final ten rows of pixels in the x-direction, rather than particle counting, as the particles could not be visualized individually. The separation of these small particles is made possible by the relatively high frequency used to do so. For a given frequency of actuation, there exists a particle size below which acoustic streaming, rather than though acoustic pressure field, dictates particle motion. This diameter is given by $d_c = \delta\sqrt{6\Psi/\phi}$, where Ψ is a geometry dependent factor (0.375 for a standing wave in a flat-walled chamber), ϕ is the acoustic contrast factor from eqn (2) and $\delta = \sqrt{2\mu/\rho\omega}$, the acoustic boundary layer thickness.[36] At a frequency of 50 MHz, for example, it should be theoretically possible to capture particles as small as 200 nm in an acoustic standing wave in water.

To better understand the parameters (velocity, pressure and diameter) that determine particle displacement, the vDLD system was modeled. To avoid duplication, the force field is modeled here as being acoustically generated. The analysis presented here, however, could easily be extended to a DEP-dominated particle trajectory.

The particle velocity **u** is determined by the contributions resulting from the acoustic field, $u_{F_{aco}}$, and that of the parabolic fluid velocity field v_f, given by

$$\mathbf{u} = \nabla(u_{F_{aco}^{max}} k(x\cos(\theta) + y\sin(\theta))) + v_f(y), \quad (7)$$

where $u_{F_{aco}^{max}}$ is the maximum migration velocity that can be induced by the acoustic field alone, $k = 2\pi/f$ is the wave number, (x, y) denotes the horizontal and vertical spatial coordinates, and

$$u_{F_{aco}^{max}} = \frac{F_{aco}^{max}}{6\pi\mu R}, \quad (8)$$

with v_f determined by

$$v_f = v_f^{max}(1 - y^2/y^{max}). \quad (9)$$

This velocity field was simulated using the MATLAB function *streamline*, with simulated particles subject to various flow rates and pressures. Fig. 6a shows the relationship between D_{crit} and pressure amplitude. As per eqn (5), $D_{crit}^{aco} \sim v_f^{0.5}/P$, with lower fluid velocities yielding a smaller D_{crit}^{aco}. With multiple IDT pairs, however, it is possible to displace particles of a given size for higher maximum flow rates more than would be suggested by Fig. 6a. Each successive antinode will shift a given particle laterally, where each shift moves the particle into a lower local fluid velocity in a parabolic laminar flow profile. Fig. 6b shows that, provided the spatial extent of the pressure field is sufficiently large, multiple flow rates will lead to eventual particle capture when a particle is sufficiently laterally shifted such

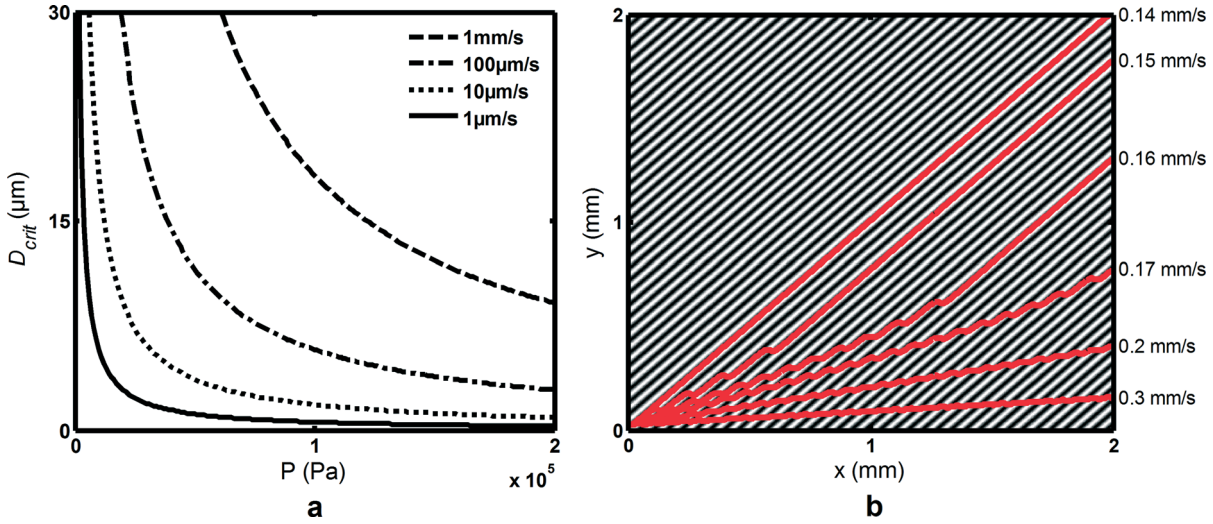

Fig. 6 The critical particle diameter D_{crit} for a given acoustic antinode is a function of the local fluid velocity and pressure amplitude. (a) Shows the relationship between D_{crit} and pressure amplitude for various realizable microfluidic flow rates when the acoustic field is angled at 45° to the fluid flow. Here, different values for pressure amplitude and flow velocity were inserted into eqn (5). The existence of multiple IDT pairs spanning a laterally oriented parabolic velocity field in the vDLD system, however, means that higher flow rates can be used than might be inferred from (a). In (b), a polystyrene 10 μm particle in a 49 MHz 100 kPa pressure field will eventually be trapped in an acoustic node, regardless of the flow rate, provided the acoustic field is sufficiently elongated horizontally. Flow velocity is at a maximum at the site of particle injection, parabolically decreasing with increasing lateral distance.

that $F_{aco}^{max} \geq F_D$ locally. Here, maximum flow velocities v_f^{max}0.17 mm s^{-1} result in particle capture within 2 mm for the pressure conditions given. Similarly, a particle of any size will eventually be captured in an acoustic node in such a field for given flow velocity and pressure amplitude conditions, allowing particles to be sorted in a definable gradation. This modeling approach is validated by comparing the simulation results with experimental results in a continuous acoustic field. Fig. 7a shows the influence a relatively small change in applied power density (with pressure amplitude $P = v_s pc_f$) will have on lateral displacement. This is also observed experimentally in Fig. 7b, with sharp increases in 6.6 μm particle displacement for power densities ≳0.03 W mm^{-2}. In both cases the acoustic field was modeled here as being locally uniform; if the number of IDTs creating the acoustic field is sufficiently large, the attenuation of SAW under water means that the field strength will vary by less than 0.05% in the central half of a field created by 216 finger pairs.

For more *deterministic* sorting, however, with greater lateral separation between particles on either side of a given diameter, it is practical to limit the number of finger pairs used. In doing so, the final acoustic antinode encountered determines the D_{crit}^{aco} of the system, with the previous finger pairs serving to shift larger particles into increasingly slower flow. In the case where the acoustic force varies across the length of the IDTs (as in Fig. 4b), this will occur in the region where the acoustic force is at a maximum.

The separation enhancing effect that multiple acoustic nodes affords can be theoretically described as follows; as the particles pass through the pressure field they are displaced laterally in two ways. (1) A small shift each time an acoustic force maxima is crossed and (2) a larger shift across the width of the field when a particle is trapped in an acoustic node, when $F_{aco}^{max} \geq F_D^{max}$. The latter is critical for sorting, but the former also aids the process. If we combine the scaling of the drag and acoustic force and examine the ratio between them, we find that $\widetilde{F} \equiv F_{aco}/F_D \sim R^2/v$. If we then define the ratio between two different particle size populations $\alpha = R_{small}/R_{large}$ and the ratio of the fluid velocities that each particle population will experience at a given point in the x-direction, $\beta = v_{small}/v_{large}$, then it follows that

$$\frac{\widetilde{F}_{large}}{\widetilde{F}_{small}} \sim \frac{\beta}{\alpha^2}. \quad (10)$$

The larger this ratio, between the force on the larger and smaller particle populations, the better sorting will be. As expected, the relative force experienced between two different particle sizes scales with the square of ratio of the difference in particle sizes. Due to the lateral deflection occurring at each acoustic force maxima, β increases with the number of IDT finger pairs, enhancing the separation effect. This aids sorting due to small variation in the forces experienced by an individual particle due to interparticle forces, the effect of nearby particles on the acoustic field and Brownian motion. The effect of different β could be further optimized in future iterations of the vDLD device by increasing the velocity profile gradient. The role of multiple acoustic force maxima becomes essential for submicron particles which experience a high degree of Brownian motion.

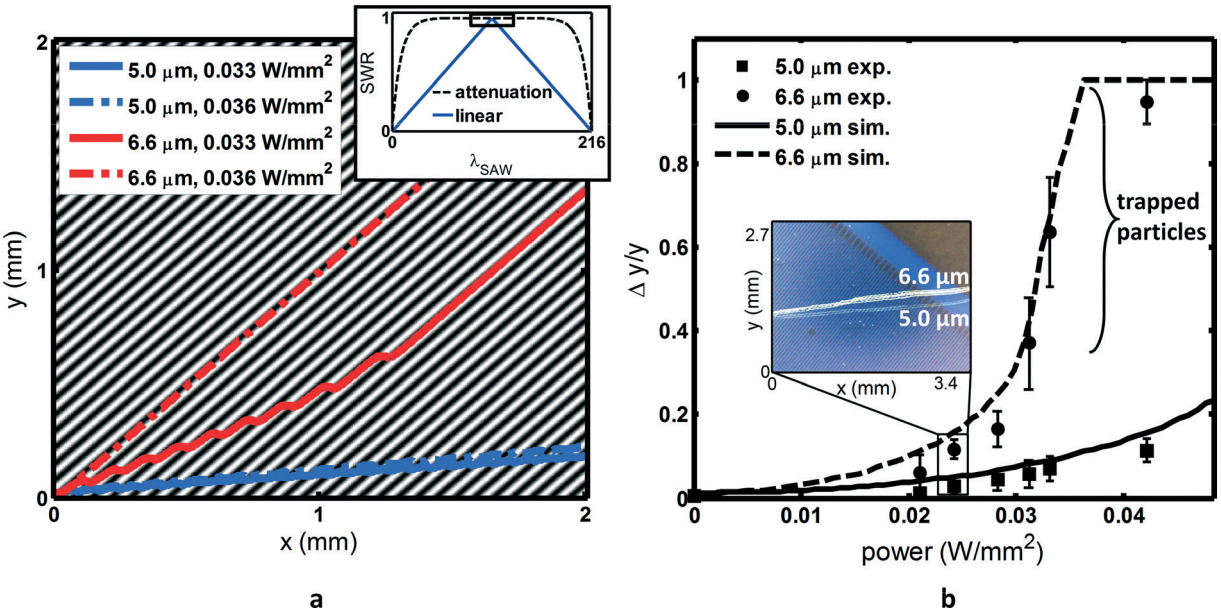

Fig. 7 In a continuous force field the lateral displacement is a function of particle size and applied power. (a) Shows the particle path traced through an acoustic force field for different particle sizes and energy densities. When a particle is close in size to D_{crit}, even a small change in parameters can have a large influence in that particles lateral displacement. A large enough number of IDTs yields a spatially uniform acoustic field (inset), as simulated here. (b) In a separate set of experiments, 5.0 μm and 6.6 μm particles were introduced into a continuous acoustic field [a λ_{SAW} = 100 μm, 39 MHz device with 216 finger pairs, $h \approx 50$ μm] with the same flow conditions (4.1 μl s^{-1}, v_f^{max} = 0.35 mm s^{-1}) as simulated in (a) and compared against these simulation results, with the inset showing representative maximum intensity images of 5.0 μm (green) and 6.6 μm (orange) particles across the continuous IDT array. Higher powers yield larger separation distances. The pressure field is determined by $P = v_s \rho c_f$, where the substrate velocity v_s was measured using a laser doppler vibrometer. For 6.6 μm particles, displacement plateaus for power densities greater than approximately 0.035 W mm^{-2}, though these particles are essentially trapped in an acoustic node by the end of the test area for power densities approximately greater than 0.03 W mm^{-2}. Here error bars show the spatial extent of observed particles and experimental points show the midpoint of this observed displacement.

The advantages of having a finite number of pressure antinodes produced by IDT finger pairs placed directly in the channel are a result of practical, as well as theoretical considerations. By integrating the IDTs directly in the path of particle migration the pressure field can be strictly defined within the boundaries of the chamber, avoiding attenuation losses compared to the case where the IDTs are placed outside of the chamber. Additional finger pairs, in addition to permitting sorting at greater maximum flow velocities for a given pressure amplitude (Fig. 6b), practically also result in larger substrate velocities, and therefore pressures, for a given A/C signal.

Conclusions

We have developed a deterministic sorting system that can be applied to a wide variety of particle/cell sizes. Placing IDT finger-pairs directly in the channel maximizes the acoustic force that is experienced by the particles and allows sorting based on either acoustic or DEP forces, with the dominant force being simply determined by choosing the channel height. Though the higher channel dimensions of the acoustic-dominant vDLD has advantages from a throughput and ease of fabrication standpoint, the system is versatile as a result. It is possible to sort based on essentially any particle/cell parameter by choosing the dominant force; the acoustic force for mechanical properties and the DEP force for electrical properties.

More generally, SAW devices are uniquely applicable to microfluidic particle separation because: (1) they are planar and can be easily integrated with other microfluidic processes, (2) the wavelength of a typical SAW device (5–300 μm) is of the same order of most microfluidic systems and (3) the localization of energy at the surface results in efficient transfer of energy to a fluid placed on top, and have therefore found application in microfluidic applications as diverse as atomization,[37,38] mixing,[39] concentration,[40] pumping,[41] droplet production[42] and microcentrifugation.[43]

Here we have presented a further utilization, vDLD, which takes advantage of the high frequencies and corresponding length scales associated with SAW. With the ability to separate particle populations of arbitrary dimensions, we expect the vDLD system to be applied to any field or application where deterministic separation of particles or cells by their physical properties is required.

Acknowledgements

Principle fabrication of the vDLD devices was performed at the Melbourne Center for Nanofabrication (MCN), the Victorian node of the Australian National Fabrication Facility (ANFF).

References

1 E. Riera-Franco de Sarabia, J. A. Gallego-Juárez, G. Rodríguez-Corral, L. Elvira-Segura and I. González-Gómez, *Ultrasonics*, 2000, **38**, 642.
2 P. Tartaj, M. del Puerto Morales, S. Veintemillas-Verdaguer, T. González-Carreno and C. J. Serna, *J. Phys. D: Appl. Phys.*, 2003, **36**, R182.
3 J. C. Giddings, F. J. Yang and M. N. Myers, *Anal. Biochem.*, 1977, **81**, 395.
4 D. Di Carlo, *Lab Chip*, 2009, **9**, 3038.
5 M. Yamada and M. Seki, *Lab Chip*, 2005, **5**, 1233.
6 Y. Wang, Y. Zhao and S. K. Cho, *J. Micromech. Microeng.*, 2007, **17**, 2148.
7 N. Xia, T. P. Hunt, B. T. Mayers, E. Alsberg, G. M. Whitesides, R. M. Westervelt and D. E. Ingber, *Biomed. Microdevices*, 2006, **8**, 299.
8 M. MacDonald, G. Spalding and K. Dholakia, *et al.*, *Nature*, 2003, **426**, 421.
9 P. R. Gascoyne and J. Vykoukal, *Electrophoresis*, 2002, **23**, 1973.
10 S. Park, Y. Zhang, T.-H. Wang and S. Yang, *Lab Chip*, 2011, **11**, 2893.
11 M. Wiklund, C. Günther, R. Lemor, M. Jäger, G. Fuhr and H. M. Hertz, *Lab Chip*, 2006, **6**, 1537.
12 J. Shi, H. Huang, Z. Stratton, Y. Huang and T. J. Huang, *Lab Chip*, 2009, **9**, 3354.
13 F. Petersson, A. Nilsson, C. Holm, H. Jönsson and T. Laurell, *Lab Chip*, 2005, **5**, 20.
14 C.-F. Chou, R. H. Austin, O. Bakajin, J. O. Tegenfeldt, J. A. Castelino, S. S. Chan, E. C. Cox, H. Craighead, N. Darnton and T. Duke, *et al.*, *Electrophoresis*, 2000, **21**, 81.
15 L. R. Huang, P. Silberzan, J. O. Tegenfeldt, E. C. Cox, J. C. Sturm, R. H. Austin and H. Craighead, *Phys. Rev. Lett.*, 2002, **89**, 178301.
16 S. L. Levy and H. G. Craighead, *Chem. Soc. Rev.*, 2010, **39**, 1133.
17 L. R. Huang, E. C. Cox, R. H. Austin and J. C. Sturm, *Anal. Chem.*, 2003, **75**, 6963.
18 J. Han, J. Fu and R. B. Schoch, *Lab Chip*, 2007, **8**, 23.
19 K. J. Morton, K. Loutherback, D. W. Inglis, O. K. Tsui, J. C. Sturm, S. Y. Chou and R. H. Austin, *Proc. Natl. Acad. Sci. U. S. A.*, 2008, **105**, 7434.
20 L. R. Huang, E. C. Cox, R. H. Austin and J. C. Sturm, *Science*, 2004, **304**, 987.
21 D. W. Inglis, J. A. Davis, R. H. Austin and J. C. Sturm, *Lab Chip*, 2006, **6**, 655.
22 J. A. Davis, D. W. Inglis, K. J. Morton, D. A. Lawrence, L. R. Huang, S. Y. Chou, J. C. Sturm and R. H. Austin, *Proc. Natl. Acad. Sci. U. S. A.*, 2006, **103**, 14779.
23 K. Loutherback, K. S. Chou, J. Newman, J. Puchalla, R. H. Austin and J. C. Sturm, *Microfluid. Nanofluid.*, 2010, **9**, 1143.
24 H. Morgan, A. G. Izquierdo, D. Bakewell, N. G. Green and A. Ramos, *J. Phys. D: Appl. Phys.*, 2001, **34**, 1553.
25 C.-F. Chou, O. Bakajin, S. W. Turner, T. A. Duke, S. S. Chan, E. C. Cox, H. G. Craighead and R. H. Austin, *Proc. Natl. Acad. Sci. U. S. A.*, 1999, **96**, 13762.
26 L. Y. Yeo and J. R. Friend, *Biomicrofluidics*, 2009, **3**, 012002.
27 G. Destgeer, K. H. Lee, J. H. Jung, A. Alazzam and H. J. Sung, *Lab Chip*, 2013, **13**, 4210.
28 S. Shiokawa, Y. Matsui and T. Ueda, in *Ultrasonics Symposium IEEE Proceedings*, 1989, **1**, 643.
29 P. Tathireddy, Y.-H. Choi and M. Skliar, *J. Electrost.*, 2008, **66**, 609.
30 Y. Chen, A. A. Nawaz, Y. Zhao, P.-H. Huang, J. P. McCoy, S. J. Levine, L. Wang and T. J. Huang, *Lab Chip*, 2014, **14**, 916.
31 Y. Chen, S. Li, Y. Gu, P. Li, X. Ding, L. Wang, J. P. McCoy, S. J. Levine and T. J. Huang, *Lab Chip*, 2014, **14**, 924.
32 Y. Chen, X. Ding, S.-C. Steven Lin, S. Yang, P.-H. Huang, N. Nama, Y. Zhao, A. A. Nawaz, F. Guo and W. Wang, *et al.*, *ACS Nano*, 2013, **7**, 3306.
33 R. Tucoulou, M. Brunel, D. V. Roshchupkin, I. A. Schelokov, J. Colin and J. Grilhe, *Ultrasonics IEEE Transactions on Ferroelectrics and Frequency Control*, 1999, **46**, 856.
34 A. Holm, P. Wallner, W. Ruile and R. Weigel, in *Ultrasonics Symposium IEEE Proceedings*, 1997, **1**, 153.
35 S. M. Langelier, L. Y. Yeo and J. Friend, *Lab Chip*, 2012, **12**, 2970.
36 H. Bruus, *Lab Chip*, 2012, **12**, 1014.
37 D. Collins, O. Manor, A. Winkler, H. Schmidt, J. Friend and L. Yeo, *Phys. Rev. E: Stat., Nonlinear, Soft Matter Phys.*, 2012, **86**, 056312.
38 J. Ju, Y. Yamagata, H. Ohmori and T. Higuchi, *Sens. Actuators, A*, 2008, **147**, 570.
39 R. Shilton, M. Tan, L. Yeo and J. Friend, *J. Appl. Phys.*, 2008, **104**, 014910.
40 J. Shi, X. Mao, D. Ahmed, A. Colletti and T. Huang, *Lab Chip*, 2008, **8**, 221.
41 M. Tan, L. Yeo and J. Friend, *Europhys. Lett.*, 2009, **87**, 47003.
42 D. Collins, T. Alan, K. Helmerson and A. Neild, *Lab Chip*, 2013, **13**, 3225.
43 N. R. Glass, R. J. Shilton, P. P. Chan, J. R. Friend and L. Y. Yeo, *Small*, 2012, **8**, 1881.

Chapter 8

Conclusions

In this final chapter the key findings and contributions of the work in this thesis are summarized. Following this a discussion of ongoing and possible future work is presented.

8.1 Contributions

In this thesis we have developed new systems for the on-chip manipulation of droplets, cells and particles and created experimentally confirmed analytical models that describe these systems, a useful and necessary step for their wider understanding and implementation. These abilities were made possible by the unique applicability of SAW to microfluidic systems, exerting a range of different forces that can be selected for in system design. In the following paragraphs the primary contributions of this thesis are summarized.

Chapter 4 describes the physical mechanisms that determine droplet size in the phenomena of SAW atomization, where micron-scale droplets are continually produced during high-frequency mechanical excitation of a liquid thin film. The droplet size was found to be a function of a length-scale adjusted acoustic weber number and the applied frequency, with $D \sim We^{2/3} f^{-}1$. Further, the thin film from which this atomization occurs was described and characterized for the first time, including with regard to its height, observed to result from the minimum energy conditions with acoustic reflection off a partially reflecting interface.

Chapter 5 presents a new method for the on-demand production of microfluidic water-in-oil

droplets. By focussing acoustic energy at a stable water-oil interface, an acoustic pressure is produced that moves this interface into a moving continuous phase, resulting in pinch-off and droplet formation. Droplet production is controllable, with greater powers (and therefore larger pressures) and longer pulse durations leading to the production of larger and more droplets, where the size of these droplets was found to match well existing models for two-phase systems in the squeezing regime of droplet formation. Additionally, it was shown that it is possible to pre-concentrate and encapsulate particles within these droplets simultaneously with droplet formation.

Chapter 6 demonstrates the use of a novel method for the on-demand concentration, release and sorting of particles in a microfluidic system using low-power SAW. Focussing a high-frequency acoustic beam at an orthogonally oriented membrane protruding partially into a channel through which particles flow, these particles are forced vertically against the chamber roof and prevented from continuing due to the membrane. By using a physical obstruction, rather than the acoustic force alone, it is possible to perform particle concentration and release with very low applied powers. This physical feature was easily fabricated, made possible without any alterations to the fabrication process. Additionally, because the force on particles is size dependent, it was shown that it is possible to sort particles based on size, with larger particles filtered.

Chapter 7 presented a method for the deterministic sorting of particles based on their physical properties. Here, we demonstrated sorting based on size, with larger particles sorted from smaller ones based on arbitrarily small differences in size. In the first ever instance of this, an investigation of the forces directly above a set of IDTs was performed, where it was found that either the dielectrophoretic (DEP) or acoustic force field will determine particle trajectories. Either force can be made use of for particle sorting through the selection of the channel height, with DEP dominant in the near-field and acoustic forces dominant in the far-field.

SAW is a useful and growing method for the on-chip manipulation of cells, particles and droplets. Possible barriers to implementation in point-of-care applications include lack of technology transfer between research and industry and the investment required in the development of suitable

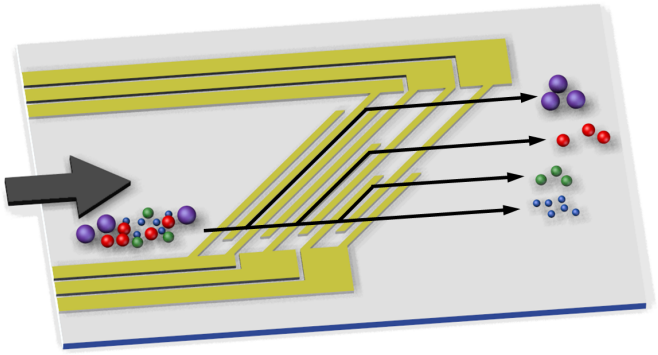

Figure 8.1: With multiple independent vDLD channels it is possible to sort multiple particle or cell populations simultaneously by making use of arbitrarily small differences in parameters, including size, electrical permittivity and stiffness.

portable electronics, similar to that demonstrated for miniature nebulization therapy [35]. However, the advantages the SAW confers are too substantial for these issues to pose too large a problem in the long term, especially given the easy integration of SAW in multi-function microfluidic devices, tunable and powerful effects on particles and cells, efficient energy transfer, ability to localize acoustic field and appropriate range of producible wavelengths. SAW techniques will eventually find widespread use in lab-on-a-chip systems.

8.2 Continuing and future work

The research into the microfluidic manipulation of microfluidic species presented in this thesis presents many opportunities for further investigation. A few of these opportunities are presented here.

In Chapter 7 we demonstrated the fractionation of different particle populations based on arbitrarily small differences in size. This ability is useful for a wide range of applications, though there are many cases where it may be desirable to sort multiple particle/cell/droplet species; for example, the simultaneous separation of white blood cells, red blood cells, platelets and plasma for subsequent blood component analysis. Building on the advances made in Chapter 7, it should be possible to modify this design to perform multichannel sorting by truncating different regions of an IDT array. In fact, devices have been constructed explicitly for this purpose, with frequencies in the range of 50–200 MHz, in principle allowing the simultaneous sorting of 4 separate particle populations anywhere in the range of 100 nm–20 μm on the same device. This can be accomplished with a single A/C signal for all sorting channels through the use of in-line attenuators. By

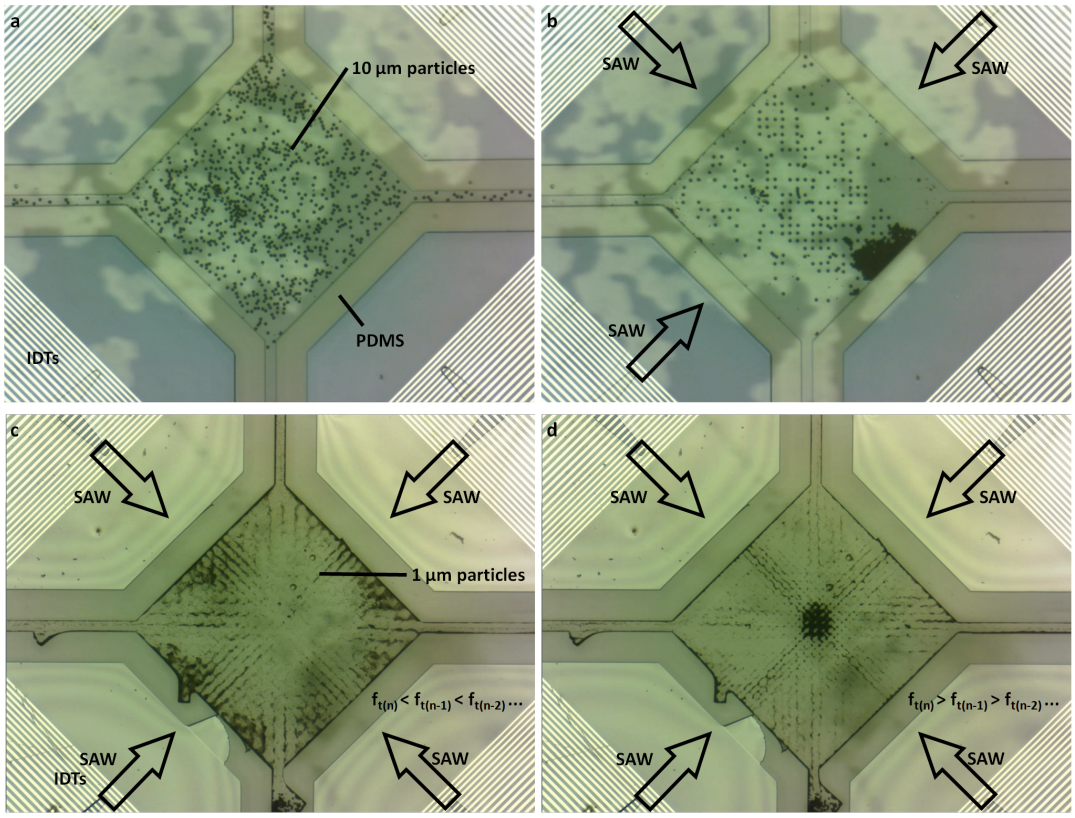

Figure 8.2: Using a 2D acoustic field it is is possible to create an array of particles, with only one particle per acoustic node (a,b). Using a partial traveling wave in one direction, excess particles are swept in the direction of the traveling wave. Bulk manipulation of particles is made possible through periodic frequency sweeps, with (c) decreasing and (d) increasing frequencies leading to dispersal and concentration, respectively.

adjusting each attenuator (effectively a resistor) appropriately, each sorting channel can be tuned so that it has its own characteristic critical diameter, with increasing standing wave pressure (or DEP force) in each addressable set of IDTs yielding a smaller and smaller critical diameter. A diagram of the multichannel vDLD concept is shown in Fig. 8.1, where the SAW/electrical field is periodically truncated laterally by appropriate patterning of IDTs.

Possible further work also includes applying the vDLD system for biological applications. Besides the aforementioned component sorting of whole blood, diagnostic uses of the vDLD concept include the detection of diseased circulating cells with different physical properties than other blood cells. For example, a cell infected with the *plasmodium falciparum* parasite, which causes malaria, results in blood cells that are an order of magnitude stiffer than normal red blood cells [216, 217, 218]. Similarly, the detection of circulating tumor cells (CTCs), which tend to be slightly larger than white blood cells [196], is currently developing as a potentially useful diagnostic screening tool. Applying the vDLD system, where these cells can be sorted in a deterministic

fashion, should result in higher separation efficiencies and therefore greater detection sensitivity than other microfluidic separation techniques.

Future work also includes the trapping of particles and cells in 2D arrays using SAW for single cell analysis. While 2D trapping has been demonstrated before [219, 101], the particle size has always been substantially smaller than the acoustic wavelength, meaning that it is impossible to reliably control the number of particles in a given acoustic node. By using higher frequencies such that a half-wavelength approaches the size of the particles in a 2D acoustic field, it is possible to restrict the number of particles in a given node to one. Using a resulting 2D array of individual cells single cell analysis, where the development and/or response of an individual cell is assessed based on its individual epigenetic markers, can be reliably and usefully performed. By retaining these cells in a static array against a periodic flow, it is also possible to assess the response of individual cells to different reagents. Additionally, the uses of this general platform, where a 2D acoustic field is generated by opposing sets of IDTs, has not been fully explored. For example, through the use of chirped IDTs (described in Section 2.3) combined with periodic frequency sweeping it is possible to either disperse or concentrate particles in a 2D array; sweeping the frequencies from high to low moves particles away from the chamber centre, with the converse concentrating particles. Both functions, where particles are trapped in a 2D array and dispersed/concentrated, are shown in Fig. 8.2. This system is currently being optimized and characterized.

1.65

Appendix A

Conference paper

The conference paper 'ON-DEMAND PICOLITER-SCALE DROPLET GENERATION USING SURFACE ACOUSTIC WAVES' was presented at the 17th International Conference on Miniaturized Systems for Chemistry and Life Sciences ("μTAS") in Freiburg, Germany on October 27–31, 2013. This paper, largely simplifying the material in Chapter 5 (showing alternative image processing), is presented on the following page.

ON-DEMAND PICOLITER-SCALE DROPLET GENERATION USING SURFACE ACOUSTIC WAVES

David J. Collins[1], Tuncay Alan[1], Kristian Helmerson[2] and Adrian Neild[1*]

[1] Laboratory for Micro Systems, Department of Mechanical and Aerospace engineering, Monash University, Clayton, VIC, AUSTRALIA and

[2]School of Physics, Monash University, Clayton, VIC, AUSTRALIA

ABSTRACT

Droplets are a versatile platform for performing chemical reactions, detection and compartmentalization. When a droplet is in a two-phase device droplet-based processes can be performed without the need for fluid handling, with small reaction volumes reducing the need to perform separate mixing steps and reducing reaction times. While techniques exist to produce continuous trains of water-in-oil droplets, it has been difficult to produce individual droplets on-demand, a prerequisite for more complex programmable microfluidic devices. Here we present a novel method for integrating a pressure source on-chip, producing picoliter scale water-in-oil droplets on-demand using surface acoustic waves.

KEYWORDS: Microfluidics, droplet, acoustic, surface acoustic waves

INTRODUCTION

The production of microfluidic droplets is fundamental for reliable droplet-based chemical reactions. The production of these droplets has been predominantly in T-junctions [1] and flow-focusing systems [2], where a continuous fluid flow of two immiscible fluids (most often oil and water) is required, with a constant stream of monodisperse droplets resulting from the combination of these two fluid streams. Technologies used to drive these flows, most often peristaltic pumps or syringe pumps, are poorly suited to manipulation of fluid volumes in the sub-nanoliter range, making on-demand production of individual droplets difficult to control. Further, in most microfluidic devices the pressure source is located distances away that are orders of magnitude greater that the length scales of the device, introducing time delays, additional fluid volumes and additional pressure gradients and resistances proportional to the length of the connecting tubing.

To address these shortcomings, several methods have been used to create pressure gradients on-chip, including surface acoustic waves (SAW). SAW is readily applicable to droplet generation, given the ability for a SAW to act directly on a fluid-fluid interface [3] with the wavelength of a typical SAW device (5 μm < λ_{SAW} < 300 μm) encompassing the range of length scales found in most microfluidic devices. SAW has been used previously for mixing, concentration [4], pumping [5], jetting [6] and atomization [7], where (in the last two cases) SAW was used to act on the fluid-air interface to produce droplets with diameters as small as a few micrometers.

A SAW is produced using a series of interdigital transducers (IDTs) arrayed on a piezoelectric substrate and driven at a frequency $f = c_s/\lambda_{SAW}$, where c_s is the sound velocity in the piezoelectric substrate, resulting in a Rayleigh wave which will travel on the surface unattenuated. A SAW is substantially different from other methods of piezoelectric actuation, with bulk of the displacement concentrated within a few wavelengths from the substrate surface, resulting in efficient energy transfer from the substrate to a fluid placed on top of it, with the angle at which the acoustic wave propagates into the fluid given by the Rayleigh angle, $\theta_R = \sin^{-1}(c_l/c_s)$.

In this paper we report a novel method to produce individual picoliter-scale droplets on-demand, using focused SAW to act upon a water-oil interface to eject water droplets into a continuous oil phase. Further, we elucidate the mechanism by which a Rayleigh SAW acts upon a water-oil interface in order to produce movement in the direction of SAW propagation.

THEORY

Acoustic radiation pressure, the time-averaged pressure on an interface placed in the path of an acoustic beam, arises as the result of the nonlinear propagation of the acoustic wave across a material discontinuity. In the case of an acoustic beam produced using SAW acting on an oil-water interface (as in Fig. 1b), there is no method, aside from interface movement, to transfer the isotropic pressure induced by the SAW to the oil side of the interface. The Rayleigh pressure acting on an interface is then given by [3]

$$p_r = \langle p - p_0 \rangle + \langle \rho v^2 \rangle, \tag{1}$$

where v is the instantaneous fluid particle velocity and $\langle \rho v^2 \rangle$ is simply $\langle E \rangle$, the energy density in the fluid. To a first order approximation the fluid particle velocity $v \approx v_0$, where $v_0 = \zeta\omega$ is the substrate velocity, ζ is the surface displacement and ω is the angular frequency. If the substrate velocity is oscillating sinusoidally, the time average $\langle \rho v^2 \rangle$ is nonzero, resulting in a nonzero pressure term for an interface in the path of the acoustic beam. The static pressure term $\langle p\text{-}p_0 \rangle$ arises from the nonlinear propagation of the acoustic beam through the fluid itself. Both the static and interfacial pressure contribute to the production of droplets in the system presented in Fig. 1.

EXPERIMENTAL

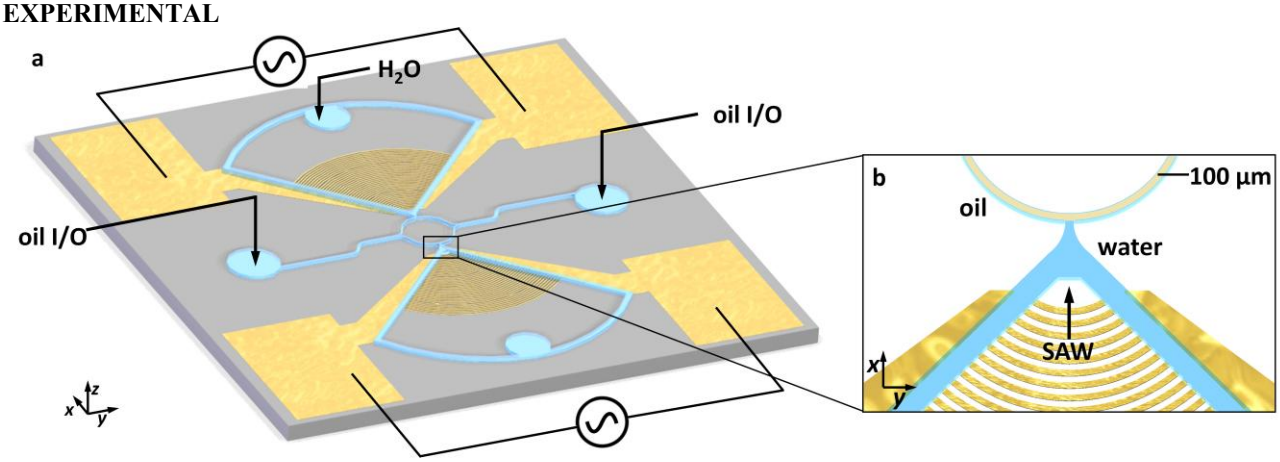

Figure 1: (a) Diagram of the SAW-based picoliter-scale droplet production system. A continuous and constant fluid phase of oil is injected in either symmetric oil I/O port. (b) Applying a short-duration SAW pulse (on the order on 100ms) focused at the water-oil interface is used to produce a single picoliter-scale water-in-oil droplet on-demand. The preferred SAW propagation direction is in the x-direction, as per the coordinate systems in (a) and (b). Figure is adapted from [8].

We employed 40 µm/80 µm wavelength focused SAW devices, comprising 90/45 finger-pairs of 90˚ circular focused interdigital transducers (FIDTs) on a 0.5 mm thick, single side polished 128˚ *Y*-cut, *X*-propagating lithium niobate (LN) substrate. The 10 nm chrome/200 nm aluminium FIDTs were aligned on the substrate symmetrically with respect to the preferred propagation direction on the LN. With the exception of the electrode pads, the devices were further coated with 70 nm of evaporation-deposited SiO_2 to promote adhesion with polydimethylsiloxane (PDMS), which was bonded after exposure to an activated air plasma. In the device setups considered the PDMS (~ 2 mm height) was either bonded directly to the IDTs (as in Fig 1) or delineated a water filled chamber around the IDTs (Figs. 2,3). Results from the two systems are comparable, though marginally higher powers are required to produce comparable droplets in the first case due to PDMS-loaded SAW attenuation.

Olive oil was injected into the using a syringe pump (KD Scientific 210, Holliston, MA, USA) whereas water (Milli-Q 18.2 MΩ.cm, Millipore, Billerica, MA) was manually manipulated using a 1 mL syringe until a steady-state oil-water interface was achieved. A signal generator/amplifier (BelektroniG F10, Freital, Germany) was used to power the device.

RESULTS AND DISCUSSION

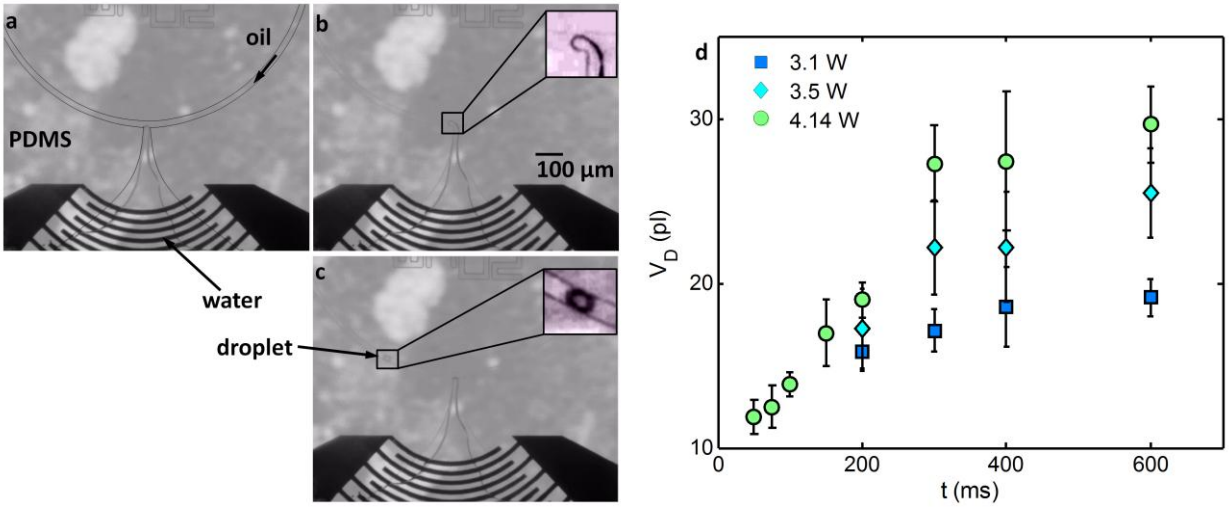

Figure 2: (a-c) Images of the production of an individual droplet and (d) the droplet volume V_D for different pulse durations and applied powers. The insets in (a-c) are contrast-enhanced for clarity. The orifice and channel width for (a-d) are 20 µm and 30 µm, respectively, both with a 30 µm chamber height, with a SAW wavelength of 80 µm and frequency of 48.4 MHz. The PDMS boundaries are highlighted in (a) for clarity. (d) Is adapted from [8].

In this work a focused SAW pulse is directed at an oil-water interface in a modified T-junction, where oil is the continuous and water is the disperse (droplet) phase. When the fluid interface is deformed sufficiently to bring the leading edge of the interface into contact with the opposing wall of the T-junction, the non-uniform pressure gradient on either

side of the nascent droplet resulting from the continuous fluid flow causes the neck at the orifice boundary to thin and finally break off, resulting in a water-in-oil droplet embedded in the oil phase [1]. Fig. 2a-c shows the interface movement and droplet break-off processes, with Fig 2d showing the observed droplet volumes, here encompassing a range of ~10-30 picoliters for SAW pulse durations from 50-600 ms. The SAW pulse must be of sufficient duration and power to deform the interface sufficiently to reach the opposing T-junction wall and produce a droplet; here pulses of lower powers (3.1, 3.5 W) require longer pulse times to initiate droplet production.

Wherever a discontinuity in acoustic properties exists an acoustic wave will be able to exert pressure on that interface – this is true for not only water-oil interfaces, but also any particles or cells that may exist in a medium exposed to an acoustic field. However, this force is greatly enhanced for higher frequencies and powers, with the force on the particle $F \sim f^4$ (for radius $\ll \lambda_{SAW}$). Increasing the SAW frequency to 95.4 MHz (λ_{SAW} = 40 μm) it is possible to concentrate particles, here an analogue for cells, at the water-oil interface for subsequent simultaneous droplet production and particle encapsulation.

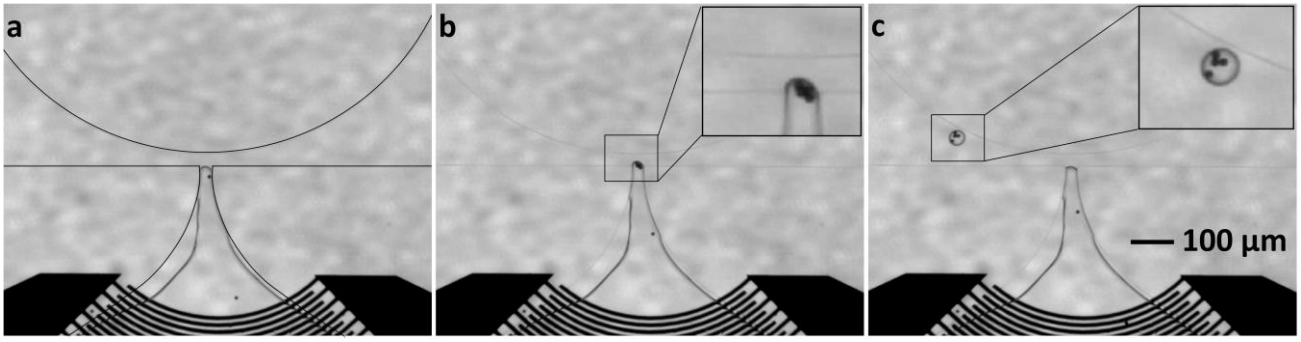

Figure 3: Simultaneous on-demand droplet production and particle encapsulation using SAW. (a) The water-oil interface at rest is (b) subjected to low power, high-frequency 95.4 MHz SAW to concentrate 10 μm particles in a dilute mixture at the interface. Applying a short duration, high power SAW pulse results in an individual water-in-oil droplet encapsulating the concentrated particles. The PDMS boundaries are highlighted in (a) for clarity. Figure is adapted from [8].

CONCLUSION

We have developed a novel system for on-demand production of water-in-oil droplets on a microfluidic platform using SAW. This system combines separate steps of particle concentration, encapsulation and droplet production, where the picoliter-scale droplet size produced can be reliably determined as a function of applied power and SAW pulse duration. We expect this system to find application in high-throughput serial analysis systems requiring programmable, on demand droplet production.

ACKNOWLEDGEMENTS

Fabrication work was performed at the Melbourne Center for Nanofabrication.

REFERENCES

[1] G.F. Christopher, N.N. Noharuddin, J.A. Taylor, and S.L. Anna. Experimental observations of the squeezing to-dripping transition in t-shaped microfluidic junctions. Physical Review E, 78(3):036317, 2008.

[2] A.M. Gañán-Calvo and J.M. Gordillo. Perfectly monodisperse microbubbling by capillary flow focusing. Physical Review Letters, 87(27):274501, 2001.

[3] R.T. Beyer. Radiation pressure: the history of a mislabelled tensor. The Journal of the Acousical Society of America, 63(4):4, 1978.

[4] R. Shilton, M.K. Tan, L.Y. Yeo, and J.R. Friend. Particle concentration and mixing in microdrops driven by focused surface acoustic waves. Journal of Applied Physics, 104(1):014910-014910, 2008.

[5] M. Cecchini, S. Girardo, D. Pisignano, R. Cingolani, and F. Beltram. Acoustic-counter flow microfluidics by surface acoustic waves. Applied Physics Letters, 92(10):104103-104103, 2008.

[6] M.K. Tan, J.R. Friend, and L.Y. Yeo. Interfacial jetting phenomena induced by focused surface vibrations. Physical Review Letters, 103(2):024501, 2009.

[7] D.J. Collins, O. Manor, A. Winkler, H. Schmidt, J.R. Friend, and L.Y. Yeo. Atomization off thin water films generated by high-frequency substrate wave vibrations. Physical Review E, 86(5):056312, 2012.

[8] D.J. Collins, T. Alan, K. Helmerson, A. Neild. Surface acoustic waves for on-demand production of picoliter droplets and particle encapsulation. Lab on a Chip, 13:3225-3231, 2013.

CONTACT

[redacted]

Appendix B

Flow around a PDMS membrane

For completeness, the fluid flow profile in a channel partially impeded by a physical obstruction in the form of a PDMS membrane was modeled using COMSOL. As seen in B.1, local flow velocity is minimized in the space directly behind the membrane, meaning less power is required by the SAW device to retain these particles.

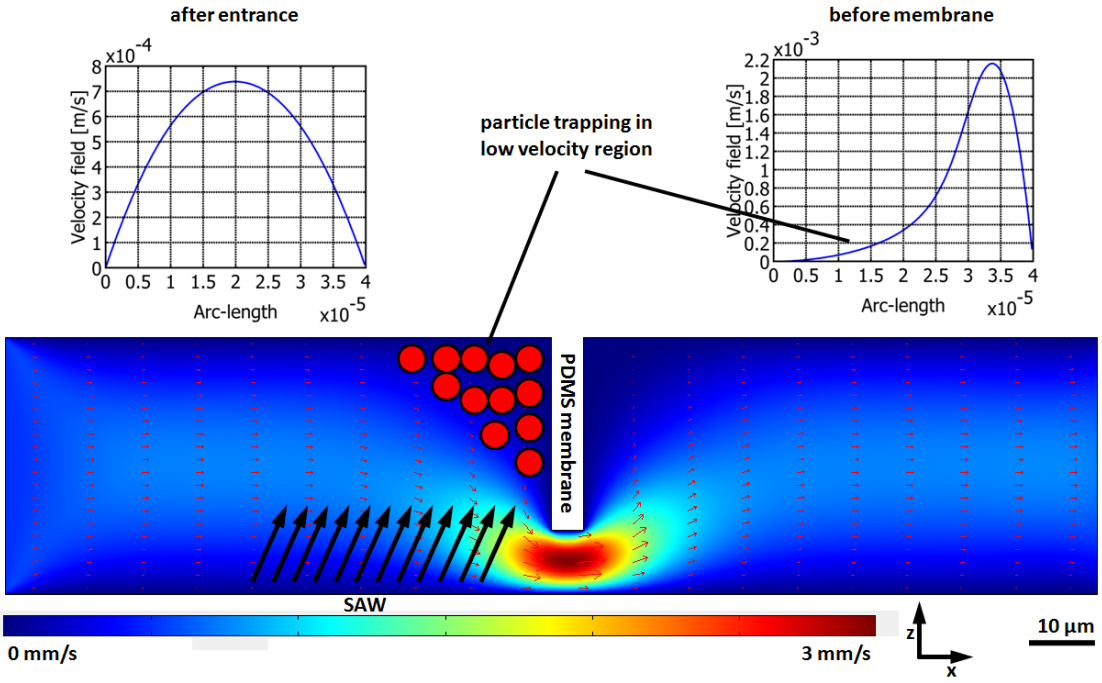

Figure B.1: Particles subject to an acoustic field oriented principally vertically in the system demonstrated in Chapter 6 will are trapped behind a 3D structured PDMS feature. Here, particles collection is aided by the lower characteristic fluid velocity in the region immediately behind this membrane. Discontinuities at the entrance to the channel are a result of the constant 0.5 mm/s flow condition, which quickly relaxes into a normal parabolic flow profile.

References

[1] Nam-Trung Nguyen and Steven T Wereley. *Fundamentals and applications of microfluidics*. Artech House, 2002.

[2] Howard A Stone, Abraham D Stroock, and Armand Ajdari. Engineering flows in small devices. *Annual Review of Fluid Mechanics*, 36:381–411, 2004.

[3] Shia-Yen Teh, Robert Lin, Lung-Hsin Hung, and Abraham P Lee. Droplet microfluidics. *Lab on a Chip*, 8(2):198–220, 2008.

[4] Anonymous Author. Microfluidics in commercial applications; an industry perspective. *Lab on a Chip*, 6(9):1118–1121, 2006.

[5] Joseph Wang. Microchip devices for detecting terrorist weapons. *Analytica Chimica Acta*, 507(1):3–10, 2004.

[6] Carl D Meinhart and Hongsheng Zhang. The flow structure inside a microfabricated inkjet printhead. *Microelectromechanical Systems, Journal of*, 9(1):67–75, 2000.

[7] Charles Q Choi. memjet momentum. *Scientific American*, 296(6):24–26, 2007.

[8] J Heikenfeld, K Zhou, E Kreit, B Raj, S Yang, B Sun, A Milarcik, L Clapp, and R Schwartz. Electrofluidic displays using young–laplace transposition of brilliant pigment dispersions. *Nature Photonics*, 3(5):292–296, 2009.

[9] Curtis D Chin, Tassaneewan Laksanasopin, Yuk Kee Cheung, David Steinmiller, Vincent Linder, Hesam Parsa, Jennifer Wang, Hannah Moore, Robert Rouse, Gisele Umviligihozo, et al. Microfluidics-based diagnostics of infectious diseases in the developing world. *Nature medicine*, 17(8):1015–1019, 2011.

[10] Todd M Squires and Stephen R Quake. Microfluidics: Fluid physics at the nanoliter scale. *Reviews of modern physics*, 77(3):977, 2005.

[11] Guillaume Mernier, Niccolò Piacentini, Thomas Braschler, Nicolas Demierre, and Philippe Renaud. Continuous-flow electrical lysis device with integrated control by dielectrophoretic cell sorting. *Lab on a Chip*, 10(16):2077–2082, 2010.

[12] Arthur Ashkin. Optical trapping and manipulation of neutral particles using lasers. *Proceedings of the National Academy of Sciences*, 94(10):4853–4860, 1997.

[13] A Hultgren, M Tanase, CS Chen, GJ Meyer, and DH Reich. Cell manipulation using magnetic nanowires. *Journal of applied physics*, 93(10):7554–7556, 2003.

[14] Emil Chmela, Robert Tijssen, Marko T Blom, Han JGE Gardeniers, and Albert van den Berg. A chip system for size separation of macromolecules and particles by hydrodynamic chromatography. *Analytical chemistry*, 74(14):3470–3475, 2002.

[15] Filip Petersson, Andreas Nilsson, Cecilia Holm, Henrik Jönsson, and Thomas Laurell. Continuous separation of lipid particles from erythrocytes by means of laminar flow and acoustic standing wave forces. *Lab on a Chip*, 5(1):20–22, 2005.

[16] Thomas Laurell, Filip Petersson, and Andreas Nilsson. Chip integrated strategies for acoustic separation and manipulation of cells and particles. *Chemical Society Reviews*, 36(3):492–506, 2007.

[17] Michelle D Wang, Hong Yin, Robert Landick, Jeff Gelles, and Steven M Block. Stretching dna with optical tweezers. *Biophysical journal*, 72(3):1335–1346, 1997.

[18] Thomas T Perkins, DE Smith, S Chu, et al. Relaxation of a single dna molecule observed by optical microscopy. *Science*, 264(5160):822–826, 1994.

[19] Utkan Demirci and Grace Montesano. Single cell epitaxy by acoustic picolitre droplets. *Lab on a chip*, 7(9):1139–1145, 2007.

[20] JC Rife, MI Bell, JS Horwitz, MN Kabler, RCY Auyeung, and WJ Kim. Miniature valveless ultrasonic pumps and mixers. *Sensors and Actuators A: Physical*, 86(1):135–140, 2000.

[21] Xu Zhu and Eun Sok Kim. Microfluidic motion generation with acoustic waves. *Sensors and Actuators A: Physical*, 66(1):355–360, 1998.

[22] Abhijit Sathaye and Amit Lal. An acoustic vortex generator for microfluidic particle entrapment. In *Ultrasonics Symposium, 2001 IEEE*, volume 1, pages 641–644. IEEE, 2001.

[23] Zhen Yang, Sohei Matsumoto, Hiroshi Goto, Mikio Matsumoto, and Ryutaro Maeda. Ultrasonic micromixer for microfluidic systems. *Sensors and Actuators A: Physical*, 93(3):266–272, 2001.

[24] Christoph J Strobl, Zeno von Guttenberg, and Achim Wixforth. Nano-and pico-dispensing of fluids on planar substrates using saw. *Ultrasonics, Ferroelectrics and Frequency Control, IEEE Transactions on*, 51(11):1432–1436, 2004.

[25] Leslie Y Yeo and James R Friend. Ultrafast microfluidics using surface acoustic waves. *Biomicrofluidics*, 3(1):012002, 2009.

[26] Curtis D Chin, Vincent Linder, and Samuel K Sia. Lab-on-a-chip devices for global health: past studies and future opportunities. *Lab on a Chip*, 7(1):41–57, 2007.

[27] David J Collins, Tuncay Alan, Kristian Helmerson, and Adrian Neild. Surface acoustic waves for on-demand production of picoliter droplets and particle encapsulation. *Lab on a Chip*, 13(16):3225–3231, 2013.

[28] Petra S Dittrich and Andreas Manz. Lab-on-a-chip: microfluidics in drug discovery. *Nature Reviews Drug Discovery*, 5(3):210–218, 2006.

[29] Bernhard H Weigl, Ron L Bardell, and Catherine R Cabrera. Lab-on-a-chip for drug development. *Advanced drug delivery reviews*, 55(3):349–377, 2003.

[30] Xize Niu, Fabrice Gielen, Joshua B Edel, et al. A microdroplet dilutor for high-throughput screening. *Nature chemistry*, 3(6):437–442, 2011.

[31] JGE Gardeniers and A Van den Berg. Lab-on-a-chip systems for biomedical and environmental monitoring. *Analytical and bioanalytical chemistry*, 378(7):1700–1703, 2004.

[32] J Wiest, T Stadthagen, M Schmidhuber, M Brischwein, J Ressler, U Raeder, H Grothe, A Melzer, and B Wolf. Intelligent mobile lab for metabolics in environmental monitoring. *Analytical letters*, 39(8):1759–1771, 2006.

[33] Leanne Marle and Gillian M Greenway. Microfluidic devices for environmental monitoring. *TrAC Trends in Analytical Chemistry*, 24(9):795–802, 2005.

[34] D.J. Collins, O. Manor, A. Winkler, H. Schmidt, J.R. Friend, and L.Y. Yeo. Atomization off thin water films generated by high-frequency substrate wave vibrations. *Physical Review E*, 86(5):056312, 2012.

[35] Aisha Qi, James R Friend, Leslie Y Yeo, David AV Morton, Michelle P McIntosh, and Leone Spiccia. Miniature inhalation therapy platform using surface acoustic wave microfluidic atomization. *Lab on a Chip*, 9(15):2184–2193, 2009.

[36] Brenda S Cho, Timothy G Schuster, Xiaoyue Zhu, David Chang, Gary D Smith, and Shuichi Takayama. Passively driven integrated microfluidic system for separation of motile sperm. *Analytical Chemistry*, 75(7):1671–1675, 2003.

[37] A Valero, JN Post, JW Van Nieuwkasteele, PM Ter Braak, W Kruijer, and A Van Den Berg. Gene transfer and protein dynamics in stem cells using single cell electroporation in a microfluidic device. *Lab on a Chip*, 8(1):62–67, 2008.

[38] Rohit Pal, M Yang, R Lin, BN Johnson, N Srivastava, SZ Razzacki, KJ Chomistek, DC Heldsinger, RM Haque, VM Ugaz, et al. An integrated microfluidic device for influenza and other genetic analyses. *Lab on a Chip*, 5(10):1024–1032, 2005.

[39] Dino Di Carlo, Nima Aghdam, and Luke P Lee. Single-cell enzyme concentrations, kinetics, and inhibition analysis using high-density hydrodynamic cell isolation arrays. *Analytical chemistry*, 78(14):4925–4930, 2006.

[40] Arnaud Bertsch, Stephan Heimgartner, Peter Cousseau, and Philippe Renaud. Static micromixers based on large-scale industrial mixer geometry. *Lab on a Chip*, 1(1):56–60, 2001.

[41] Tae Woo Lim, Yong Son, Yu Jin Jeong, Dong-Yol Yang, Hong-Jin Kong, Kwang-Sup Lee, and Dong-Pyo Kim. Three-dimensionally crossing manifold micro-mixer for fast mixing in a short channel length. *Lab on a Chip*, 11(1):100–103, 2011.

[42] Arjun P Sudarsan and Victor M Ugaz. Multivortex micromixing. *Proceedings of the National Academy of Sciences*, 103(19):7228–7233, 2006.

[43] Kee Suk Ryu, Kashan Shaikh, Edgar Goluch, Zhifang Fan, and Chang Liu. Micro magnetic stir-bar mixer integrated with parylene microfluidic channels. *Lab on a Chip*, 4(6):608–613, 2004.

[44] George M Whitesides. The origins and the future of microfluidics. *Nature*, 442(7101):368–373, 2006.

[45] Eric K Sackmann, Anna L Fulton, and David J Beebe. The present and future role of microfluidics in biomedical research. *Nature*, 507(7491):181–189, 2014.

[46] Daniel Mark, Stefan Haeberle, Günter Roth, Felix von Stetten, and Roland Zengerle. Microfluidic lab-on-a-chip platforms: requirements, characteristics and applications. *Chemical Society Reviews*, 39(3):1153–1182, 2010.

[47] Hoyoung Yun, Kisoo Kim, and Won Gu Lee. Cell manipulation in microfluidics. *Biofabrication*, 5(2):022001, 2013.

[48] Michael Kirschbaum, Christian R Guernth-Marschner, Solène Cherré, Albora de Pablo Peña, Magnus S Jaeger, Richard A Kroczek, Thomas Schnelle, Torsten Mueller, and Claus Duschl. Highly controlled electrofusion of individually selected cells in dielectrophoretic field cages. *Lab on a Chip*, 12(3):443–450, 2012.

[49] Emma Eriksson, Kristin Sott, Fredrik Lundqvist, Martin Sveningsson, Jan Scrimgeour, Dag Hanstorp, Mattias Goksör, and Annette Granéli. A microfluidic device for reversible environmental changes around single cells using optical tweezers for cell selection and positioning. *Lab on a Chip*, 10(5):617–625, 2010.

[50] David C Duffy, Heather L Gillis, Joe Lin, Norman F Sheppard, and Gregory J Kellogg. Microfabricated centrifugal microfluidic systems: characterization and multiple enzymatic assays. *Analytical Chemistry*, 71(20):4669–4678, 1999.

[51] Jun Hirabayashi, Naofumi Ito, Kohji Noguchi, and Kenichi Kasai. Slalom chromatography: size-dependent separation of dna molecules by a hydrodynamic phenomenon. *Biochemistry*, 29(41):9515–9521, 1990.

[52] Hideaki Tsutsui and Chih-Ming Ho. Cell separation by non-inertial force fields in microfluidic systems. *Mechanics research communications*, 36(1):92–103, 2009.

[53] Takashi Yasuda, Shouhei Harada, and Katsuya Daimon. Microfluidic dispensing device using wettability gradient and electrowetting. *IEEJ Transactions on Sensors and Micromachines*, 128:75–79, 2008.

[54] Masumi Yamada and Minoru Seki. Nanoliter-sized liquid dispenser array for multiple biochemical analysis in microfluidic devices. *Analytical chemistry*, 76(4):895–899, 2004.

[55] P Ferraro, S Coppola, S Grilli, M Paturzo, and V Vespini. Dispensing nano-pico droplets and liquid patterning by pyroelectrodynamic shooting. *Nature nanotechnology*, 5(6):429–435, 2010.

[56] Daniel Brassard, Lidija Malic, François Normandin, Maryam Tabrizian, and Teodor Veres. Water-oil core-shell droplets for electrowetting-based digital microfluidic devices. *Lab on a Chip*, 8(8):1342–1349, 2008.

[57] Martina Hitzbleck, Robert D Lovchik, and Emmanuel Delamarche. Flock-based microfluidics. *Advanced Materials*, 25(19):2672–2676, 2013.

[58] Yizhong Wang, Yuejun Zhao, and Sung Kwon Cho. Efficient in-droplet separation of magnetic particles for digital microfluidics. *Journal of Micromechanics and Microengineering*, 17(10):2148, 2007.

[59] Jongin Hong, Suwan N Jayasinghe, et al. Bio-electrospraying and droplet-based microfluidics: control of cell numbers within living residues. *Biomedical Materials*, 5(2):021001, 2010.

[60] Piotr Garstecki, Irina Gitlin, Willow DiLuzio, George M Whitesides, Eugenia Kumacheva, and Howard A Stone. Formation of monodisperse bubbles in a microfluidic flow-focusing device. *Applied Physics Letters*, 85(13):2649–2651, 2004.

[61] P. Garstecki, M.J. Fuerstman, H.A. Stone, and G.M. Whitesides. Formation of droplets and bubbles in a microfluidic t-junctionscaling and mechanism of break-up. *Lab on a Chip*, 6(3):437–446, 2006.

[62] M. De Menech, P. Garstecki, F. Jousse, and HA Stone. Transition from squeezing to dripping in a microfluidic t-shaped junction. *Journal of Fluid Mechanics*, 595(1):141–161, 2008.

[63] Michael Goldin, Joseph Yerushalmi, Robert Pfeffer, and Reuel Shinnar. Breakup of a laminar capillary jet of a viscoelastic fluid. *Journal of Fluid Mechanics*, 38(04):689–711, 1969.

[64] Nagi N Mansour and Thomas S Lundgren. Satellite formation in capillary jet breakup. *Physics of Fluids A: Fluid Dynamics (1989-1993)*, 2(7):1141–1144, 1990.

[65] Manu Prakash and Neil Gershenfeld. Microfluidic bubble logic. *Science*, 315(5813):832–835, 2007.

[66] Tor Vestad, David WM Marr, and Toshinori Munakata. Flow resistance for microfluidic logic operations. *Applied Physics Letters*, 84(25):5074–5075, 2004.

[67] Yang Zhao, Tao Xu, and Krishnendu Chakrabarty. Digital microfluidic logic gates. In *Nano-Net*, pages 54–60. Springer, 2009.

[68] Mengying Zhang, Limu Wang, Xiang Wang, Jinbo Wu, Jiaxing Li, Xiuqing Gong, Jianhua Qin, Weihua Li, and Weijia Wen. Microdroplet-based universal logic gates by electrorheological fluid. *Soft Matter*, 7(16):7493–7497, 2011.

[69] Minsoung Rhee and Mark A Burns. Microfluidic pneumatic logic circuits and digital pneumatic microprocessors for integrated microfluidic systems. *Lab on a Chip*, 9(21):3131–3143, 2009.

[70] Zuoyan Han, Wentao Li, Yanyi Huang, and Bo Zheng. Measuring rapid enzymatic kinetics by electrochemical method in droplet-based microfluidic devices with pneumatic valves. *Analytical chemistry*, 81(14):5840–5845, 2009.

[71] Jae-Hoon Choi, Seung-Kon Lee, Jong-Min Lim, Seung-Man Yang, and Gi-Ra Yi. Designed pneumatic valve actuators for controlled droplet breakup and generation. *Lab on a Chip*, 10(4):456–461, 2010.

[72] Chunsun Zhang, Da Xing, and Yuyuan Li. Micropumps, microvalves, and micromixers within pcr microfluidic chips: advances and trends. *Biotechnology advances*, 25(5):483–514, 2007.

[73] Charles N Baroud, Matthieu Robert de Saint Vincent, and Jean-Pierre Delville. An optical toolbox for total control of droplet microfluidics. *Lab on a Chip*, 7(8):1029–1033, 2007.

[74] Nam-Trung Nguyen, Sumantri Lassemono, and Franck Alexis Chollet. Optical detection for droplet size control in microfluidic droplet-based analysis systems. *Sensors and Actuators B: Chemical*, 117(2):431–436, 2006.

[75] Jean-Christophe Baret, Oliver J Miller, Valerie Taly, Michaël Ryckelynck, Abdeslam El-Harrak, Lucas Frenz, Christian Rick, Michael L Samuels, J Brian Hutchison, Jeremy J Agresti, et al. Fluorescence-activated droplet sorting (fads): efficient microfluidic cell sorting based on enzymatic activity. *Lab on a Chip*, 9(13):1850–1858, 2009.

[76] Darren R Link, Erwan Grasland-Mongrain, Agnes Duri, Flavie Sarrazin, Zhengdong Cheng, Galder Cristobal, Manuel Marquez, and David A Weitz. Electric control of droplets in microfluidic devices. *Angewandte Chemie International Edition*, 45(16):2556–2560, 2006.

[77] Feng Guo, Xing-Hu Ji, Kan Liu, Rong-Xiang He, Li-Bo Zhao, Zhi-Xiao Guo, Wei Liu, Shi-Shang Guo, and Xing-Zhong Zhao. Droplet electric separator microfluidic device for cell sorting. *Applied Physics Letters*, 96(19):193701, 2010.

[78] Thomas Franke, Adam R Abate, David A Weitz, and Achim Wixforth. Surface acoustic wave (saw) directed droplet flow in microfluidics for pdms devices. *Lab on a Chip*, 9(18):2625–2627, 2009.

[79] T Franke, S Braunmüller, L Schmid, A Wixforth, and DA Weitz. Surface acoustic wave actuated cell sorting (sawacs). *Lab on a chip*, 10(6):789–794, 2010.

[80] Jonathan Shemesh, Avishay Bransky, Maria Khoury, and Shulamit Levenberg. Advanced microfluidic droplet manipulation based on piezoelectric actuation. *Biomedical microdevices*, 12(5):907–914, 2010.

[81] Zhuochen Wang and Jiang Zhe. Recent advances in particle and droplet manipulation for lab-on-a-chip devices based on surface acoustic waves. *Lab on a Chip*, 11(7):1280–1285, 2011.

[82] Robert M Lorenz, J Scott Edgar, Gavin DM Jeffries, and Daniel T Chiu. Microfluidic and optical systems for the on-demand generation and manipulation of single femtoliter-volume aqueous droplets. *Analytical chemistry*, 78(18):6433–6439, 2006.

[83] Jie Xu and Daniel Attinger. Drop on demand in a microfluidic chip. *Journal of Micromechanics and Microengineering*, 18(6):065020, 2008.

[84] Sung-Yong Park, Ting-Hsiang Wu, Yue Chen, Michael A Teitell, and Pei-Yu Chiou. High-speed droplet generation on demand driven by pulse laser-induced cavitation. *Lab on a Chip*, 11(6):1010–1012, 2011.

[85] Feng Guo, Kan Liu, Xing-Hu Ji, Hui-Jiang Ding, Meng Zhang, Qian Zeng, Wei Liu, Shi-Shang Guo, and Xing-Zhong Zhao. Valve-based microfluidic device for droplet on-demand operation and static assay. *Applied Physics Letters*, 97(23):233701, 2010.

[86] Sungyoung Choi, Jeffrey M Karp, and Rohit Karnik. Cell sorting by deterministic cell rolling. *Lab on a Chip*, 12(8):1427–1430, 2012.

[87] MP MacDonald, GC Spalding, Kishan Dholakia, et al. Microfluidic sorting in an optical lattice. *Nature*, 426(6965):421–424, 2003.

[88] Xiaolin Wang, Shuxun Chen, Marco Kong, Zuankai Wang, Kevin D Costa, Ronald A Li, and Dong Sun. Enhanced cell sorting and manipulation with combined optical tweezer and microfluidic chip technologies. *Lab on a Chip*, 11(21):3656–3662, 2011.

[89] Stephen L Levy and Harold G Craighead. Dna manipulation, sorting, and mapping in nanofluidic systems. *Chemical Society Reviews*, 39(3):1133–1152, 2010.

[90] Hadi Shafiee, John L Caldwell, Michael B Sano, and Rafael V Davalos. Contactless dielectrophoresis: a new technique for cell manipulation. *Biomedical microdevices*, 11(5):997–1006, 2009.

[91] Xiaoyun Ding, Sz-Chin Steven Lin, Brian Kiraly, Hongjun Yue, Sixing Li, I-Kao Chiang, Jinjie Shi, Stephen J Benkovic, and Tony Jun Huang. On-chip manipulation of single microparticles, cells, and organisms using surface acoustic waves. *Proceedings of the National Academy of Sciences*, 109(28):11105–11109, 2012.

[92] Seungkyung Park, Yi Zhang, Tza-Huei Wang, and Samuel Yang. Continuous dielectrophoretic bacterial separation and concentration from physiological media of high conductivity. *Lab on a Chip*, 11(17):2893–2900, 2011.

[93] Haiyan Li, James R Friend, and Leslie Y Yeo. Surface acoustic wave concentration of particle and bioparticle suspensions. *Biomedical Microdevices*, 9(5):647–656, 2007.

[94] R. Shilton, M.K. Tan, L.Y. Yeo, and J.R. Friend. Particle concentration and mixing in microdrops driven by focused surface acoustic waves. *Journal of Applied Physics*, 104(1):014910–014910, 2008.

[95] R Gomez-Sjoberg, Dallas T Morisette, and Rashid Bashir. Impedance microbiology-on-a-chip: Microfluidic bioprocessor for rapid detection of bacterial metabolism. *Microelectromechanical Systems, Journal of*, 14(4):829–838, 2005.

[96] MK Tan, LY Yeo, and JR Friend. Rapid fluid flow and mixing induced in microchannels using surface acoustic waves. *Europhysics Letters*, 87(4):47003, 2009.

[97] Somphop Rodamporn, NR Harris, Steve P Beeby, Rosemary J Boltryk, and Tilman Sanchez-Eisner. Hela cell transfection using a novel sonoporation system. *Biomedical Engineering, IEEE Transactions on*, 58(4):927–934, 2011.

[98] Hang Lu, Martin A Schmidt, and Klavs F Jensen. A microfluidic electroporation device for cell lysis. *Lab on a Chip*, 5(1):23–29, 2005.

[99] Chia-Yen Lee, Gwo-Bin Lee, Jr-Lung Lin, Fu-Chun Huang, and Chia-Sheng Liao. Integrated microfluidic systems for cell lysis, mixing/pumping and dna amplification. *Journal of Micromechanics and Microengineering*, 15(6):1215, 2005.

[100] Dongeun Huh, Hideki Fujioka, Yi-Chung Tung, Nobuyuki Futai, Robert Paine, James B Grotberg, and Shuichi Takayama. Acoustically detectable cellular-level lung injury induced by fluid mechanical stresses in microfluidic airway systems. *Proceedings of the National Academy of Sciences*, 104(48):18886–18891, 2007.

[101] Jinjie Shi, Daniel Ahmed, Xiaole Mao, Sz-Chin Steven Lin, Aitan Lawit, and Tony Jun Huang. Acoustic tweezers: patterning cells and microparticles using standing surface acoustic waves (ssaw). *Lab on a Chip*, 9(20):2890–2895, 2009.

[102] Jessica Hultström, Otto Manneberg, Katja Dopf, Hans M Hertz, Hjalmar Brismar, and Martin Wiklund. Proliferation and viability of adherent cells manipulated by standing-wave ultrasound in a microfluidic chip. *Ultrasound in medicine & biology*, 33(1):145–151, 2007.

[103] Darren S Gray, John L Tan, Joel Voldman, and Christopher S Chen. Dielectrophoretic registration of living cells to a microelectrode array. *Biosensors and Bioelectronics*, 19(7):771–780, 2004.

[104] Lo-Chang Hsiung, Chun-Hui Yang, Chi-Li Chiu, Chen-Lin Chen, Yueh Wang, Hsinyu Lee, Ji-Yen Cheng, Ming-Chih Ho, and Andrew M Wo. A planar interdigitated ring electrode array via dielectrophoresis for uniform patterning of cells. *Biosensors and Bioelectronics*, 24(4):869–875, 2008.

[105] Ana Egatz-Gómez, Sonia Melle, Antonio A García, SA Lindsay, M Márquez, P Dominguez-Garcia, Miguel A Rubio, ST Picraux, JL Taraci, T Clement, et al. Discrete magnetic microfluidics. *Applied Physics Letters*, 89(3):034106, 2006.

[106] Nicole Pamme and Claire Wilhelm. Continuous sorting of magnetic cells via on-chip free-flow magnetophoresis. *Lab on a Chip*, 6(8):974–980, 2006.

[107] Mark Tondra, Mike Granger, Rachel Fuerst, Marc Porter, Catherine Nordman, John Taylor, and Seraphin Akou. Design of integrated microfluidic device for sorting magnetic beads in biological assays. *Magnetics, IEEE Transactions on*, 37(4):2621–2623, 2001.

[108] Chengxun Liu, Tim Stakenborg, Sara Peeters, and Liesbet Lagae. Cell manipulation with magnetic particles toward microfluidic cytometry. *Journal of Applied Physics*, 105(10):102014, 2009.

[109] Z Jiang, J Llandro, T Mitrelias, and JAC Bland. An integrated microfluidic cell for detection, manipulation, and sorting of single micron-sized magnetic beads. *Journal of applied physics*, 99(8):08S105, 2006.

[110] Allen HJ Yang, Sean D Moore, Bradley S Schmidt, Matthew Klug, Michal Lipson, and David Erickson. Optical manipulation of nanoparticles and biomolecules in sub-wavelength slot waveguides. *Nature*, 457(7225):71–75, 2009.

[111] J. Shi, X. Mao, D. Ahmed, A. Colletti, and T.J. Huang. Focusing microparticles in a microfluidic channel with standing surface acoustic waves (ssaw). *Lab on a Chip*, 8(2):221–223, 2008.

[112] Maulik V Patel, Armando R Tovar, and Abraham P Lee. Lateral cavity acoustic transducer as an on-chip cell/particle microfluidic switch. *Lab on a chip*, 12(1):139–145, 2012.

[113] Keunho Ahn, Charles Kerbage, Tom P Hunt, RM Westervelt, Darren R Link, and DA Weitz. Dielectrophoretic manipulation of drops for high-speed microfluidic sorting devices. *Applied Physics Letters*, 88(2):024104–024104, 2006.

[114] Barbaros Çetin and Dongqing Li. Dielectrophoresis in microfluidics technology. *Electrophoresis*, 32(18):2410–2427, 2011.

[115] Zachary R Gagnon. Cellular dielectrophoresis: applications to the characterization, manipulation, separation and patterning of cells. *Electrophoresis*, 32(18):2466–2487, 2011.

[116] Shunbo Li, Ming Li, Kristelle Bougot-Robin, Wenbin Cao, Irene Yeung Yeung Chau, Weihua Li, and Weijia Wen. High-throughput particle manipulation by hydrodynamic, electrokinetic, and dielectrophoretic effects in an integrated microfluidic chip. *Biomicrofluidics*, 7(2):024106, 2013.

[117] Jaap MJ den Toonder and Patrick R Onck. Microfluidic manipulation with artificial/bioinspired cilia. *Trends in biotechnology*, 31(2):85–91, 2013.

[118] Wong Cheng Lee, Ali Asgar S Bhagat, Sha Huang, Krystyn J Van Vliet, Jongyoon Han, and Chwee Teck Lim. High-throughput cell cycle synchronization using inertial forces in spiral microchannels. *Lab on a chip*, 11(7):1359–1367, 2011.

[119] Dino Di Carlo. Inertial microfluidics. *Lab on a Chip*, 9(21):3038–3046, 2009.

[120] Yoko Yamanishi, Yu-Ching Lin, and Fumihito Arai. Magnetically modified pdms microtools for micro particle manipulation. In *Intelligent Robots and Systems, 2007. IROS 2007. IEEE/RSJ International Conference on*, pages 753–758. IEEE, 2007.

[121] Myeong Chan Jo and Rasim Guldiken. Particle manipulation by phase-shifting of surface acoustic waves. *Sensors and Actuators A: Physical*, 207:39–42, 2014.

[122] Sathyakumar S Kuntaegowdanahalli, Ali Asgar S Bhagat, Girish Kumar, and Ian Papautsky. Inertial microfluidics for continuous particle separation in spiral microchannels. *Lab on a Chip*, 9(20):2973–2980, 2009.

[123] Hywel Morgan, Michael P Hughes, and Nicolas G Green. Separation of submicron bioparticles by dielectrophoresis. *Biophysical journal*, 77(1):516–525, 1999.

[124] Justin E Molloy and Miles J Padgett. Lights, action: optical tweezers. *Contemporary Physics*, 43(4):241–258, 2002.

[125] Nicole Pamme. Magnetism and microfluidics. *Lab on a Chip*, 6(1):24–38, 2006.

[126] Hywel Morgan, Alberto García Izquierdo, David Bakewell, Nicolas G Green, and Antonio Ramos. The dielectrophoretic and travelling wave forces generated by interdigitated electrode arrays: analytical solution using fourier series. *Journal of Physics D: Applied Physics*, 34(10):1553, 2001.

[127] Peter Gascoyne, Chulabhorn Mahidol, Mathuros Ruchirawat, Jutamaad Satayavivad, Piyajit Watcharasit, and Frederick F Becker. Microsample preparation by dielectrophoresis: isolation of malaria. *Lab on a Chip*, 2(2):70–75, 2002.

[128] DA Fedosov, B Caswell, S Suresh, and GE Karniadakis. Quantifying the biophysical characteristics of plasmodium-falciparum-parasitized red blood cells in microcirculation. *Proceedings of the National Academy of Sciences*, 108(1):35–39, 2011.

[129] Andreas Nilsson, Filip Petersson, Henrik Jönsson, and Thomas Laurell. Acoustic control of suspended particles in micro fluidic chips. *Lab on a Chip*, 4(2):131–135, 2004.

[130] Zeno Guttenberg, Helena Müller, Heiko Habermüller, Andreas Geisbauer, Jürgen Pipper, Jana Felbel, Mark Kielpinski, Jürgen Scriba, and Achim Wixforth. Planar chip device for pcr and hybridization with surface acoustic wave pump. *Lab on a Chip*, 5(3):308–317, 2005.

[131] XY Du, YQ Fu, JK Luo, AJ Flewitt, and WI Milne. Microfluidic pumps employing surface acoustic waves generated in zno thin films. *Journal of Applied Physics*, 105(2):024508, 2009.

[132] Rachel E Saunders, Julie E Gough, and Brian Derby. Delivery of human fibroblast cells by piezoelectric drop-on-demand inkjet printing. *Biomaterials*, 29(2):193–203, 2008.

[133] Richie J Shilton, Nick R Glass, Peggy Chan, Leslie Y Yeo, and James R Friend. Rotational microfluidic motor for on-chip microcentrifugation. *Applied Physics Letters*, 98(25):254103, 2011.

[134] Erika J Fong, Amanda C Johnston, Timothy Notton, Seung-Yong Jung, Klint A Rose, Leor S Weinberger, and Maxim Shusteff. Acoustic focusing with engineered node locations for high-performance microfluidic particle separation. *Analyst*, 2014.

[135] Warren P Mason. Piezoelectricity, its history and applications. *The Journal of the Acoustical Society of America*, 70(6):1561–1566, 1981.

[136] Ronald M Hays and Clinton S Hartmann. Surface-acoustic-wave devices for communications. *Proceedings of the IEEE*, 64(5):652–671, 1976.

[137] J. Friend and L.Y. Yeo. Microscale acoustofluidics: Microfluidics driven via acoustics and ultrasonics. *Reviews of Modern Physics*, 83(2):647, 2011.

[138] Sean M Langelier, Leslie Y Yeo, and James Friend. Uv epoxy bonding for enhanced saw transmission and microscale acoustofluidic integration. *Lab on a Chip*, 12(16):2970–2976, 2012.

[139] Ming K Tan, Leslie Y Yeo, and James R Friend. Unique flow transitions and particle collection switching phenomena in a microchannel induced by surface acoustic waves. *Applied Physics Letters*, 97(23):234106, 2010.

[140] Ryan P Hodgson, Ming Tan, Leslie Yeo, and James Friend. Transmitting high power rf acoustic radiation via fluid couplants into superstrates for microfluidics. *Applied Physics Letters*, 94(2):024102, 2009.

[141] M. Cecchini, S. Girardo, D. Pisignano, R. Cingolani, and F. Beltram. Acoustic-counterflow microfluidics by surface acoustic waves. *Applied Physics Letters*, 92(10):104103–104103, 2008.

[142] Achim Wixforth. Acoustically driven programmable microfluidics for biological and chemical applications. *Journal of the Association for Laboratory Automation*, 11(6):399–405, 2006.

[143] Saku Lehtonen, Victor P Plessky, and Martti M Salomaa. Short reflectors operating at the fundamental and second harmonics on 128/spl deg/linbo/sub 3. *Ultrasonics, Ferroelectrics and Frequency Control, IEEE Transactions on*, 51(3):343–351, 2004.

[144] PV Wright. The natural single-phase unidirectional transducer: a new low-loss saw transducer. In *IEEE 1985 Ultrasonics Symposium*, pages 58–63. IEEE, 1985.

[145] VB Chvets, PG Ivanov, VM Makarov, and VS Orlov. Low-loss saw filters using new spudt structures. In *Ultrasonics Symposium, 1997. Proceedings., 1997 IEEE*, volume 1, pages 69–72. IEEE, 1997.

[146] Tsung-Tsong Wu, He-Tai Tang, Yung-Yu Chen, and P-L Liu. Analysis and design of focused interdigital transducers. *Ultrasonics, Ferroelectrics and Frequency Control, IEEE Transactions on*, 52(8):1384–1392, 2005.

[147] Hiromi Yatsuda. Design techniques for saw filters using slanted finger interdigital transducers. *Ultrasonics, Ferroelectrics and Frequency Control, IEEE Transactions on*, 44(2):453–459, 1997.

[148] RT Smith and FS Welsh. Temperature dependence of the elastic, piezoelectric, and dielectric constants of lithium tantalate and lithium niobate. *Journal of applied physics*, 42(6):2219–2230, 2003.

[149] James F Tressler, Sedat Alkoy, and Robert E Newnham. Piezoelectric sensors and sensor materials. *Journal of Electroceramics*, 2(4):257–272, 1998.

[150] Colin Campbell. *Surface acoustic wave devices for mobile and wireless communications*. Academic press, 1998.

[151] A Holm, P Wallner, W Ruile, and R Weigel. High-resolution optical probing of saw and leaky saw structures. In *Ultrasonics Symposium IEEE Proceedings*, volume 1, pages 153–156. IEEE, 1997.

[152] Y Li, YQ Fu, SD Brodie, M Alghane, and AJ Walton. Integrated microfluidics system using surface acoustic wave and electrowetting on dielectrics technology. *Biomicrofluidics*, 6(1):012812, 2012.

[153] Sir James Lighthill. Acoustic streaming. *Journal of Sound and Vibration*, 61(3):391–418, 1978.

[154] T. Hasegawa, T. Kido, T. Iizuka, and C. Matsuoka. A general theory of rayleigh and langevin radiation pressures. *Acoustical Science and Technology*, 21(3):145–152, 2000.

[155] B.T. Chu and R.E. Apfel. Acoustic radiation pressure produced by a beam of sound. *The Journal of the Acoustical Society of America*, 72:1673, 1982.

[156] J.A. Rooney and W.L. Nyborg. Acoustic radiation pressure in a traveling plane wave. *American Journal of Physics*, 40:1825, 1972.

[157] FE Fox and WA Wallace. Absorption of finite amplitude sound waves. *The Journal of the Acoustical Society of America*, 26(6):994–1006, 1954.

[158] Vladimir Aleksandrovich Shutilov and Michael E Alferieff. *Fundamental physics of ultrasound*, volume 149. Gordon and Breach Science Publishers New York, 1988.

[159] Louis V King. On the acoustic radiation pressure on spheres. *Proceedings of the Royal Society of London. Series A-Mathematical and Physical Sciences*, 147(861):212–240, 1934.

[160] B.J.W.S. Rayleigh. *The theory of sound*, volume 2. Macmillan, 1896.

[161] G. Fuhr, R. Hagedorn, T. Muller, W. Benecke, and B. Wagner. Pumping of water solutions in microfabricated electrohydrodynamic systems. In *Micro Electro Mechanical Systems, 1992, MEMS'92, Proceedings. An Investigation of Micro Structures, Sensors, Actuators, Machines and Robot. IEEE*, pages 25–30. IEEE, 1992.

[162] XY Huang, C.Y. Wen, and ZJ Jiao. A standing wave model for acoustic pumping effect in microchannels. *Applied Acoustics*, 71(2):164–168, 2010.

[163] A.H. Meng, N.T. Nguyen, and R.M. White. Focused flow micropump using ultrasonic flexural plate waves. *Biomedical Microdevices*, 2(3):169–174, 2000.

[164] S.B. Huang, M.H. Wu, Z. Cui, Z. Cui, and G.B. Lee. A membrane-based serpentine-shape pneumatic micropump with pumping performance modulated by fluidic resistance. *Journal of Micromechanics and Microengineering*, 18:045008, 2008.

[165] T. Hasegawa, K. Nakamura, and S. Ueha. A miniature ultransonic pump using a bending disk transducer and a gap. *Ultrasonics*, 44:e575–e579, 2006.

[166] T. Hasegawa, D. Koyama, K. Nakamura, and S. Ueha. A design of a miniature ultrasonic pump using a bending disk transducer. *Journal of Electroceramics*, 20(3):145–151, 2008.

[167] RM Moroney, RM White, and RT Howe. Ultrasonically induced microtransport. In *Micro Electro Mechanical Systems, 1991, MEMS'91, Proceedings. An Investigation of Micro Structures, Sensors, Actuators, Machines and Robots. IEEE*, pages 277–282. IEEE, 1991.

[168] L. Masini, M. Cecchini, S. Girardo, R. Cingolani, D. Pisignano, and F. Beltram. Surface-acoustic-wave counterflow micropumps for on-chip liquid motion control in two-dimensional microchannel arrays. *Lab Chip*, 10(15):1997–2000, 2010.

[169] L.G. Leal. *Advanced transport phenomena: fluid mechanics and convective transport processes*. Cambridge Univ Pr, 2010.

[170] M.F. Hamilton and D.T. Blackstock. *Nonlinear acoustics*. Academic Pr, 1998.

[171] S. Shiokawa, Y. Matsui, and T. Ueda. Liquid streaming and droplet formation caused by leaky rayleigh waves. In *Ultrasonics Symposium, 1989. Proceedings., IEEE 1989*, pages 643–646. IEEE, 1989.

[172] G.Q. Zhang, K. Hashimoto, and M. Yamaguchi. Liquid streaming by high-frequency ultrasonic waves. *Jpn. J. Appi. Phys. Vol*, 35:3248–3250, 1996.

[173] W.L. Nyborg. Acoustic streaming due to attenuated plane waves. *The journal of the acoustical society of America*, 25:68, 1953.

[174] H. Schlichting. Berechnung ebener periodischer grenzschichtstromungen. *Phys. Z*, 33(1932):327–335, 1932.

[175] S.K.R.S. Sankaranarayanan, S. Cular, V.R. Bhethanabotla, and B. Joseph. Flow induced by acoustic streaming on surface-acoustic-wave devices and its application in biofouling removal: A computational study and comparisons to experiment. *Physical Review E*, 77(6):066308, 2008.

[176] R.V. Raghavan, J.R. Friend, and L.Y. Yeo. Particle concentration via acoustically driven microcentrifugation: micropiv flow visualization and numerical modelling studies. *Microfluidics and Nanofluidics*, 8(1):73–84, 2010.

[177] F. Barreras, H. Amaveda, and A. Lozano. Transient high-frequency ultrasonic water atomization. *Experiments in fluids*, 33(3):405–413, 2002.

[178] Bojan Vukasinovic, Marc K Smith, and Ari Glezer. Mechanisms of free-surface breakup in vibration-induced liquid atomization. *Physics of Fluids (1994-present)*, 19(1):012104, 2007.

[179] Scott R Heron, Rab Wilson, Scott A Shaffer, David R Goodlett, and Jonathan M Cooper. Surface acoustic wave nebulization of peptides as a microfluidic interface for mass spectrometry. *Analytical chemistry*, 82(10):3985–3989, 2010.

[180] Lucía Martín-Banderas, María Flores-Mosquera, Pascual Riesco-Chueca, Alfonso Rodríguez-Gil, Ángel Cebolla, Sebastián Chávez, and Alfonso M Gañán-Calvo. Flow focusing: A versatile technology to produce size-controlled and specific-morphology microparticles. *Small*, 1(7):688–692, 2005.

[181] AM Ganan-Calvo, J Davila, and A Barrero. Current and droplet size in the electrospraying of liquids. scaling laws. *Journal of Aerosol Science*, 28(2):249–275, 1997.

[182] Minoru Kurosawa, Takayuki Watanabe, Akira Futami, and Toshiro Higuchi. Surface acoustic wave atomizer. *Sensors and Actuators A: Physical*, 50(1):69–74, 1995.

[183] Richard L Peskin and Roland J Raco. Ultrasonic atomization of liquids. *The Journal of the Acoustical Society of America*, 35(9):1378–1381, 2005.

[184] Jeremy Blamey, Leslie Y Yeo, and James R Friend. Microscale capillary wave turbulence excited by high frequency vibration. *Langmuir*, 29(11):3835–3845, 2013.

[185] W Eisenmenger. Dynamic properties of the surface tension of water and aqueous solutions of surface active agents with standing capillary waves in the frequency range from 10 kc/s to 1.5 mc/s. *Acta Acustica united with Acustica*, 9(4):327–340, 1959.

[186] EG Lierke and G Griesshammer. The formation of metal powders by ultrasonic atomization of molten metals. *Ultrasonics*, 5(4):224–228, 1967.

[187] Robert J Lang. Ultrasonic atomization of liquids. *The journal of the acoustical society of America*, 34(1):6–8, 2005.

[188] Aisha Qi, Leslie Y Yeo, and James R Friend. Interfacial destabilization and atomization driven by surface acoustic waves. *Physics of Fluids (1994-present)*, 20(7):074103, 2008.

[189] James R Friend, Leslie Y Yeo, Dian R Arifin, and Adam Mechler. Evaporative self-assembly assisted synthesis of polymeric nanoparticles by surface acoustic wave atomization. *Nanotechnology*, 19(14):145301, 2008.

[190] Jeong Hoon Lee, Benjamin D Cosgrove, Douglas A Lauffenburger, and Jongyoon Han. Microfluidic concentration-enhanced cellular kinase activity assay. *Journal of the American Chemical Society*, 131(30):10340–10341, 2009.

[191] Richard W Light, M Isabelle Macgregor, Peter C Luchsinger, and Wilmot C Ball. Pleural effusions: the diagnostic separation of transudates and exudates. *Annals of Internal Medicine*, 77(4):507–513, 1972.

[192] R Huang, TA Barber, MA Schmidt, RG Tompkins, M Toner, DW Bianchi, R Kapur, and WL Flejter. A microfluidics approach for the isolation of nucleated red blood cells (nrbcs) from the peripheral blood of pregnant women. *Prenatal diagnosis*, 28(10):892–899, 2008.

[193] Leslie Y Yeo, James R Friend, and Dian R Arifin. Electric tempest in a teacup: The tea leaf analogy to microfluidic blood plasma separation. *Applied physics letters*, 89(10):103516, 2006.

[194] Nick R Glass, Richie J Shilton, Peggy PY Chan, James R Friend, and Leslie Y Yeo. Miniaturized lab-on-a-disc (miniload). *small*, 8(12):1881–1888, 2012.

[195] Matthew S Pommer, Yanting Zhang, Nawarathna Keerthi, Dong Chen, James A Thomson, Carl D Meinhart, and Hyongsok T Soh. Dielectrophoretic separation of platelets from diluted whole blood in microfluidic channels. *Electrophoresis*, 29(6):1213–1218, 2008.

[196] Sunitha Nagrath, Lecia V Sequist, Shyamala Maheswaran, Daphne W Bell, Daniel Irimia, Lindsey Ulkus, Matthew R Smith, Eunice L Kwak, Subba Digumarthy, Alona Muzikansky, et al. Isolation of rare circulating tumour cells in cancer patients by microchip technology. *Nature*, 450(7173):1235–1239, 2007.

[197] Jeremy J Agresti, Eugene Antipov, Adam R Abate, Keunho Ahn, Amy C Rowat, Jean-Christophe Baret, Manuel Marquez, Alexander M Klibanov, Andrew D Griffiths, and David A Weitz. Ultrahigh-throughput screening in drop-based microfluidics for directed evolution. *Proceedings of the National Academy of Sciences*, 107(9):4004–4009, 2010.

[198] Brian M Paegel and Gerald F Joyce. Darwinian evolution on a chip. *PLoS biology*, 6(4):e85, 2008.

[199] Leonard A Herzenberg, Richard G Sweet, and Leonore A Herzenberg. Fluorescence-activated cell sorting. *Sci Am*, 234(3):108–117, 1976.

[200] Fernando Patolsky, Gengfeng Zheng, Oliver Hayden, Melike Lakadamyali, Xiaowei Zhuang, and Charles M Lieber. Electrical detection of single viruses. *Proceedings of the National Academy of Sciences of the United States of America*, 101(39):14017–14022, 2004.

[201] Kerstin Länge, Bastian E Rapp, and Michael Rapp. Surface acoustic wave biosensors: a review. *Analytical and Bioanalytical Chemistry*, 391(5):1509–1519, 2008.

[202] Jinjie Shi, Hua Huang, Zak Stratton, Yiping Huang, and Tony Jun Huang. Continuous particle separation in a microfluidic channel via standing surface acoustic waves (ssaw). *Lab Chip*, 9(23):3354–3359, 2009.

[203] Ghulam Destgeer, Kyung Heon Lee, Jin Ho Jung, Anas Alazzam, and Hyung Jin Sung. Continuous separation of particles in a pdms microfluidic channel via travelling surface acoustic waves (tsaw). *Lab on a Chip*, 13(21):4210–4216, 2013.

[204] Quan Qi and Giles John Brereton. Mechanisms of removal of micron-sized particles by high-frequency ultrasonic waves. *Ultrasonics IEEE Transactions on Ferroelectrics and Frequency Control*, 42(4):619–629, 1995.

[205] D Čiplys and R Rimeika. Measurements of electromechanical coupling coefficient for surface acoustic waves in proton-exchanged lithium niobate. *ULTRAGARSAS journal*, 33(3):14–20, 1999.

[206] Sami Franssila. Deep reactive ion etching. *Introduction to Microfabrication, Second Edition*, pages 255–270.

[207] Mark A Eddings, Michael A Johnson, and Bruce K Gale. Determining the optimal pdms–pdms bonding technique for microfluidic devices. *Journal of Micromechanics and Microengineering*, 18(6):067001, 2008.

[208] Shantanu Bhattacharya, Arindom Datta, Jordan M Berg, and Shubhra Gangopadhyay. Studies on surface wettability of poly (dimethyl) siloxane (pdms) and glass under oxygen-plasma treatment and correlation with bond strength. *Microelectromechanical Systems, Journal of*, 14(3):590–597, 2005.

[209] B-H Jo, Linda M Van Lerberghe, Kathleen M Motsegood, and David J Beebe. Three-dimensional micro-channel fabrication in polydimethylsiloxane (pdms) elastomer. *Microelectromechanical Systems, Journal of*, 9(1):76–81, 2000.

[210] Benjamin Aaron Evans. *Design, fabrication, and actuation of biomimetic cilia*. ProQuest, 2008.

[211] CL Leach, PJ Davidson, and RJ Boudreau. Improved airway targeting with the cfc-free hfa-beclomethasone metered-dose inhaler compared with cfc-beclomethasone. *European Respiratory Journal*, 12(6):1346–1353, 1998.

[212] Hugh DC Smyth. Multimodal particle size distributions emitted from hfa-134a solution pressurized metered-dose inhalers. *AAPS PharmSciTech*, 4(3):76–86, 2003.

[213] Jolyon P Mitchell, Mark W Nagel, Kimberly J Wiersema, and Cathy C Doyle. Aerodynamic particle size analysis of aerosols from pressurized metered-dose inhalers: comparison of andersen 8-stage cascade impactor, next generation pharmaceutical impactor, and model 3321 aerodynamic particle sizer aerosol spectrometer. *AAPS PharmSciTech*, 4(4):425–433, 2003.

[214] Avishay Bransky, Natanel Korin, Maria Khoury, and Shulamit Levenberg. A microfluidic droplet generator based on a piezoelectric actuator. *Lab on a Chip*, 9(4):516–520, 2008.

[215] David J Collins, Tuncay Alan, and Adrian Neild. The particle valve: On-demand particle trapping, filtering, and release from a microfabricated polydimethylsiloxane membrane using surface acoustic waves. *Applied Physics Letters*, 105(3):033509, 2014.

[216] JP Mills, M Diez-Silva, DJ Quinn, M Dao, MJ Lang, KSW Tan, CT Lim, G Milon, PH David, O Mercereau-Puijalon, et al. Effect of plasmodial resa protein on deformability of human red blood cells harboring plasmodium falciparum. *Proceedings of the National Academy of Sciences*, 104(22):9213–9217, 2007.

[217] Hope A Cranston, Charles W Boylan, Gregory L Carroll, Salvatore P Sutera, IY Gluzman, DJ Krogstad, et al. Plasmodium falciparum maturation abolishes physiologic red cell deformability. *Science*, 223(4634):400–403, 1984.

[218] Subra Suresh, J Spatz, JP Mills, Alexandre Micoulet, M Dao, CT Lim, M Beil, and T Seufferlein. Connections between single-cell biomechanics and human disease states: gastrointestinal cancer and malaria. *Acta biomaterialia*, 1(1):15–30, 2005.

[219] CD Wood, JE Cunningham, R ORorke, C Wälti, EH Linfield, AG Davies, and SD Evans. Formation and manipulation of two-dimensional arrays of micron-scale particles in microfluidic systems by surface acoustic waves. *Applied Physics Letters*, 94(5):054101, 2009.